MODELLING OF PHOTOVOLTAIC CHARACTERISTICS OF LEAD - FREE $Cs_{1-x}Rb_xSnI_3$ –SILICON TANDEM SOLAR CELL

AKOTO EMMANUEL

A Thesis Submitted to the Institute of Postgraduate Studies of Kabarak University in Partial Fulfillment of the Requirements for the Award of the Master of Science in Physics

KABARAK UNIVERSITY

NOVEMBER, 2023

DECLARATION

1. I do declare that:
    - i. This thesis is my original work and to the best of my knowledge it has not been presented to any institution as a research paper for the award or conferment of any academic degree or diploma.
    - ii. That the work has not incorporated material from other works or a paraphrase of such material without due and appropriate acknowledgement.
    - iii. That the work has been subjected to the process of anti-plagiarism and has met Kabarak University 15% similarity index threshold.
2. I do understand that issues of academic integrity are paramount and therefore I may be suspended or expelled from the university or my degree be recalled for academic honesty and other related malpractices.

Signature: .... Date: ....

Akoto Emmanuel

GMP/M/1895/09/20

RECOMMENDATION

To the Institute of Postgraduate Studies:

The thesis entitled **“Modelling of photovoltaic characteristics of lead-free $Cs_{1-x}Rb_xSnI_3$ – silicon tandem solar cell”** and written by **Akoto Emmanuel** is presented to the Institute of Postgraduate Studies of Kabarak University. We have reviewed the research thesis and recommend it be accepted in partial fulfillment of the requirement for award of the Master of Science in Physics.

Signature:.. Date: ....

Prof. Christopher Maghanga
Department of Biological and Physical Sciences,
Kabarak University.

Signed:... Date: ....

Dr. Benjamin Victor Odari Ombwayo
Department of Physics
Masinde Muliro University

COPYRIGHT

DEDICATION

This work is dedicated to my parents Evans Mutange Akoto and Judith Nafula Mutange my siblings, and friends for their endless love, support, and encouragement.

ACKNOWLEDGMENTS

I greatly and sincerely thank my research supervisors: Prof. Christopher Mkirema Maghanga and Dr. Victor Odari for their positive and timely guidance and their invaluable support since we started this research work to its conclusion. I also appreciate both the teaching and non-teaching staff of Kabarak University School of Science, Engineering, and Technology for their involvement in my research. Further, I acknowledge the administration and management of Kabarak University for providing a conducive environment for the development of this research. Special thanks go to my family for all the sacrifices they made to ensure that am able to start and complete my studies. I also express my heartfelt gratitude to Sandy Sanford, Milton and Barbie Ordom who supported me financially. It hasn’t been easy but through this compounded effect, it was possible. Above all, my great appreciation goes to God for His grace.

ABSTRACT

The full potential of perovskite – silicon tandem solar cells is yet to be realised despite its power conversion efficiency being higher than all other solar cell technologies. To optimize and leverage on this new technology, several techniques and materials are explored. Silicon and perovskite materials are used in several photovoltaics and optoelectronics applications. This research study primarily focuses on the simulation of perovskite – silicon tandem solar cells and investigated the photovoltaic characteristics by using the open-source solar cell capacitance simulator (SCAPS-1D) software. The top cell is the perovskite cell and the bottom is the silicon cell. The top cell was simulated independently with the structure ITO/$Cs_{0.8}Rb_{0.2}SnI_3$/PCBM/BCP/Al with an efficiency of 2.25 %. The effect of varying thickness, defect density, and doping concentration of the absorber layer, variation of Electron Transport Layer (ETL) thickness and doping concentration, and influences of the work function of Cl – doped and undoped – Indium-doped tin oxide (ITO) front contact of the tin-based perovskite solar cells were studied. Optimum open circuit voltage$(1.0356\ V)$, short circuit current density$(23.76\ mA/cm^2)$, fill factor $(83.18\ \%)$and efficiency $(20.46\ \%)$ are determined. The bottom cell was simulated independently using the structure Au/c-Si (n)/c-Si (p)/c-Si (p+)/Al with an efficiency of 26.68 %. The monolithic $Cs_{0.8}Rb_{0.2}SnI_3$ perovskite– silicon tandem solar cell of the architecture ITO/$Cs_{1-x}Rb_xSnI_3$/c-Si (n)/c-Si (p)/c-Si (p+)/Al performance was analyzed by varying the thickness, doping concentration, and defect density of the active layers. Optimized parameters for the tandem cell were as follows: top perovskite layer thickness $(100\ nm)$, doping concentrations $(5\ \times\ 10^{19} cm^{-3})$and defect density $(1\ \times\ 10^{13} cm^{-3})$, and bottom silicon absorber layer thickness $(50\ \mu m)$, doping concentrations $(5\ \times\ 10^{16} cm^{-3})$, defect density $(1\ \times\ 10^{12} cm^{-3})$, with Cl doped – ITO of work function $5.3\ eV$ as front contact. Optimized outcomes of efficiency$(29.82\ \%)$, open-circuit voltage$(0.7992\ V)$, short circuit current density$(43.39\ mA/cm^2)$, and fill factor $(85.58\ \%)$ were realized for the lead-free $Cs_{1-x}Rb_xSnI_3$ – silicon 2T tandem solar cell.

Keywords: *Tandem solar cells, Silicon,* $Cs_{1-x}Rb_xSnI_3$*perovskite, SCAPS-1D*

TABLE OF CONTENTS

LIST OF TABLES

LIST OF FIGURES

LIST OF ABBREVIATIONS AND ACRONYMS

2T	Two terminal
4T	Four Terminals
a– Si	Amorphous silicon
Al	Aluminum
AMPS	Analysis of Microelectronic and Photonic Structures
ASA	Amorphous Semiconductor Analysis
BCP	Bathocuproine
B-γ- $CsSnI_3$	Black Gamma Phase Cesium Tin Tri- Iodide
CBO	Conduction Band Offset
CdS	Cadmium Sulphide
CdTe	Cadmium Teleride
$CH_3NH_3PbX_3$	Methylammonium lead halide-based perovskite
CIS or CIGS	Copper Indium (Gallium) Diselenide
Cl – doped ITO	Chlorine doped Indium tin oxide
Cs	Cesium
$Cs_{1-X}Rb_XSnI_3$	Mixed cation of Cesium and Rubidium Tin Tri - Iodide
CsI	Cesium Iodide
C-Si	Crystalline silicon
$CsSnI_3$	Cesium Tin Tri - Iodide
$CuInS_2$	Copper Indium Sulphide
CuSCN	Copper Thiocyanate
HTL	Hole Transport Layer
ITO	Indium- doped tin oxide
J-V	Current density-voltage
MACl	Methylammonium Chloride
MAH_2PO_2	Methylammonium Hypophosphite
Pb	Lead
PCBM	Phenyl C61 Butyric Acid Methyl Ester
PCE	Power Conversion Efficiency
PERC	Passivated emitter rear contact
P-I-N	Inverted planar architecture

PSCs	Perovskite Solar Cells
PV	Photovoltaic
Rb	Rubidium
RbI	Rubidium Iodide
SCAPS-1D	Solar capacitance Simulator One Dimension
SDG(s)	Sustainable Development Goal(s)
Si	Silicon
Sn	Tin
Sn – HaP	Tin based halide perovskites
SnI_2	Tin dioxide
S-Q	Shockley- Quisser
SRH	Shockley- Read- Hall recombination model

LIST OF SYMBOLS AND FORMULAE

τ	Relaxation time
ε	Dielectric permittivity
ε_o	Permittivity of free space
σ	Carriers' capture cross section
χ	Electron affinity
η	Power conversion efficiency (PCE)
ρ	Density of charge (C/cm^3)
$\boldsymbol{\varphi}$	Electrostatic potential
μ , μ_n, μ_p	Mobility, Electron mobility and Hole mobility, respectively
Cl- doped ITO	Chlorine doped Indium Tin Oxide
d	Thickness
D	Diffusion
$D_{p,n}$	Diffusion coefficient of holes and electrons
E	Electric field
$E_C\, E_V E_F$	Conduction band, Valence band and Fermi level, respectively
E_g	Band gap energy
E_T	Defect energy level
eV	Electron volt
FF	Fill Factor
G	Carrier generation
J	Current density
J_{drift}	Drift Current
J_{diff}	Diffusion Current
J_{dark}	Dark current density
J_{light}	Illuminated current density
J_O	Dark saturation current density
J_{max}	Peak Current density
$J_{p,n}$	Current densities for holes and electrons
J_{ph}	Photo generated current density
J_{sc}	Short-circuit current density

K	Degree Kelvin
k_B	Boltzmann's constant
k_s	Semiconductor dielectric constant
m_e^*	Effective electron mass
n	Concentration of electrons
$n_t(x)$	Trapped electrons
$n(x)$	Free electrons
N_A^+	Acceptor ionized doping concentration
N_D^-	Donor ionized doping concentration
N_a	Concentration of acceptor
N_C	Density of states in the conduction band
N_D	Doping concentration
N_T	Defect density
N_V	Density of states in the valence band
p	Concentration of holes,
P_{max}	Peak power
$p_t(x)$	Trapped holes,
$p(x)$	Free holes,
q	Electron charge
R	Carrier recombination
R_{SRH}	Shockley- Read- Hall recombination
T	Temperature
U	Net recombination in a device
V	Voltage
V_{bi}	Built-in voltage
V_d	Drift Velocity
V_{max}	Peak Voltage
V_{oc}	Open-circuit voltage
v_{th}	Thermal velocity

CHAPTER ONE

INTRODUCTION

1.1 Introduction

This chapter gives a brief overview of the growing energy consumption and the shortcomings of fossil fuels hence the need for alternative energy sources such as solar energy. The advancement of solar cells through the first, second and third generations: the shift that has led to the study of lead – free $Cs_{1-x}Rb_xSnI_3$perovskite, crystalline silicon single cell and lead – free $Cs_{1-x}Rb_xSnI_3$Perovskite – Silicon 2T tandem solar cell (s) is explored. The problem statement, justification, objectives, research questions, scope and limitations of the study are dealt with in this chapter.

1.2 Background of the Study

Civilization comes with a steady increase in energy consumption. The increase in consumption of energy, more so electrical energy is expected to rise in the future to sustain human development. The increasing energy demand has caused a drastic decline in the fuel stocks, fossil fuel being a primary source of energy (Z. Liu, 2015) hence creating an energy crisis. This compounded with increasing carbon dioxide emissions that are causing global warming has enhanced interest in the development of clean renewable sources of energy (Xu *et al*., 2021). Extensive research on solar energy accompanied by technological advances over the last twenty years augments solar usage by further decreasing costs and increasing solar panel efficiency (Sahare *et al*., 2021). Solar cells hence hold great hopes for use as an environmentally friendly and economically viable renewable source of energy, hence an alternative to fossil fuels (Trieb & Elnokraschy, 2007). There are three basic generations of solar cells, though one of them doesn't quite exist yet, and research is ongoing.

They are designated as first (or Silicon) solar cells, second (or thin films) solar cells, and third generation solar cells, differing according to their cost and efficiency (Khatibi *et al.*, 2019). The first solar cell based on a silicon (Si) p-n junction with 6% power conversion efficiency (PCE) was invented at the Bell Labs in 1954 (Chapin *et al.*, 1954). Since then, Si-based solar cells have undergone decades of development including device structure design, Si defects passivation, optical design, and wafer surface treatment, (L. Hao *et al.*, 2021) which boosts the device efficiency gradually to a world-record value of 23.3% for multi- crystalline Si cell (Richter *et al.*, 2017), 26.1% for single crystal Si cell (Partain *et al.*, 1987), and 26.7% for Si-based heterostructure solar cell (Stevenson & Luchkin, 2021).

Further improvement in device PCE for Si-based single-junction solar cells becomes a bottleneck in this field since the device efficiency is approaching the Shockley-Quisser (S-Q) limit of 29% for a single-junction cell (Jiang *et al.*, 2021). Traditional solar cells are made from silicon, which are currently the most efficient, long-lasting, and account for around 80+ percent of all the solar panels sold (Sampaio & González, 2017). Silicon however has an indirect bandgap and is not able to absorb much sunlight as compared to direct bandgap materials. Thicker Silicon layers are required to absorb the same amount of light as any thin layer of direct bandgap material (Makori *et al.*, 2015).

Second-generation (thin-films) solar cells are made from layers of thin semiconductors. They offset many of the disadvantages of the conventional silicon cells by use of less material of lower cost, less energy, and lower-cost manufacturing processes making largescale production of thin films feasible (Devi *et al.*, 2018). Photovoltaic conversion of solar energy from low-cost solar cells will be a very important solution to supply the increasing energy demands when the conventional source of energy is depleted in the future (P. Liu *et al.*, 2011). Thin-film solar cells are made by depositing a thin layer of semiconductor on a supporting material (substrates) such as glass, stainless steel by chemical vapor deposition. The materials selected for deposition are strong light absorbers, most commonly amorphous silicon (a-Si), cadmium telluride (CdTe) and copper indium (gallium) diselenide (CIS or CIGS) (Seshan, 2012). These materials are suitable for deposition over large substrate areas (up to 1 meter) and hence allow high volume manufacturing (Bhatia, 2014). In terms of costs, amorphous silicon thin film solar cells use less than 1 percent of the silicon used in conventional cells, and the material costs are also lower for cells using CdTe or CIS technologies (Rahman, 2021). These cells also do not require assembling and are flexible, hence having versatile applications. The efficiency levels of these thin film solar cells range between 6 to 8 per cent (Bhatia, 2014).

Third generation of solar cells have drawn a great deal of attention over the years since the introduction of methylammonium lead halide-based perovskite ($CH_3NH_3PbX_3$ = Cl, Br, I) (Kojima *et al.*, 2009).Its remarkable features such as ideal tunable bandgap, long diffusion length, excellent carrier transport mechanism, and ease of fabrication have made the perovskite material become a formidable competitor to the traditional silicon-based solar cells (Shi & Jayatissa, 2018). The search for Perovskite solar cells (PSCs) with high efficiencies and stability is an active area of research. Lead halide perovskites have displayed the highest solar power conversion efficiencies of 25.7 % (Green *et al.*, 2019). Pb toxicity of the lead halide perovskite is however a serious hurdle in the quest for commercial development of the solar cell (Green *et al.*, 2014). Lead-free perovskites have emerged as viable candidates for potential use as light harvesters to ensure clean and green photovoltaic technology (Kour *et al.*, 2019) .Tin (Sn) is one of the most promising alternative candidates to replace Pb, being its closest analogue with similar structural and electronic properties. Most efficient Pb-free perovskite solar cells (PSCs) to date always include Sn in the perovskite composition (Ke *et al.*, 2019).

Motivated by the tandem configuration, a few years ago, research scientists started to fabricate perovskite – Si tandem solar cells. The first reported proof-of-concept was a perovskite – Silicon four-terminal (4T) tandem solar cell that exhibited an overall power conversion efficiency (PCE) of 13.4 % (6.2 % of the top cell and 7.2 % of the bottom cell) in 2014. The authors estimated that 31.6 % power conversion efficiency (PCE) can be achieved with both optical and electrical optimization (Löper *et al.*, 2015). The first perovskite – Silicon two-terminal (2T) tandem solar cell was reported with an overall power conversion efficiency of 14.3 % in 2015. Simulation results indicate a possible 32 % power conversion efficiency (PCE) with optimization of the transparent top electrode and interconnection layers between the top and bottom cell (Mailoa *et al.*, 2015).

The certified PCE of perovskite – Silicon tandem solar cells increased dramatically from 23.5 % in 2017 to 29.5 % in 2020, exceeding the S-Q limit of Si single-junction cell, but it is still far from saturating (Cheng & Ding, 2021). According to the reported optical and electrical analysis, the efficiency limit of perovskite – Silicon tandem cell is over 40 % (Futscher., 2016), indicating that there is still a room for boosting the device efficiency of tandem solar cells.

The single-junction solar cell efficiency is limited by its intrinsic optical bandgap(Benduhn *et al.*, 2017). The tandem devices however, by combining semiconducting materials with different bandgaps are able to react with a wider range of solar spectrum, generating power greater than the S-Q limit (Leijtens *et al.*, 2018). In a tandem configuration, the top solar cell with relatively wide bandgap absorbs photons with high energy (such as ultraviolet and visible light), while the bottom solar cell with relatively narrow bandgap harvests photons with low energy such as near infrared part of the solar spectrum (Lin *et al*., 2021). In this way, more photons can be absorbed and converted into electricity. Generally, the tandem solar cell architecture could either be a monolithically integrated device where the wide bandgap top cell is directly fabricated on top of the narrow bandgap bottom cell to form a series connection between the two sub cells (2T tandem cell), or a mechanical stack where the two sub cells are only coupled optically but electrically separated (4T tandem cell). In the perovskite – Si tandem solar cells circuit, the sub cells in a 2T tandem device are connected in series, current matching of the top and bottom cell is always required to ensure the overall device current is not limited by the sub-cell with lower current. The 4T tandem solar cells are not subject to current matching since the top and bottom cells are electrically separated (Lin *et al*., 2021).

1.3 Statement of the Problem

Solar cells are considered among promising alternatives to fossil fuels (Makori *et al*., 2015). Crystalline silicon solar cells (c-Si) are not only stable, non-toxic and abundant but also the dominant technology on the commercial photovoltaic market, comprising above 80 % of total demand (Jäger *et al*., 2019). However the PCE of silicon (Si) solar cell has been stuck around 25 % for 15 years, therefore some approaches are needed to enhance the Si solar cell performance. In the family of solar cells.Perovskite Solar Cells (PSCs) have emerged as one of the most promising photovoltaic (PV) technology (Kojima *et al.,* 2009). Lead-based perovskite solar cells exhibit outstanding performance. However, the toxicity of Pb increases environmental damage and is also a barrier to the mass production and commercialization of perovskite solar cells (Wang *et al*., 2019). Introduction of Pb-free perovskites enhances the affordability of perovskite solar cells, apart from being safe. The lead –free perovskites however are faced with a major challenge of low efficiency and stability. Novel design strategies for perovskite materials with improved stability and high performance have to be explored. One such way to mitigate the deficiencies of both cells, a perovskite – silicon tandem solar cell is designed and optimized (Nogay *et al.*, 2019), the top cell being $Cs_{1-x}Rb_xSnI_3$perovskite which is a viable alternative to lead-based perovskites. The perovskite – silicon tandem solar cell is reliable material due to its potential to raise the efficiency past the theoretical limit.

1.4 Research Objectives

1.4.1 General Objectives of the Study

To model and investigate the photovoltaic characteristics of lead – free $Cs_{1-x}Rb_xSnI_3$ – silicon tandem solar cell

1.4.2 Specific Objectives of the Study

i. To investigate the effect of thickness, defect density and doping concentration on the lead – free $Cs_{1-x}Rb_xSnI_3$ absorber layer.

ii. To evaluate the effect of variation of electron transport material (ETL) thickness, doping concentration and CBO and influence of the ITO and Cl – doped ITO front contact work function on the lead – free $Cs_{1-x}Rb_xSnI_3$perovskite solar cell.

iii. To determine the photovoltaic characteristics of lead – free $Cs_{1-x}Rb_xSnI_3$ – silicon tandem solar cell.

iv. To assess the effect of thickness, defect density and doping concentration on the absorber layers in the lead – free $Cs_{1-x}Rb_xSnI_3$ – silicon tandem solar cell.

1.5 Research Questions

i. What is the effect of thickness, defect density and doping concentration on the performance of the lead – free $Cs_{1-x}Rb_xSnI_3$perovskite absorber layer?

ii. What is the effect of variation of the thickness and doping concentration of the electron transport material as well as the influence of the back contact work function on the lead – free $Cs_{1-x}Rb_xSnI_3$perovskite solar cell?

iii. What are the photovoltaic characteristics of lead – free $Cs_{1-x}Rb_xSnI_3$ – silicon tandem solar cell?

iv. What is the effect of thickness, defect density and doping concentration on the absorber layers in the lead – free $Cs_{1-x}Rb_xSnI_3$ – silicon tandem solar cell?

1.6 Justification of the Study

There is a growing demand for materials with desirable properties required in the fabrication process of a solar cells. Crystalline silicon solar cells have dominated the photovoltaic market since the very beginning in the 1950s (Baloch *et al.*, 2018). Silicon is nontoxic and abundantly available in the earth's crust, and silicon PV modules have shown their long-term stability over decades in practice. Perovskites have physical, optical, and electrical characteristics that aim to increase the efficiency and lower the cost of solar energy. Perovskite PVs indeed hold promise for high efficiencies, as well as low potential material & reduced processing costs (Lin *et al.*, 2021). Despite the fast development of perovskite PV technology, the practical application of PSCs is significantly limited by their small device area and poor device stability.

The advantage of tandem solar cells is that they exploit sunlight better. By using a higher bandgap material as top cell which is higher than 1.124 eV of the silicon bandgap(Baloch *et al.*, 2018), the higher energy photons generates a voltage approximately twice that which silicon can generate. In perovskite – silicon tandem device, the high energy photons are absorbed by the top cell of perovskite, while the low energy photons are absorbed by the Silicon bottom cell. The lead – free $Cs_{1-x}Rb_XSnI_3$ ($x \leq 0.2$) perovskite with a bandgap of ~1.4 eV is a compatible contender as a material for the top cell in tandem configuration (Marshall *et al*., 2018). Numerical simulations are required to study the behavior of systems/materials whose mathematical models are too complex to provide analytical solutions. This gives deeper insight into the material/system for optimization without much wastage incurred in actual calibration of the materials by different iterations and for a far lesser cost than the actual calibration of a material (Devi *et al*., 2018).

1.7 Significance of the Study

Experimental and theoretical concepts and trends of the tandem solar cells predicts a photovoltaic device with high conversion efficiency. In pursuit of an environmental friendly device with the predicted properties, research has been done on different structures of solar cells. This work endeavors to study a lead – free $Cs_{1-x}Rb_xSnI_3$ – silicon tandem solar cell hence providing a lead to experimental physicists in the moderation of variation of different parameters of study for achieving its maximum potential. This achievement contributes to the industrialization of the energy sector to come to the realization of Sustainable Development Goal (SDG 7) which aims to increase substantially the share of renewable energy in the global energy mix.

1.8 Scope of the Study

This study focused on the numerical modelling and characterization of lead – free $Cs_{1-x}Rb_xSnI_3$ – silicon tandem solar cell for photovoltaic applications.

1.9 Limitation of the Study

The SCAPS application was used without any modification or alteration to the original source code; through validation from experimentation literature. The limited extent to which SCAPS could predict the properties of the material, are hence the confines to which this research was undertaken.

CHAPTER TWO

LITERATURE REVIEW

2.1 Introduction

This chapter is a presentation of both empirical and theoretical review on $Cs_{1-x}Rb_xSnI_3$ perovskite, crystalline silicon solar cells and lead – free $Cs_{1-x}Rb_xSnI_3$ – silicon tandem solar cell. The studies that have been done on and the deduced general theory on the interaction of light in photovoltaics in relation to the aforementioned solar cells are discussed. The working principle behind photovoltaic cell and the SCAPS simulator is also covered extensively using mentioned equations.

2.2 Empirical Review

2.2.1 $Cs_{1-x}Rb_xSnI_3$ Perovskite Solar Cells

B-γ- phase $CsSnI_3$ is a wholly inorganic perovskite comprising a 3-dimensional structure of corner sharing SnI_6octahedra with Cs cations surrounded by 8 SnI_6octahedra, and adopts the orthorhombic B-γ- phase below 89°C. It possesses a high electron and hole mobility, a small exciton binding energy (Chen *et al.*, 2012; L. Huang & Lambrecht, 2016) and offers strong inter-band absorption and photoluminescence. Tin vacancies however can readily form, leading to heavily p-type semiconductors which can be regarded as metallic in the degenerately doped limit (10^{19} cm^{-3}). Thin-film samples with 10 % excess SnI_2 produce materials with a low equilibrium hole-density hence minimize the presence of excess tin halide during film deposition, offering semiconducting behavior. To date it has been used as the light harvesting semiconductor in planar (Marshall *et al.*, 2015, 2016, 2018) device architectures, demonstrating the potential to achieve very high short circuit current density (Song *et al.*, 2017) and high device fill factor (FF)(Marshall *et al.*, 2016) under one sun illumination .

The primary factor limiting the power conversion efficiency of B-γ- $CsSnI_3$ based PVs is the low open-circuit voltage, V_{oc}. To date the highest V_{oc} reported is ~ 0.55 V (Marshall *et al*., 2016) achieved for an inverted device architecture using phenyl-C61-butyric acid methyl ester (PCBM) as the electron transport layer (ETL). One strategy is to curb this is to tune the electronic structure of B-γ- $CsSnI_3$ by substitution of A-site Cs cation with the smaller Rbcation to form $Cs_{1-x}Rb_xSnI_3$. The orbitals of the A-site metal cation indirectly affect the band gap as a result of the distortion of the lattice of SnI_6octahedra via tilting that occurs when reducing the size of the A-site ion (Jung *et al*., 2017; Prasanna *et al*., 2017). B- γ- $CsSnI_3$ PV devices with an inverted planar device architecture exhibit the best efficiency and stability without a hole-transport layer. This simplified device architecture was hence used as a test bed for this perovskite material. By increasing the molar composition of Rb (value of x), V_{oc}can be significantly increased in this type of perovskite material. However it was observed that as the number of Rb atoms substituting Cs increased the stability of the perovskite decreased.

Over the years a steady progress has been made in elevating the efficiency and enhancing air stability of this single cation (Cs) based Sn perovskites. However, the challenge of commercialization has pushed the scientific and research community to come up with unique ideas. A new trend of combining two or more cations in a single perovskite has emerged, as it offers numerous possibilities of enhancing device performance and stability. This idea proved very successful in lead based perovskites(Namvar *et al*., 2019; Salado *et al*., 2017; Sun *et al*., 2017; X. Zhang *et al*., 2017) , simultaneously gaining the attention of groups working on Sn based perovskites keeping in view the objectivity of high efficiency and long term stability. Uniform morphology with better crystal quality, significant suppression of defect profile and suppression of oxidation of tin are achieved with the Rb incorporated film. The incorporative additive ensures enhancement in the device performance and stability (Khadka *et al*., 2020). The $Rb_xCs_{1-x}SnI_3$ alloy follows Vegard's law well in terms of lattice constants, distortion angles, and band gap. The ionization potentials and electron affinities vary strongly with surface termination, which can be tuned with synthesis conditions (Jung *et al*., 2017).

Marshall and group (Marshall *et al*., 2018) first reported this 3D mixed cation $Cs_{1-x}Rb_xSnI_3$ perovskite, for PV application. The 3D perovskite $Cs_{1-x}Rb_xSnI_3$ can be prepared from room temperature N, N-dimethylformamide solutions of RbI, CsI and $SnCl_2$ for $x \leq 0.5$, and that for $x \leq 0.2$ film stability is sufficient for utility as the light harvesting layer in p-i-n architectures. When $Cs_{0.8}Rb_{0.2}SnI_3$perovskite is incorporated into the model inverted PV device structure; ITO|$Cs_{0.8}Rb_{0.2}SnI_3$|PCBM|BCP|Al, a $V_{oc}$of 0.5 V is achieved (Marshall *et al*., 2018). However, for this low Rb loading the increase in band gap is very small ~0.6 eV and so an increase in V_{oc} is achieved without reducing the range of wavelengths over which the perovskite can harvest light. This champion cell for $x \leq 0.2$ provided a PCE of ~ 2.25% and was the preferred option for photovoltaic applications.

2.2.2 Tandem Solar Cells

Monolithic tandem techniques (perovskite – CIGS, perovskite – silicon, perovskite – perovskite tandems) were first reported in 2015 and experienced a remarkable development over time. The PCE has recently improved to 23.5 % (Ruiz-Preciado *et al*., 2022), 28.7 % (Sveinbjörnsson *et al*., 2022) and ~20 % (Zheng *et al*., 2022) and for all-perovskite, perovskite – silicon and perovskite – CIGS tandems, respectively. Many 2T tandem solar cells have been designed by using silicon as a lower cell with a steady improvement in PCEs over time. Despite the similar high-efficiency potential of all three tandem technologies, progress in the development of the all-perovskitetandem and perovskite – CIGS cells has been slow although recently impressive results have been reported (Jošt *et al*., 2020).

Silicon base hetero-junction and nanocrystalline recombination junctions, demonstrated a PCE of 25.5 % (Sahli *et al*., 2018). A PCE of 25.0 % for perovskite – silicon tandem solar cells after minimizing the parasitic absorption and reflection losses with optical optimization in the perovskite precursor, by adding MACl and MAH_2PO_2 (Bush *et al*., 2018). The efficiency of perovskite – silicon-heterojunction tandem solar cells was improved from 23.4 % to 25.5 % by utilizing a textured foil for light manipulation (Jošt *et al*., 2018). A valid stable figure of 25.2 % for power conversion efficiency could be obtained by making use of silicon oxide nanocrystalline-based optical interlayer in perovskite – silicon tandem solar cell (Mazzarella *et al*., 2019). Using high temperature resistant p-type crystalline silicon lower cells in 2T perovskite – silicon tandem solar cells, they exhibit a stable state and attained 25.1 % PCE (Nogay *et al*., 2019). Highly effective monolithic tandem solar cells could be realized by combining rear silicon hetero-junction lower cells with p-i-n perovskite top cells that give a certified PCE of 25 % and 26 % after reducing current mismatch but with slightly less fill factor (Köhnen *et al*., 2019). Oxford PV demonstrated the highest PCE of 28 % (Green *et al*., 2019).

Solar cells involving crystalline silicon (c-Si) are the dominant technology on the commercial photovoltaic (PV) market, comprising 66 % of total demand in 2020 (P. Liu *et al*., 2011). Literature findings postulate silicon attracting a great deal of attention by far, from the various potential lower cell technologies for perovskite based tandem cells. The dominant mono-crystalline solar cell technology used in silicon single-junction solar cells is based on passivated emitter rear contact (PERC) technology, generating PCEs well beyond 20 % and exceeding 700 mV. The perovskite – silicon two-terminal (2T) tandem has also been designed on a homo- junction silicon solar cell treated with classical processes of high-temperature diffusion (Mailoa *et al.*, 2015). Hetero-junction cell with an efficiency of 26.6 % and a V_{oc} of 740 mV hold today's single-junction silicon cell record (Yoshikawa *et al.*, 2017). The cell was manufactured with interdigitated back contacts, however, not fitted to 2T requirements. The device with either side contacted holds the record for a Tunnel Oxide Passivated Contact (TOPCon) technology of 25.7 % (Richter *et al.*, 2017). In this research, a monolithic lead – free $Cs_{1-x}Rb_xSnI_3$ – silicon tandem solar cell was studied, and its performance optimized by varying some prime parameters.

2.3 Theoretical Review

To study the complex performance of semiconductors, numerical simulation is used to solve the Poisson and continuity semiconductor equations. Several parameters such as absorber thickness, defect density, donor concentration can be used to understand individual carrier densities, carrier transport mechanism, electric field distribution, and recombination profiles which are optimized to achieve a better solar cell.

2.3.1 Photovoltaic Effect

In a solar cell, an electron-hole pair is created when light is absorbed. Both chemical and electrical processes are involved in creating current and voltage in a semiconductor when exposed to light (Khallaf *et al.*, 2009). The light that is incident to a p-n junction solar cell is transmitted through the n-type material to the p-type semiconductor which absorbs it leading to generation of electron-hole pair. Some of the charge carries with generated minority are swept by electric field to across the junction in the depletion region. The electrons are collected at n-type region while holes are collected at p-type region. Photocurrent is kept connected through the collection of the charges across the cell. A semiconductor does not absorb all the light that is incident to its surface, part of the light is transmitted through the material and also a portion of the light is reflected by the surface of the semiconductor (Kurumi *et al*., 2008).

The absorption coefficient is a parameter that measures the ability of the material to absorb light (Khallaf *et al*., 2009). Electrons in the valence band absorb photons that have energy that is greater than the band gap which makes them to be excited to states that are higher. An electron-hole pair is created when the electrons that have been excited cross the band gap and move to the n-side. The electron-hole pair is separated by an internal electric junction field, hence electrons move towards the n-side while holes to the p-side of the cell (Kurumi *et al*., 2008).

2.3.2 Working principle of Photovoltaic Solar Cells

The commonly known photovoltaic solar cells are derived from a p – n junction formed by bringing two asymmetrically doped semiconductors together. The semiconductor with donor impurities is referred to as n – type semiconductor while the other with acceptor impurities is called the p – type semiconductor. The p – n junction formed can either be of the same material or different materials forming a homojunction or hetero junction respectively. When light of sufficient energy is irradiated on the solar cell, a potential difference is generated at the junction of the two different semiconductors. A solar cell is two terminal device which conducts like a rectifier diode in the dark and generates a photo voltage when illuminated (Nelson, 2003).

2.3.3 Solar Cell Device Characterization Parameters

The simplest characterization in a solar cell is the determination of the current – voltage relationship which involves parameters such as the short- circuit current density, J_{sc}, the open-circuitvoltage, V_{oc}, theFill Factor, FF and the peak power, P_{max}.These parameters are determined from the illuminated $J - V$characteristic curve as illustrated in Figure1.

The conversion efficiency, η, is determined from these parameters as shown in Equation 2.15. The following sub-section gives a brief explanation and formulae for these parameters based on an ideal solar cell.

Figure 1

J – V characteristic of a solar cell in the dark and under illumination

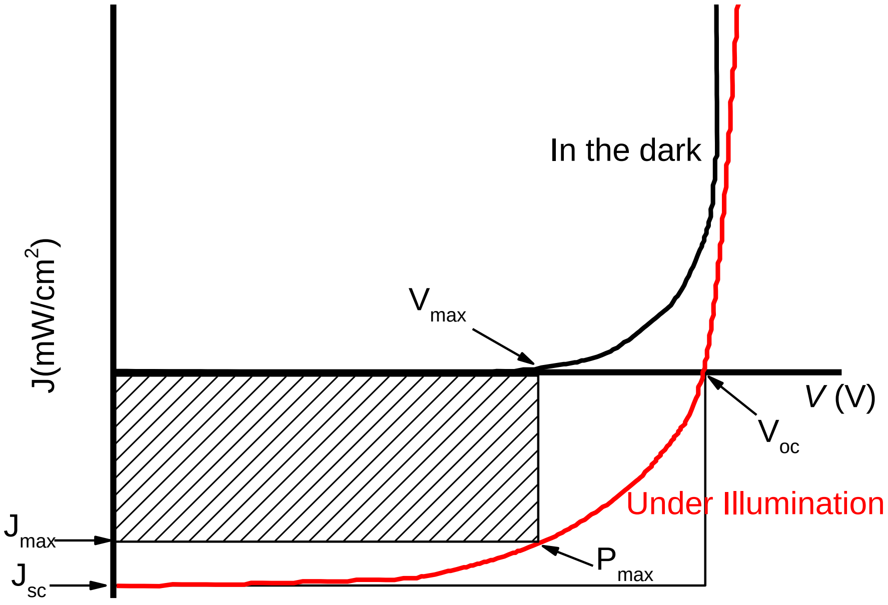

(a) Short-Circuit Current Density, J_{sc}

The short- circuit current density is the maximum photo-generated current per unit area delivered by a solar cell when the terminals of the solar cell are in contact with each other. It ideally represents the contribution of the photocurrent to the electronic transport. This is the current flowing through an external circuit attached to the metal contacts of the solar cell under short-circuit conditions (Araoz, 2009). It is determined from the net current density $J_{light}(V)$ in an illuminated solar cell which is given as (Nelson, 2003)

$$J_{light}(V) = J_{dark}(V) - J_{ph} \tag{2.10}$$

Where J_{ph} is the photon generated current density and

$J_{dark}(V)$ is the dark current density given by:

$$J_{dark}\,(V) = J_o\left(e^{qV/nk_BT} - 1\right) \qquad (2.11)$$

Where T is the absolute temperature, J_o is the dark saturation current density and n is the ideality factor with values between 1 and 2 and V is the voltage across the junction (Nelson, 2003).

Thus, with the electronic charge $(q = 1.603 \times 10^{-19} C)$ and Boltzmann's constant $(k_B = 1.38 \times 10^{-23} JK^{-1})$ the illuminated solar cell equation is given by

$$J_{light}\,(V) = J_o\left(e^{qV/nK_BT} - 1\right) - J_{ph} \qquad (2.12)$$

(b) The open-circuit voltage, V_{oc}

The open circuit voltage V_{oc} defined by J (V_{oc}) = 0, is the maximum voltage obtainable from the solar cell and a measurement of the change in electrochemical potential of electrons and holes with respect to their equilibrium conditions in the darkness. V_{oc} depends on the photo-generated current density, J_{ph}. For an ideal solar cell, it is given by (Nelson, 2003):

$$V_{oc} = \frac{nK_BT}{q}\ln\left(\frac{J_{ph}}{J_o} + 1\right) \qquad (2.13)$$

(c) Fill factor, FF

The fill factor is the ratio of the maximum power $P_{max} = J_{max} \times V_{max}$ generated by a solar cell and the product of V_{oc} and J_{sc}. It describes the 'squareness' of the $J - V$ curve. Equally, it is the area ratio of the rectangle of maximal area covered by the axis and the experimental I (V) curve to that enclosed by the axis and the corresponding parallels at V_{oc} and J_{sc}.

$$FF = \frac{V_{max}J_{max}}{V_{oc}J_{sc}} == \frac{P_{max}}{V_{oc}J_{sc}} \qquad (2.14)$$

(d) Power Conversion Efficiency, η

This is the ratio of the generated maximum power and the incident power on the solar cell. It is given by:

$$\eta = \frac{P_{max}}{P_{in}} = \frac{V_{oc} \times J_{sc} \times FF}{P_{in}} \qquad (2.15)$$

2.3.4 Solar cell simulation in SCAPS

Computational simulation is a technique of studying and analyzing properties of thin films, real devices or an imaginary system using mathematical models by mimicking it with a computer software.

A number of solar cell simulation applications have been developed over the years such as AMPS (Analysis of Microelectronic and Photonic Structures), ASA (Amorphous Semiconductor Analysis), PC1D, SimWindows, ADEPT-F, SILVACO TCAD, SYNOPSYS ATLAS and many others as viable tools for studying and understanding the properties of solar cell devices such as the optical and electrical properties of complex solar cell devices. Simulation also helps to reduce processing cost and time spent on solar cell device fabrication by providing useful information on optimum values of parameters that contribute to the improvement of the device's performance. It further predicts properties that may not be easy to determine experimentally.

In this section, the operation of Solar Cells Capacitance Simulator (SCAPS) developed by University of Gent is described, which was used to carry out the simulations is described in detail.

(a) Description of working principles of SCAPS

SCAPS 1D simulator is used to simulate the electrical characteristics of thin-film heterojunction solar cells by solving the basic semiconductor device equations under steady state conditions (Burgelman *et al.*, 2016). A brief description of running a simulation is as follows:

Figure 2

SCAPS start up panel: The Action Panel

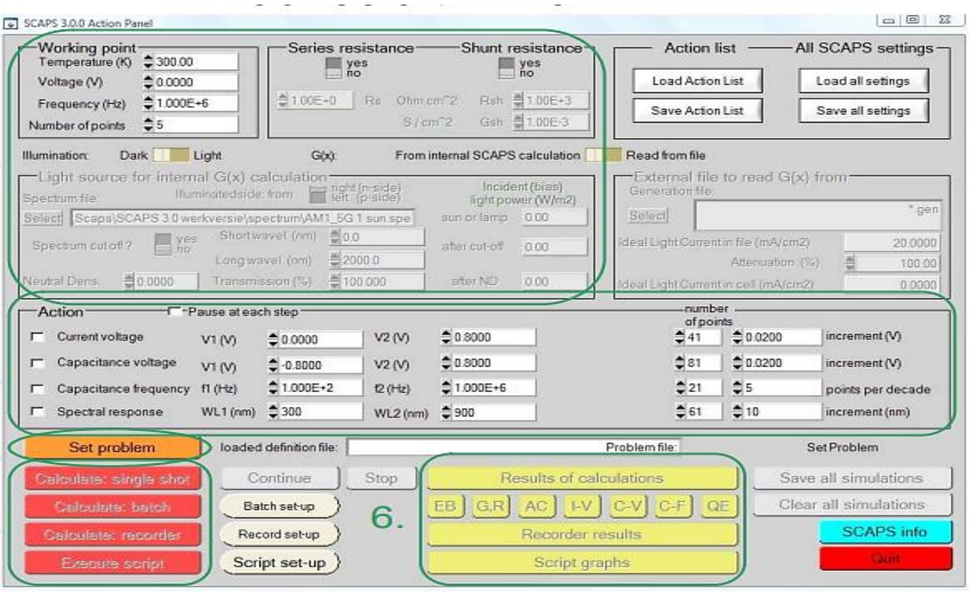

SCAPS 3.0.0 Action Panel

Working point
Temperature (K) 300.00
Voltage (V) 0.0000
Frequency (Hz) 1.000E+6
Number of points 5

Series resistance: Rs 1.00E+0 Ohm.cm^2
Shunt resistance: Rsh 1.00E+3 Ohm.cm^2; Gsh 1.00E-3 S / cm^2

Illumination: Dark / Light
G(x): From internal SCAPS calculation / Read from file

Light source for internal G(x) calculation
Spectrum file: Scaps\SCAPS 3.0 werkversie\spectrum\AM1_5G 1 sun.spe
Illuminated side: from right (n-side) / left (p-side)
Incident (bias) light power (W/m2): sun or lamp 0.00; after cut-off 0.00; after ND 0.00
Spectrum cut off? yes / no
Short wavel. (nm) 0.0
Long wavel. (nm) 2000.0
Neutral Dens. 0.0000
Transmission (%) 100.000

External file to read G(x) from
Generation file: *.gen
Ideal Light Current in file (mA/cm2) 20.0000
Attenuation (%) 100.00
Ideal Light Current in cell (mA/cm2) 0.0000

Action ☐ Pause at each step

					number of points		
☐ Current voltage	V1 (V)	0.0000	V2 (V)	0.8000	41	0.0200	increment (V)
☐ Capacitance voltage	V1 (V)	-0.8000	V2 (V)	0.8000	81	0.0200	increment (V)
☐ Capacitance frequency	f1 (Hz)	1.000E+2	f2 (Hz)	1.000E+6	21	5	points per decade
☐ Spectral response	WL1 (nm)	300	WL2 (nm)	900	61	10	increment (nm)

loaded definition file: Problem file:
Set Problem

(b) Derivation of the governing equations in SCAPS

SCAPS simulation is governed by three semiconductor equations: Poisson's equation, electron and hole continuity equations and the carrier transport equations. SCAPS numerically solves these equations for the electrostatic potential, electron and hole concentration as function of positions *x*.

a. Poisson equation

The Poisson equation connects the electric potential Φ and the charge as shown in equation 2.16 (Jehad & Hamammu, 2013; Physics, 2014).

$$\frac{d}{dx}\left(-\varepsilon(x)\frac{d\Phi}{dx}\right) = q[p(x) - n(x) + N_D^+(x) - N_A^-(x) + p_t(x) - n_t(x)] \qquad (2.16)$$

where p is the free hole density, n is the free electron density, $N_D^+(x)$ is the ionized-donor density, $N_A^-(x)$ is the ionized-acceptor density, $p_t(x)$ and $n_t(x)$ are trapped hole density and trapped electron density respectively, and ε is the dielectric constant of the medium.

In the simulation, SCAPS determines the electrical potential Φ and the carrier concentrations p and n (Φ, n, p) by solving the coupled differential equations (Burgelman *et al.*, 2016).

b. Continuity equations

The continuity equations in a semiconductor describe the change in carrier density over time due to the difference between the incoming and outgoing flux of carriers (electrons and holes) and their generation and recombination rates (Zeghbroeck, 2011). The derivation of the continuity equation is shown below.

Figure 3

Likely generation and recombination processes and electron currents

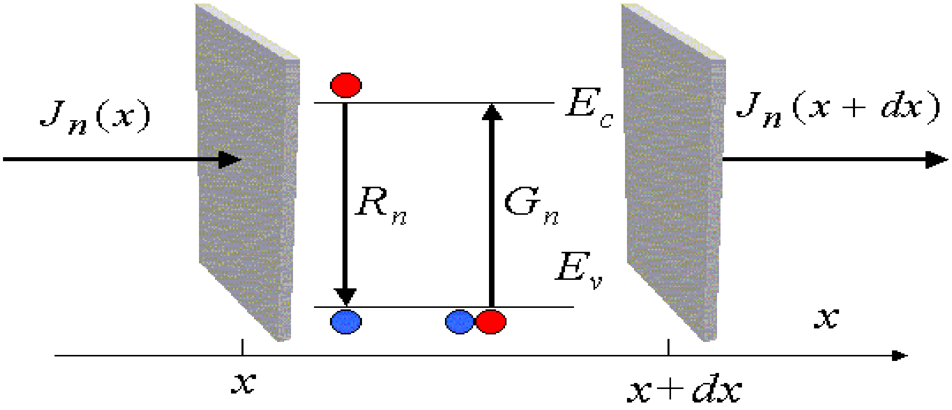

Note: Adapted from Zeghbroeck, (2011)

Figure 3 shows an elemental volume in which a one- dimensional electron flux $J_n(x)$ and $J_n(x+dx)$ entering and leaving the elemental volume at x and $(x+dx)$ respectively. R_n and G_n are respectively rates of electron recombination and generation in the semiconductor device. The rate of change of electrons between x and $(x+dx)$ is equal to the difference between the incoming and outgoing flux and the difference between the generation and recombination.

If $-qn(x,t)$ is the electron carrier density in the volume, then, the total carrier charge in the volume

$$= -qn(x,t)dV = -qn(x,t)dxdydz = -qn(x,t)A_x dx \tag{2.17}$$

Total number of charges generated $-qG_n dV = -qG_n A_x dx$

Total number of charges recombined $-qR_n dV = -qR_n A_x dx$

Therefore, the change of charges in the volume

$$-q\frac{\partial_n(x,t)}{\partial t}A_x dx = [J_n(x) - J_n(x+dx)]A_x - q(G_n - R_n)A_x dx \tag{2.18}$$

\By Taylor expansion, $J_n(x+dx) \sim J_n(x) + \frac{\partial J_n}{\partial x}dx$

$$-q\frac{\partial_n(x,t)}{\partial t}A_x dx = \left[J_n(x) - J_n(x) - \frac{\partial J_n}{\partial x}dx\right]A_x - q(G_n - R_n)A_x dx$$

$$-q\frac{\partial_n(x,t)}{\partial t}A_x dx = -\frac{\partial J_n}{\partial x}A_x dx - q(G_n - R_n)A_x dx \tag{2.19}$$

Dividing through Equation (2.19) by $-qA_x dx$

$$\frac{\partial_n(x,t)}{\partial t} = \frac{1}{q}\frac{\partial J_n}{\partial x} + G_n(x,t) - R_n(x,t) \tag{2.20}$$

Similarly, for holes,

$$\frac{\partial_p(x,t)}{\partial t} = \frac{1}{q}\frac{\partial J_p}{\partial x} + G_p(x,t) - R_p(x,t) \tag{2.21}$$

Equations (2.20) and (2.21) are 1-D continuity equation for electrons and holes, respectively.

c. Carrier transport equations

The net flow of charge carriers in a semiconductor generates currents. The process by which these electrons and holes move is called transport**.** There are two main transport mechanisms in semiconductor devices which are Drift: - the movement of charge due to electric fields and Diffusion: - the flow of charge due to density gradients. The total current density expressions for these carriers due to both drift and diffusion mechanism is derived.

i. Drift current density

Drift current is the current generated by the movement of charge carriers due to an applied electric field, E as shown in Figure 4.

Figure 4

Carrier drift caused by an applied electric field

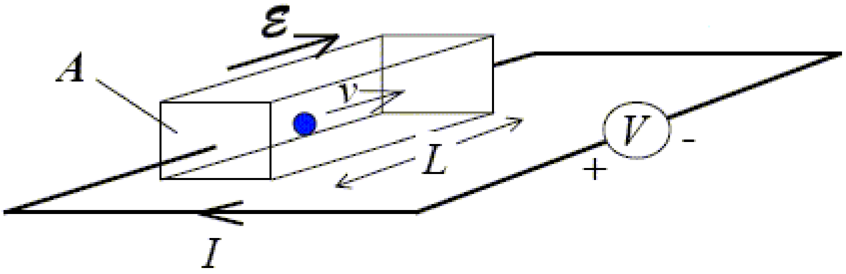

Note: Adapted from Zeghbroeck, (2011)

Where I = current and therefore $J = I/A$ = current density, σ = conductivity of the material, E= applied electric field.

When an Electric field ε is applied to a semiconductor device, it produces a force, **F** on the charge carriers which will experience a net acceleration**, a** (Neamen, 2003).

$$\boldsymbol{F} = m_e^* \boldsymbol{a} = -q\varepsilon \qquad (2.22)$$

$$-q\varepsilon = \frac{m_e^* \boldsymbol{v}_d}{t}$$

$$\boldsymbol{v}_d = -\frac{qt\varepsilon}{m_e^*} = -\mu_n \varepsilon$$

$$\boldsymbol{v}_d = -\mu_n \varepsilon \qquad (2.23)$$

Where, $\boldsymbol{v}_d$ is the drift velocity, q is the elementary charge, $\mu_n = \frac{qt}{m_e^*}$ is the electron mobility, t is time and m_e^* is the effective mass of electron.

The total current flux *J* passing through the box of volume V with length L as shown in Figure 4 is the total number N of charges passing through a unit area A per unit time. Mathematically (Amu, 2014);

$$J_{n|drift} = -\frac{NqL}{At} = -\frac{Nq\boldsymbol{v}_d}{A}$$

$$J_{n|drift} = -nq(-\mu_n\varepsilon)$$

n is electron number density given as $\frac{N}{V}$. If the electron passing through the entire volume of the box is considered; $\frac{N}{A} = \frac{N}{V}$.

$$J_{n|drift} = nq\mu_n\varepsilon \qquad (2.24)$$

Similarly, for holes the current density becomes

$$J_{p|drift} = pq\mu_p\varepsilon \qquad (2.25)$$

Therefore, the total drifts current becomes $J_{drift} = J_{n|drift} + J_{p|drift}$

$$J_{drift} = q\varepsilon(n\mu_n + p\mu_p)$$

ii. Diffusion current density

Diffusion is the process where particles flow from a region of higher concentration toward a region of lower concentration. A thermal equilibrium state of the system where the net flow of electrons and holes do not significantly alter the thermal equilibrium condition of the system (Neamen, 2003) is considered here. Figure 5 shows the electron concentration variation with position x in 1-D assuming uniform temperature so that the thermal velocity of the electron is independent of x.

Figure 5

Representation of diffusion process

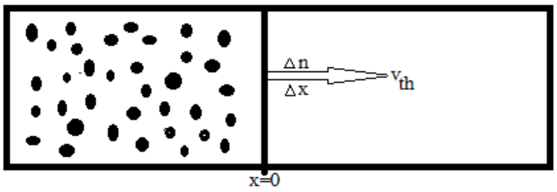

Note: Adapted from Neamen, (2000)

Figure 6

Profile of carrier density for deriving the diffusion current expression

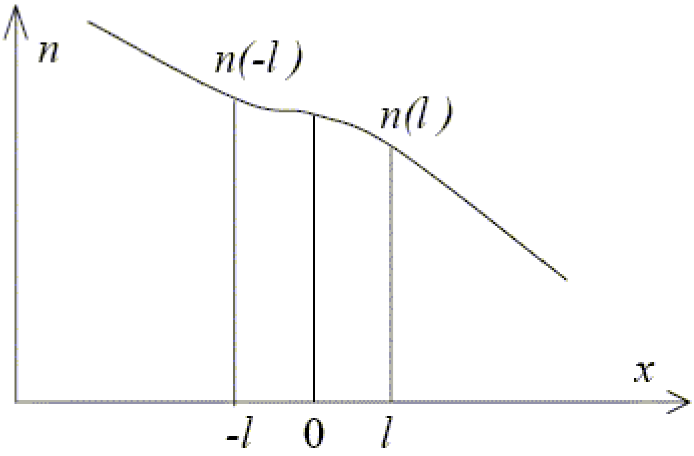

Note: Adapted from Zeghbroeck, (2011)

To calculate diffusion current for electron, defining some parameters is essential:

l = Mean free path of carrier

$n(x)$ = Carrier concentration

v_{th} = Thermal velocity

$Flux$ = Concentration × velocity

The flux of carrier crossing $x = 0$ from a distance $x = -l$ from left to right of Figure 6 is

$$F_{l-R} = \frac{1}{2} n(x = -l) v_{th} \tag{2.26}$$

The carrier flux crossing $x = 0$ from a distance $x = l$ right to left is

$$F_{R-l} = \frac{1}{2} n(x = l) v_{th} \qquad (2.27)$$

The factor $\frac{1}{2}$ is because a half path travel of the carrier flow is considered to the right while the other half to the left.

The net flux of carriers crossing $x = 0$ from left to right is

$$F_n = F_{l-R} - F_{R-l} = \frac{1}{2}[n(-l) - n(l)]v_{th} \qquad (2.28)$$

Using Taylor expansion for the carrier concentration about $x = 0$, to the first order gives;

$$n(-l) = n(0) - l\frac{dn}{dx} \qquad (2.29)$$

$$n(l) = n(0) + l\frac{dn}{dx} \qquad (2.30)$$

Substituting eqs. (2.29), (2.30) into (2.28)

$$F_n = \frac{1}{2}\left[n(0) - l\frac{dn}{dx} - n(0) - l\frac{dn}{dx}\right]v_{th} = -l\, v_{th}\frac{dn}{dx}$$

$$F_n = -\, D_n\frac{dn}{dx} \qquad (2.31)$$

$D_n = l\, v_{th}$

The electron diffusion current density $J_{n|diff} = -qF_n$

Therefore

$$J_{n|diff} = -qD_n\frac{dn}{dx} \qquad (2.32)$$

Similarly, for holes

$$J_{p|diff} = -qD_p\frac{dp}{dx} \qquad (2.33)$$

The diffusion current for both electrons and holes is thus given as;

$J_{diff} = J_{n|diff} + J_{p|diff}$

$$J_{diff} = q\left(D_n\frac{dn}{dx} - D_p\frac{dp}{dx}\right)$$

iii. Total current density, J

The total electron current density J_n for both drift and diffusion is:

$$J_n = J_{n|drift} + J_{n|diff}$$

$$J_n = q\left(n\mu_n\boldsymbol{E} + D_n\frac{dn}{dx}\right) \quad (2.34)$$

Similarly,

$$J_p = J_{p|drift} + J_{p|diff}$$

$$J_p = q\left(p\mu_p\boldsymbol{E} + D_p\frac{dp}{dx}\right) \quad (2.35)$$

where D_n and D_p are the diffusivities determined by Einstein relation as (Amu, 2014):

$$D_n = \frac{\mu_n K_B T}{q}$$

$$D_p = \frac{\mu_p K_B T}{q}$$

Equations (2.34) and (2.35) are the carrier current transport equation for electrons and holes, respectively, of a 1D semiconductor device.

Under steady state, $\frac{\partial n}{\partial t} = 0$ so that the continuity equations (Eq. 2.21) becomes

$$\frac{1}{q}\frac{\partial J_n}{\partial x} + G_n(x) - R_n(x) = 0$$

Substituting J_n from eq. 2.34 into the equation above;

$$n\mu_n\frac{dE}{dx} + \mu_n E\frac{dn}{dx} + D_n\frac{d^2n}{dx^2} + G_n(x) - R_n(x) = 0$$

Similarly, for holes

$$-p\mu_n\frac{dE}{dx} + \mu_p E\frac{dp}{dx} + D_p\frac{d^2p}{dx^2} + G_p(x) - R_p(x) = 0$$

2.3.5 Generation (Gn, Gp) and Recombination (Rn, Rp) processes in the absorber layer

When a semiconductor is irradiated with solar energy, photons are absorbed resulting in creation of electron-hole pairs by excitation of an electron from the valence band into the conduction band, thus forming a hole in the valence band. This excitation can either be classified as a direct transition or an indirect transition. In direct transition, the maximum of the valence band and the minimum of the conduction band coincide at the same position in the reciprocal space. In the indirect semiconductor, the valence band maximum and conduction band minimum are at different positions in the reciprocal space. This difference has to be compensated for momentum conservation to take place. For small differences, the change of the momentum can be provided by the momentum of the photon, while phonons have to be emitted or absorbed to balance larger variations.

After an electron-hole pair is generated, recombination mechanisms such as radiative and non-radiative start taking place. Radiative recombination is spectrally distributed and gives information on the electronic states of the recombining charge carriers. Several other recombination processes can be distinguished depending on which electronic states are involved in the transition as shown in Figure 7. Once excitation take place (1), the electrons and holes move to the band edges (thermalize) within a timescale of picoseconds (2) or into shallow states (3) next to the band edges by dissipating their energy by emission of phonons. Recombination of electron-hole pairs from the extended states of the conduction and valence bands gives rise to band-to-band luminescence (4). From the band edges the electron and hole recombine giving out a photon with the energy approximately equal to the band gap energy. Coulomb interaction of electron-hole pair and electron phonon coupling may possibly account for the slight deviations of the photon energy from the band gap energy.

Figure 7

Schematic diagram showing the generation and radiative recombination processes in semiconductor: (1) generation of an electron-hole pair, (2) thermalization to the band edges and (3) into shallow states close to the band edges. (4) band-band, (5) band-to-tail, (6) tail-to-band, and (7) tail-to-tail transitions are presented as well as transitions involving deep states in the band gap (8) and excitonic states (9)

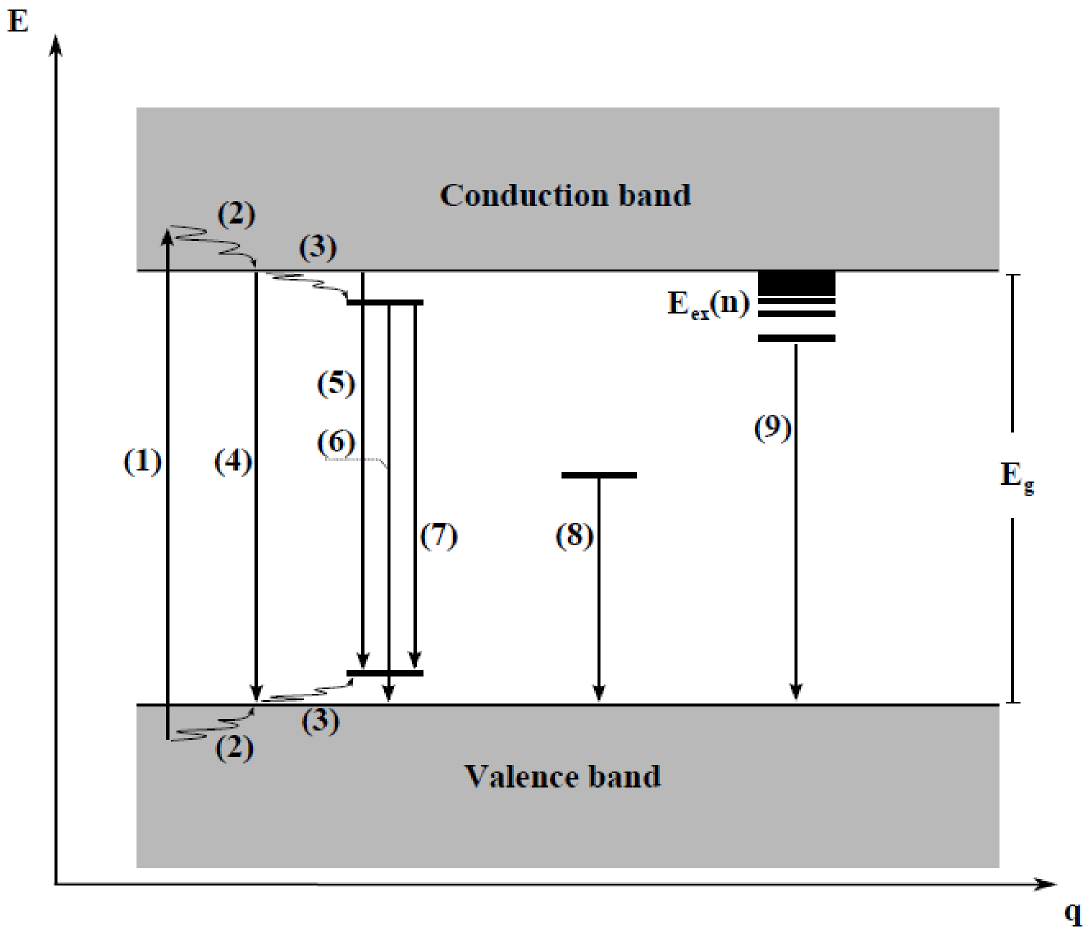

Note: Adapted from Nuys, (2015)

Furthermore, states within the band gap such as band-tail states and deep states may result in radiative transitions with energies lesser than the band gap energy. Transitions that involve band states and/or band-tail states are called band-to-tail (5), tail-to-band (6), or tail-to-tail (7) transitions. When deep states are included in the transition (8), the energy of the emitted photon is significantly lower than the band gap energy(Nuys, 2015). Lastly, luminescence can occur from excitonic states (9). An exciton is a bound electron-hole pair formed by the absorption of a photon. Owing to the coulomb interaction between the electron and the hole, the total energy of the exciton is marginally smaller than the band gap energy (Nuys, 2015).

2.3.6 Influence of Solar Cell Parameters

a) Absorber Defect Density

An understanding of the effect of defect densities on device performance is of much importance since generation and recombination processes occur inside the absorber layer. Morphology and quality of absorber films are key factors in determining the performance of solar cells(Xing *et al*., 2013). Charge recombination phenomena becomes dominant in the light absorber layer due to large defect density (N_T) that is brought about by poor film quality. The Gaussian distribution with neutral defects set to be at the center of the band-gap is a perfect approach to understand the influence of defect densities of the absorber layer because a lot of defect energy levels are existing in the layer (Yin *et al*., 2014). In light of the Shockley- Read- Hall recombination model (SRH), the effect of defect density on the cell performance of the silicon and perovskite layers (Sherkar *et al*., 2017) is investigated. In this recombination type, electrons in the conduction band and holes in the valence band recombine through trap states.

$$R_{SRH} = \frac{np - n_i^2}{\tau\ (p + n + 2n_i \cos h(\frac{[E_i - E_T]}{KT})} \qquad (2.36)$$

$$\tau = \sigma \times N_T \times v_{th} \qquad (2.37)$$

Where n and p are mobile electrons and holes concentrations, which are obtained by solving the Poisson equation and the Continuity equation for charge carriers. τ is the carrier lifetime and N_T and E_T are defect concentration and defect energy level, respectively. σ and v_{th} represent carriers' capture cross section and thermal velocity, respectively; they both give information about the generated carrier lifetimes as can be deduced. The perovskite material quality is quantified by the product of the carrier-capture cross-section σ and the trap density N_T (Baloch *et al*., 2018).

b) Absorber Layer Thickness

Absorber layer thickness plays an important role in determination of the performance of thin film solar cells. Optimum thickness ensures absorption of maximum number of photons to generate electron-hole pairs. When the absorber layer thickness is increased, the lower energy photons with longer illumination wavelengths that need a larger absorption depth produce an additional amount of electron-hole pair generation. If the layer is too thick, the photo- generated charge carriers must travel through the absorber to reach the electron and hole transport (carrier collection) layers, this necessitates low collection efficiency. Decreasing the absorber layer significantly means that the depletion region comes closer to the back contact, hence more electrons will be captured for recombination by the back contact. The decreased thickness is also not beneficial for full absorption of light, since there will be fewer electrons participating in the generation process and hence lowering the cell fill factor and power conversion efficiency (Nalianya *et al*., 2021). It is therefore essential to optimize the absorber layer thickness for maximum photon absorption and in turn maximum efficiency.

c) Absorber Doping Density

Absorber layer doping plays a key role in the performance of the device as it influences the electrical behavior of the layer. Appropriate doping levels can lead to an improved carrier transport by concentration of charges. Prior studies on Sn based perovskites show doping levels varied significantly in the range of $10^{15}cm^{-3} - 10^{21}cm^{-3}$ (F. Hao *et al*., 2014). Doping concentration variation influences cell performance due to the built-in electric field that increases with increase in N_A, this leads to high exciton dissociation and electron-hole migration with less recombination rate, hence the solar cell performance is improved (Mandadapu *et al*., 2017).

There was need for a comprehensive understanding of the complex relationship between the different parameters that affect the lead – free $Cs_{1-x}Rb_xSnI_3$ perovskite solar cell, the crystalline silicon solar cell and the lead – free $Cs_{1-x}Rb_xSnI_3$ perovskite – silicon tandem cell that guided the estimation of optimum values for best performance from tandem solar cells.

2.4 Conceptual Framework

The SCAPS 1D software has been used to study various materials and characterize them for photovoltaic applications. The main variables in this study were the absorber thickness, donor and acceptor concentrations and the defect density. The intervening factors are kept constant in this study since they could also affect performance of the material. The optimized parameters gave yield to the optimum power conversion efficiency, the open circuit voltage, the fill factor and the short circuit current density which contain valuable information to guide researchers about the materials

Figure 8

Conceptual Framework

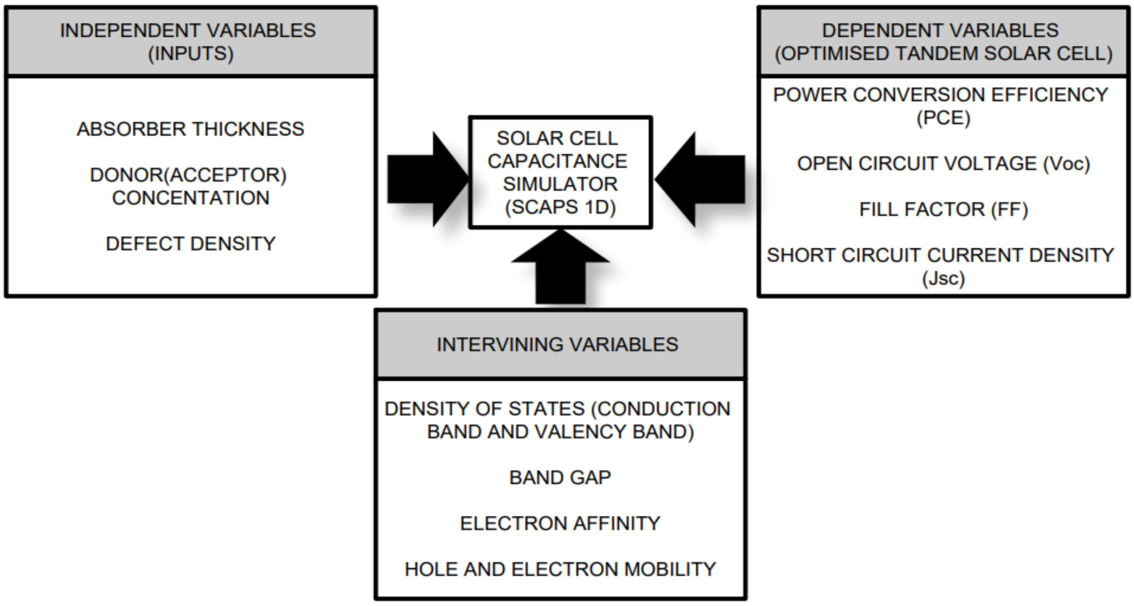

Source: Author (2023)

2.5 Research Gap

Table 1

Research Gap

Authors	Research	Key Findings	Research Gap
(Khadka *et al.*, 2020)	Passivation of the Recombination Activities with Rb incorporation for Efficient and Stable SnHaP Solar Cells	Rb incorporation controls surface chemistry, film formation and mitigation of trap centers hence uniform morphology with better crystal quality and suppression of oxidation of tin vacancies.	Incorporation of Rb into B-γ- $CsSnI_3$ and study its effect experimentally, theoretically and computationally
(Jung *et al.*, 2017)	Rb/Cs Cation-Exchange on Inorganic Sn Halide Perovskites	$Rb_xCs_{1-x}SnI_3$ demonstrates stability and follows Vegard's law in terms of lattice constants, distortion angles, and band gap	Subjection of the perovskite material $Rb_xCs_{1-x}SnI_3$for photovoltaic applications
(Monti *et al.*, 2018)	Efficient Intra-band Hot Carrier Relaxation in the Perovskite Semiconductor $Cs_{1-x}Rb_xSnI_3$:	Cation-tuning is explored as a route to improved performance where a small Rb fraction ($x \leq 0.1$) was used and found to increase the Voc of model inverted photovoltaic cells	Optimization of the potential of application of $Cs_{1-x}Rb_xSnI_3$
(Marshall *et al.*, 2018)	$Cs_{1-x}Rb_xSnI_3$ light harvesting semiconductors for perovskite photovoltaics	Experimental application of $Cs_{1-x}Rb_xSnI_3$ perovskite in an inverted planar device architecture without a HTL to achieve best stability and efficiency. The champion cell provided a PCE of 2.25%	Design and optimization of efficiency of $Cs_{1-x}Rb_xSnI_3$ using numerical methods in SCAPS.
(Aman *et al.*, 2021)	Numerical Modeling and Optimization of Perovskite – Silicon Tandem Solar Cell Using SCAPS-1D	Design and optimization of the efficiency of lead – based $CH_3NH_3PbI_3$ Perovskite – Silicon 2T tandem solar cell using SCAPS 1D with 32.97% efficiency.	Design and optimization of the efficiency of lead – free $Cs_{1-x}Rb_xSnI_3$ – Silicon 2T tandem solar cell using SCAPS 1D

The need and role of incorporation of Rb in different inorganic perovskites is gradually developed and studied through the literature outlined in the table 1. The practical incorporation and effect of replacement of Cs by Rb in the B-γ- $CsSnI_3$ structure to come up with $Cs_{1-x}Rb_xSnI_3$ mixed cation perovskite has caught the attention of researchers as an alternative to lead based perovskites. The new trend of research on lead – free $Cs_{1-x}Rb_xSnI_3$ perovskite – silicon tandem solar cells gives a further area to explore the photovoltaic nature of the material hence the reason for carrying out this research.

CHAPTER THREE

RESEARCH DESIGN AND METHODOLOGY

3.1 Introduction

In this chapter, the operation and working principles of the SCAPS 1D software is discussed. The simulation architectures and parameters of the perovskite, silicon and tandem solar cells are also detailed. The range of variation of the parameters in each structure is also discussed.

3.2 Methodology and Modelling

SCAPS-1D (ver.3.3.03) software was used for the device modelling. Various panels of the software are used to set or adjust the parameters from which results are inferred. In two-band gap system, higher bandgap absorber material forms the upper cell and lower bandgap absorber material forms the lower cell for optimum operation (Bremner *et al.*, 2016). Perovskite bandgap energies range from 1.4 eV to 1.9 eV (larger than silicon, band gap of ~1.1eV). This is relevant to the upper active layer for an efficient 2 – band gap structure (Almansouri *et al.*, 2015). SCAPS is fundamentally based on Poisson's differential equation for electrons and holes of semiconductors, coupled continuity differential equations and carrier transport equations as solved by Newton-Raphson and Gummel type iteration method (Burgelman *et al.*, 2000).

3.3 Simulation of Lead – Free $Cs_{1-x}Rb_xSnI_3$ Perovskite Solar Cell

The one dimensional SCAPS software, developed at the University of Gent, Belgium (Burgelman *et al.*, 2000) allows simulation of inverted planar devices. SCAPS is founded on three semiconductor equations which are Poisson’s equation, electron and hole continuity equations and the carrier transport equations and can model various homo-junctions, hetero-junctions, multi-junctions and Schottky barrier devices (Du *et al.*, 2016).The perovskite solar cell’s architecture is an inverted heterojunction of ITO/Cs_{1-}

$_x$Rb$_x$SnI$_3$/PCBM/ BCP/Al as shown in Figure 9 (a) with its energy band diagram in figure 10 (a), has a reported a *PCE* of 2.08 % experimentally (Marshall *et al*., 2018). The material parameters of the different layers have been selected from those reported in theoretical and experimental data of other works. Validation of results was accomplished by comparison of the simulated and experimental inverted (p-i-n) architecture of ITO/ Cs$_{1-x}$Rb$_x$SnI$_3$/PCBM/BCP/Al. A numerical variation of band gap with varying molar composition x in Cs$_x$Rb$_{1-x}$SnI$_3$ was done to study the behavior of the band gap in the perovskite material.

The conduction band offset (CBO) sign can be positive or negative depending on the photo-generated carrier barrier heights as indicated in the formulae CBO $=(\chi_{perovskite} - \chi_{ETL})$. The CBO was carefully optimized to reduce charge recombination at the absorber and ETL interface and that allows efficient carrier extraction. Electrical and optical characteristics of [6, 6]-Phenyl-C61-butyric acid methyl ester (PCBM) was used as ETL and its electron affinity varied to get the intended CBO.

Optimization of absorber thickness, defect density, and doping concentration, ETL (PCBM) thickness, doping concentration and CBO and ITO front contact was done by variation of parameters on specific ranges. Absorber thickness was varied on a range of (100nm–500 nm), defect density $(10^{14} - 10^{17} cm^{-3})$ and absorber doping concentration $(5 \times 10^{15} - 5 \times 10^{21} cm^{-3})$. ETL (PCBM) thickness was varied on a range of (40 nm-100 nm), doping concentration $(1 \times 10^{16} - 1 \times 10^{21} cm^{-3})$ and CBO $(-0.28\ eV) - (+0.22\ eV)$. Influences of the work function of the ITO on the Cs$_{1-x}$Rb$_x$SnI$_3$ perovskite solar cells was varied from $4.7\ eV - 5.6\ eV$. The work function of the Al metal back contact is determined at $4.2\ eV$. Tables 2, 4, 5 and 6 summarize parameters of each layer in the architecture and also indicate the parameters that were optimized for better results

Figure 9

Solar cells architecture, (a) p-i-n architecture of ITO/Cs1-XRbXSnI3/PCBM/BCP/Al, (b) Single junction Si cell of c-Si (p+)/c-Si (p)/c-Si (n) architecture and (c) Cs1-XRbXSnI3 – Si Tandem Solar cell Structure

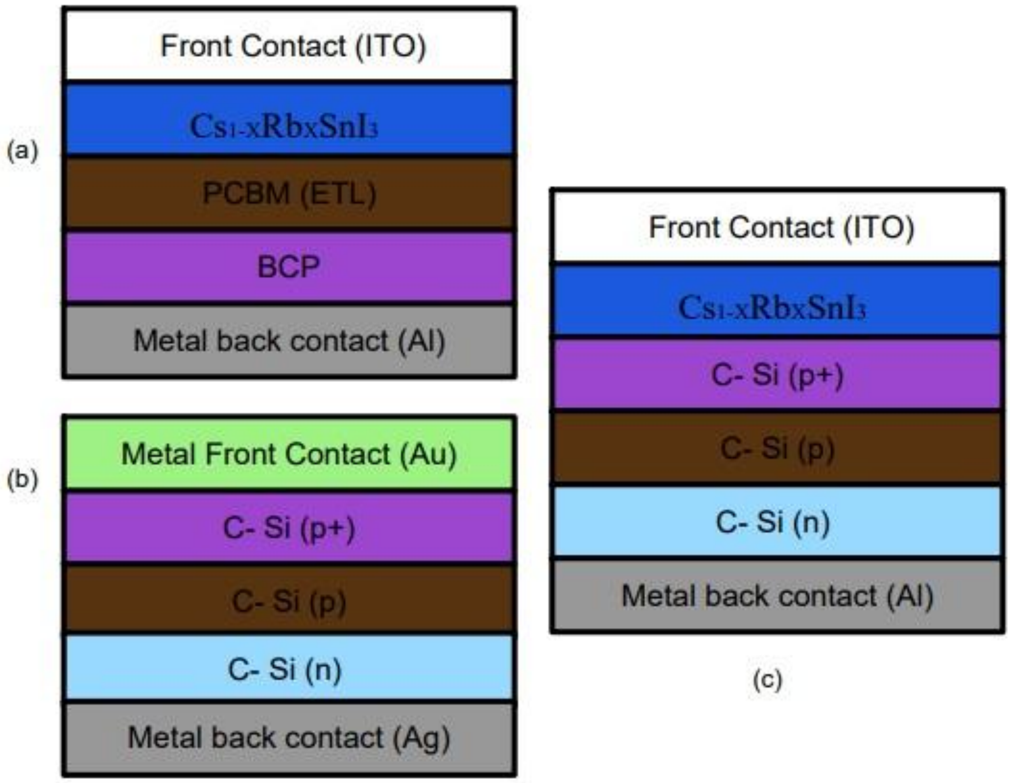

Figure 10

Energy band diagrams of (a) Lead – free $Cs_{1-X}Rb_XSnI_3$ *perovskite solar cell with -0.28 eV CBO, (b) Silicon cell with C-Si (p) at 1μm and (c) Lead – free* $Cs_{1-X}Rb_XSnI_3$ *perovskite solar cell with + 0.22 eV CBO (d) Lead – free* $Cs_{1-X}Rb_XSnI_3$ *perovskite – Silicon tandem solar cell with C-Si (p) at 1μm*

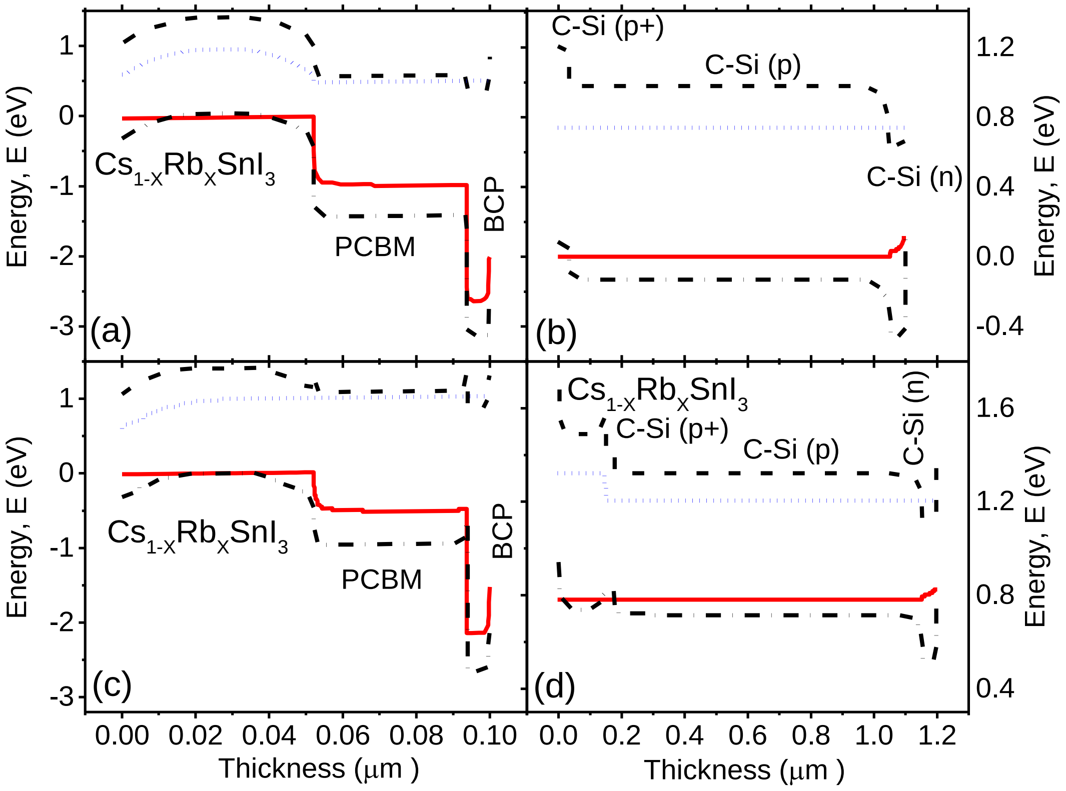

3.4 Simulation of Lead – Free $Cs_{1-X}Rb_XSnI_3$ – Silicon 2T Tandem Structure

To simulate a lead – free $Cs_{1-x}Rb_xSnI_3$ –Silicon 2T tandem solar cell, $Cs_{1-x}Rb_xSnI_3$ was used as a top (front) cell absorber, c-Si (p) for the bottom cell and the overall cell structure composes of ITO/Perovskite/c-Si (p+)/c-Si (p)/c-Si (n)/Al as shown in Figure 9 (c). The n-p-p+ structure covers a broad bandwidth spectrum of $1.12\ eV$ due to infrared photons transmission from perovskite cell. Combining both of these two cells, a tandem structure is formed. The single silicon cell is simulated following experimental data (Yoshikawa *et al.*, 2017) as shown in figure 9 (b). The $Cs_{1-X}Rb_XSnI_3$ perovskite cell was added into the single silicon cell where cells are configured in series producing a monolithic tandem structure. To get the optimum performance of the tandem solar cell, different physical parameters of top and bottom cells were taken into consideration. Tuning the thickness, donor/acceptor concentration and the defect density of the absorber layers, the PCE was optimized. Tables 3, 4, 5 and 6 summarizes parameters of each layer in the architecture of the 2T tandem solar cell and also indicates the parameters that were optimized for better results.

3.5 Device Simulation Parameters

All material parameters for simulation were obtained from reported experimental data and other works in literature. The individual materials parameters for c-Si, $Cs_{0.8}Rb_{0.2}SnI_3$ are shown in Table 2,3,4,5 and 6 below. Electron and hole- thermal velocity were set to $10^7 cm/s$ (Mandadapu *et al.*, 2017) The standard $AM1.5G$ spectrum and working temperature $300\ K$ were utilized in this model, however, shunt and series resistance values were not taken into consideration.

Table 2

Simulation Parameters for $Cs_{1-x}Rb_xSnI_3$ Perovskite Solar Cell

Parameter		Units	BCP	PCBM	$Cs_{0.8}Rb_{0.2}SnI_3$
E_g (Band gap)		eV	3.5 [a]	2.0 [a]	1.4 [b]
χ_e (Electron affinity)		eV	3.7 [a]	3.9 [a]	3.62 [c]
d (Thickness)		nm	6 [a]	40 [a]	50 [b]
ε_r (Permittivity)			10 [a]	4.0 [a]	25.7 [c]
μ_n (electron mobility)		cm^2 /Vs	$2x10^{-2}$ [a]	$1x10^{-1}$ [a]	$5.85x10^2$ [c]
μ_p (hole mobility)		cm^2 /Vs	$2x10^{-3}$ [a]	$1.5\ x10^{-2}$ [a]	$4.0x\ 10^1$ [c]
Effective density of states	Conduction band N_C	cm^{-3}	$1.8\ x\ 10^{21}$ [a]	$1.8\ x\ 10^{21}$ [a]	$1.58x10^{19}$ [c]
	Valence band N_V	cm^{-3}	$2.2\ x\ 10^{21}$ [a]	$2.2\ x\ 10^{21}$ [a]	$1.47x10^{18}$ [c]
Carrier density	Acceptor (N_A)	cm^{-3}	$1x10^{10}$ [a]	$1x10^{13}$ [a]	$5\ x\ 10^{18}$
	Donor (N_D)	cm^{-3}	$1x\ 10^{21}$	$1\ x10^{18}$	

Table 3

Simulation Parameters for Silicon solar cell and lead – free $Cs_{1-x}Rb_xSnI_3$ – Silicon 2T Tandem Solar Cell

Parameter		Units	$Cs_{0.8}Rb_{0.2}SnI_3$	c-Si (n)	c-Si (p)	c-Si (p+)
E_g (Band gap)		eV	1.4 [b]	1.124 [d]	1.124 [d]	1.124 [d]
χ_e (Electron affinity)		eV	3.62 [c]	3.9 [d]	4.05 [d]	3.9 [d]
d (Thickness)			150 [b]	50 nm [d]	100 µm [d]	30 nm [d]
ε_r (Permittivity)			25.7 [c]	11.9 [d]	11.9 [d]	11.9 [d]
μ_n (electron mobility)		cm^2 /Vs	5.85x10^{2} [c]	1250 [d]	1010 [d]	1212 [d]
μ_p (hole mobility)		cm^2 /Vs	4.0x 10^{1} [c]	443 [d]	443 [d]	421 [d]
Effective density of states	Conduction band N_C	cm^{-3}	1.58x10^{19} [c]	2.8x 10^{19} [d]	2.8 x 10^{19} [d]	2.84x 10^{19} [d]
	Valence band N_V	cm^{-3}	1.47x10^{18} [c]	1.04 x 10^{19} [d]	1.04 x 10^{19} [d]	1.04 x 10^{19} [d]
Carrier density	Acceptor (N_A)	cm^{-3}	5 x 10^{15}	0	5x 10^{16}	9.5 x 10^{18} [d]
	Donor (N_D)	cm^{-3}	0	8x 10^{21}	0	0

Table 4

Defects properties in $Cs_{0.8}Rb_{0.2}SnI_3$ and $Cs_{0.8}Rb_{0.2}SnI_3$ – C- Si Tandem solar cells

		Units	BCP	PCBM	$Cs_{0.8}Rb_{0.2}SnI_3$	c-Si (n)	c-Si (p)	c-Si (p+)
Type			Neutral	Neutral	Neutral	Neutral	Neutral	Neutral
Density of defects		cm^{-3}	1×10^{17}	1×10^{14}	10^{10} to10^{19}	1×10^{12}	1×10^{12}	1×10^{12}
Capture cross section	Electron (σ_n)	cm^2	1×10^{-15}	1×10^{-14}	1×10^{-15}	1×10^{-17}	1×10^{-17}	1×10^{-17}
	Holes (σ_p)	cm^2	1×10^{-17}	1×10^{-14}	1×10^{-15}	1×10^{-17}	1×10^{-17}	1×10^{-17}
Energy		eV	Above E_V	Above E_V	Above E_V	Above E_V	Above E_V	Above E_V

Table 5

Interface properties in $Cs_{0.8}Rb_{0.2}SnI_3$ and $Cs_{0.8}Rb_{0.2}SnI_3$ – C- Si Tandem solar cells

Interface		Units	PCBM/ $Cs_{0.8}Rb_{0.2}SnI_3$	$Cs_{0.8}Rb_{0.2}SnI_3$/C-Si (p)
Parameter			Neutral	Neutral
Density of defects		cm^{-2}	1×10^{12}	1×10^{12}
Capture cross-section	Electron (σ_n)	cm^{-2}	1×10^{-10}	1×10^{-10}
	Holes (σ_p)	cm^{-2}	1×10^{-10}	1×10^{-10}
Energy		eV	Below the lowest E_C	Below the lowest E_C

a. (Moiz & Alahmadi, 2021) b. (Marshall *et al*., 2018) c. (Jahangir *et al*., 2021) d. (Aman *et al*., 2021)

Table 6

Simulation Parameters for Contacts

Back Metal Contact Properties	
The electron work function of Al	4.2 eV
Surface recombination velocity of the electron	10^5 cm/s
Surface recombination velocity of hole	10^7 cm/s
Front Contact Properties	
The electron work function of ITO and Cl – doped ITO	4.7 eV – 5.6 eV
Surface recombination velocity of the electron	10^7 cm/s
Surface recombination velocity of hole	10^5 cm/s

3.6 Validation of Results

The SCAPS-1D software simulation validity was confirmed by comparison of simulated performance with experimental device performance of the $Cs_{0.8}Rb_{0.2}SnI_3$ perovskite and the single silicon cell following experimental data. The open circuit voltage, short circuit current density, fill factor and power conversion efficiency were of good match, as illustrated in the next chapter to determine the veracity of the simulated cells.

CHAPTER FOUR

DATA ANALYSIS, PRESENTATION AND DISCUSSION

4.1 Introduction

This chapter is divided into three main parts. First, the results of solar cell simulation of lead - free $Cs_{1-X}Rb_XSnI_3$ perovskite based solar cells with an inverted planar architecture are dealt with using SCAPS. The findings are compared with published experimental data for validation. Secondly, various photovoltaic parameters of both the absorber, the electron transport layer (ETL) and front contact work function of the p – i – n lead – free $Cs_{1-X}Rb_XSnI_3$ perovskite based solar cell are analyzed and optimum values reported. In the third section, additional layers are embedded on the silicon solar cell structure hence constituting the lead – free $Cs_{1-X}Rb_XSnI_3$ perovskite – Silicon tandem solar cell. The results of lead – free $Cs_{1-X}Rb_XSnI_3$ perovskite – Silicon tandem solar cells with lead – free $Cs_{1-X}Rb_XSnI_3$ and C – Si (p) as the absorber layers. The influence of different absorber layer (s) parameters on photovoltaic parameters of the solar cell were analyzed, optimum values reported and an optimum solar cell developed from the optimized parameters.

4.2 Validation of the modeled lead – free Cs1-XRbXSnI3 perovskite and Silicon Solar Cells

The SCAPS-1D software simulation validity is confirmed by comparison of simulated performance with experimental device performance of the $Cs_{0.8}Rb_{0.2}SnI_3$ perovskite as reported by Marshall (Marshall *et al.*, 2018) (Table 7). The single silicon cell is also simulated following experimental data (Yoshikawa *et al.*, 2017). There is a good matching between experimental and the calibrated results, which is proof of the validity and feasibility of device configuration and material parameters of the simulations as shown in Table 7 and 8.

Table 7

Using the Architecture of ITO/$Cs_{0.8}Rb_{0.2}SnI_3$/PCBM/BCP/Al

	Voc (V)	Jsc (mA/cm^2)	FF (%)	PCE (%)
Experimental (Marshall *et al.*, 2018)	0.50 ± 0.01	6.71 ± 0.71	0.61 ±0.03	2.05 ± 0.26
SCAPS 1D	0.4757	6.63	0.6597	2.08

Table 8

Using the architecture of Au/c-Si (p+)/c-Si (p)/c-Si (n)/Al

	Voc (V)	Jsc (mA/cm^2)	FF (%)	PCE (%)
Experimental (Yoshikawa *et al.*, 2017)	0.744	42.3	83.8	26.3 ± 0.5
SCAPS 1D	0.7443	43.29	83.30	26.68

Figure 11 (a) is a validity test to the viability of SCAPS 1D to the patterns of $Cs_{0.8}Rb_{0.2}SnI_3$ perovskite material that is being tested for photovoltaic application in order to optimize its parameters. The validity of the SCAPS device simulation is confirmed by comparison with devices performance from real experimental characterization reported by literature (Marshall *et al.*, 2018). In Figure 11 (b) electronic absorption and photoluminescence spectroscopy measurements supported by computational simulation, show that increasing Rb substitution (x) increases the band gap, E_g in $Cs_{1-X}Rb_XSnI_3$. This band gap is computationally predicted using DFT-1/2. The uncertainty in the DFT calculations is approximately ~0.1 eV. This increase is attributed to distortion of the lattice of SnI_6 octahedra that occurs when Cesium (Cs) is substituted with Rubidium (Rb), although it also reduces the stability towards decomposition

(Marshall *et al*., 2018). By varying the molar composition of Cesium (Cs) and Rubidium (Rb) the optimal value x was determined at 0.2 where stability is sufficient for utility as the light harvesting layer in inverted photovoltaic (PV) devices.

Figure 11

(a) Experimental (Marshall et al., 2018) and Simulation Graphs of $Cs_{0.8}Rb_{0.2}SnI_3$ *(b) Band gap evolution of* $Cs_{1-X}Rb_XSnI_3$ *with increasing Rb (X) substitution (Marshall et al., 2018)*

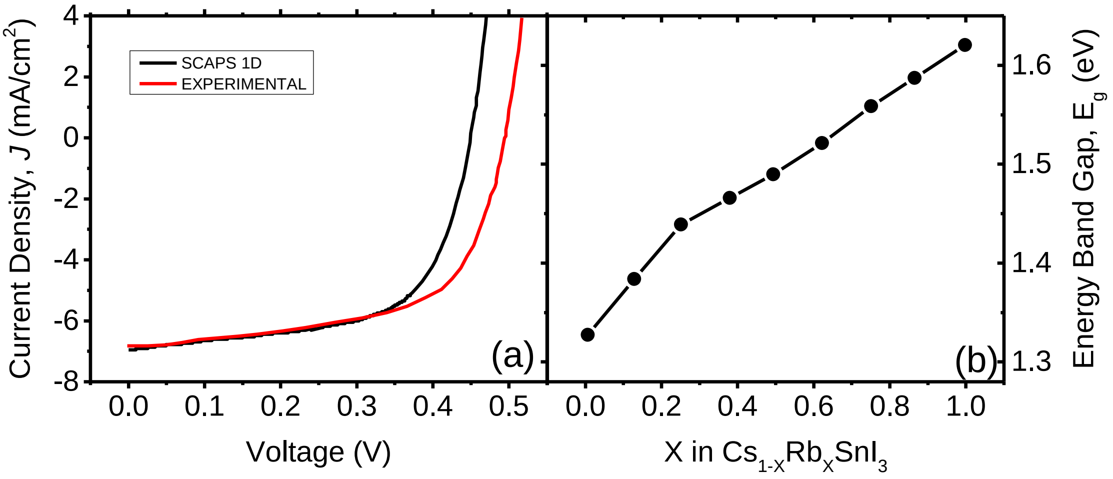

4.3 Numerical Simulation of Lead – Free Cs1-XRbxSnI3 and Silicon Solar Cells

Effect of thickness (nm) and defect density, NT (cm− 3) absorber layer on photovoltaic characteristics of lead – free Cs1-XRbXSnI3 perovskite solar cell.

Figure 12

Effect of thickness (nm) and defect density, N_T *(*cm^{-3}*) absorber layer on photovoltaic characteristics of* $Cs_{1-X}Rb_XSnI_3$ *perovskite solar cell*

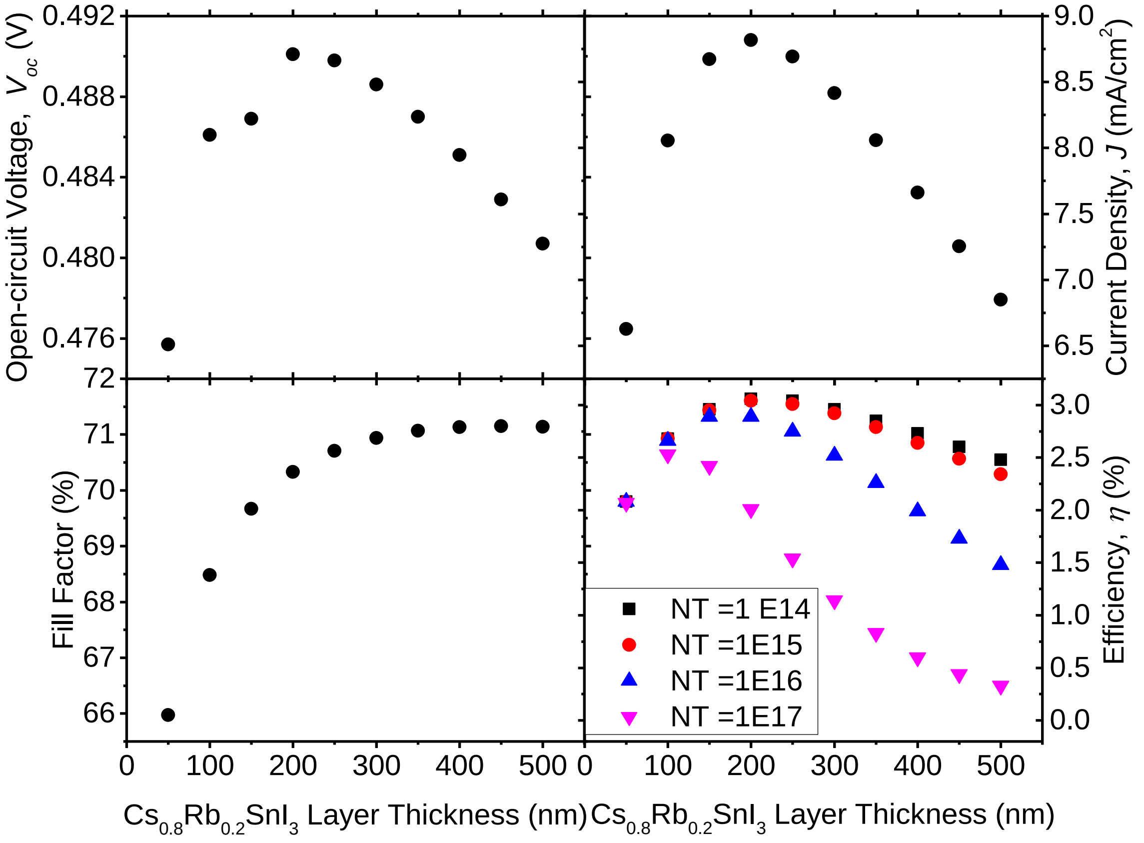

The thickness of the absorber layer plays an important role in charge extraction and hence the layer must be made sufficiently large to absorb all the penetrating incident radiation. Defects in an absorber material act as trap centers hence diminish the mobility and lifetime of the charge carriers and are therefore detrimental to cell performance. The *PCE* of various defect density $(1 \times 10^{14} - 1 \times 10^{17} cm^{-3})$ with increasing absorber thickness was simulated to obtain optimum defect density. Absorber thickness is thereafter varied from 100 nm to 500 nm at optimum defect density of the $Cs_{0.8}Rb_{0.2}SnI_3$ perovskite absorber layer to determine their effects on the solar cell performance as shown in Figure 12.

The optimum value of trap density is determined at 1×10^{15} cm^{-3} which gives a diffusion length of 640 nm. The thickness of $Cs_{0.8}Rb_{0.2}SnI_3$ perovskite layer is then varied from 50 nm to 500 nm at optimum defect density. Increase in $Cs_{0.8}Rb_{0.2}SnI_3$ perovskite layer thickness leads to an increase in solar cell *PCE* from 2.08 % at 50 nm, peaks at 200 nm (3.04 %) and thereafter deteriorates to 2.34 % at 500 nm. The J_{sc}, similar to the *PCE* increases from 6.63 mA/cm^2 at 50 nm, peaks at 8.82 mA/cm^2 at 200nm and thereafter significantly reduces to 6.85 mA/cm^2 at 500 nm. The V_{oc} also increases from 0.4757 V at 50 nm, peaks at 0.4901 V at 200 nm and thereafter reduces to 0.4807 at 500 nm with increasing absorber thickness. The increase in thickness of the absorber layer leads to an increase in the effective bandgap, which consequently results in the increase of the V_{oc} (Bag *et al*., 2020). For the overly thick photoactive layer beyond the optimum thickness, the V_{oc} suddenly drops due to aggravated recombination loss.

The *FF* increases from 65.97 % at 50 nm and increases to a maximum value of 71.14 % at 500 nm. The FF increases significantly implying that the FF is related to the efficiency of charge extraction that resulted from smaller built in voltage in the thicker devices (Momblona *et al*., 2014) meaning, increasing thickness increases the photon-capturing ability, which results in an increase in the rate of generation of charge carriers (Rai *et al*., 2020). The preferred optimized thickness for the $Cs_{0.8}Rb_{0.2}SnI_3$ perovskite based solar cell is selected at 200 nm, which is within the diffusion length range. Increase in defect density leads to a reduction in the photocurrent hence increasing the number of trap centers.

The carrier recombination rate therefore increases in turn decreasing the carrier lifetime and diffusion length and hence the overall performance of the device decreases (Li *et al*., 2020).The *PCE* increases for $N_T = 1 \times 10^{15} cm^{-3}$ due to increased absorption, hence increased exciton generation as the absorber thickness was increased peaking at 200 nm.

There is a significant increase in the fill factor, owing to reduced internal resistance in the solar cell. The increased thickness necessitates an increase in spectral response at the longer wavelength solar irradiance hence the increasing J_{sc}. There is however an increase in carrier recombination rate in comparison with the carrier generation rate, with the increasing absorber thickness which leads to the saturation of J_{sc} at 200 nm. The increase in thickness of the absorber layer leads to reduction of the effective bandgap, which consequently results in a reduction of the V_{oc} (Bag *et al.*, 2020).

Effect of absorber doping concentration on solar cell parameters of lead – free Cs1-XRbXSnI3 perovskite solar cell.

Figure 13

Effect of absorber doping concentration on solar cell parameters of $Cs_{1-X}Rb_XSnI_3$ *perovskite solar cell*

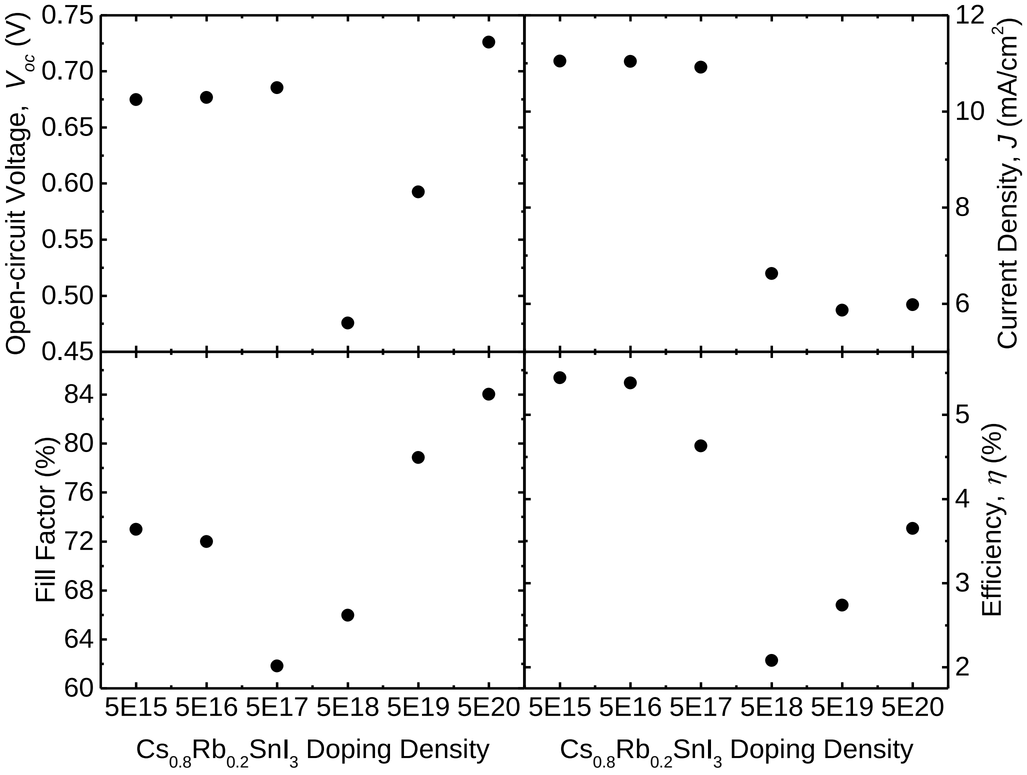

The charge carrier density is one of the key factors for designing a perovskite solar cell structure (Ushasree *et al.*, 2019). Carrier concentration of the absorber layer is important to obtain the most favorable PV action of the cell. Doping of the photoactive layer influences the electrical behavior of the absorber material which in turn affects the performance of the solar cell device (Coulibaly *et al*., 2019). The absolute carrier density in the absorber layer is beneficial to generate a suitable electric field and strengthen the separation of the photo generated charge carriers (Parisi *et al*., 2015). In this section, the influence of absorber doping density on solar cell parameters of $Cs_{0.8}Rb_{0.2}SnI_3$ perovskite solar cell is studied. For a better understanding of the influence of doping on photovoltaic parameters, doping levels varied from $10^{15} - 10^{20} cm^{-3}$ as shown in figure 13. Doping beyond 10^{21} cm^{-3} is regarded as heavy doping may render the semiconductor degenerate and therefore have metallic tendencies which is not desirable.

Doping below 10^{16} cm^{-3}, is considered light doping and may not be optimal due to the little electrical conductivity in the semiconductors, hence to optimally operate this range was preferred. Variations in photovoltaic characteristics with changes in doping concentrations are shown. It's worth noting that *PCE*, similar to the *FF* decrease with the increasing N_A values to minimum values of 2.08 % at $10^{18} cm^{-3}$ and 61.83 % at $10^{17} cm^{-3}$ respectively. The V_{oc} decreases drastically from 0.6748 V at $10^{15} cm^{-3}$, to a minimum value of 0.4757 V at $10^{18} cm^{-3}$ and thereafter improves to 0.7261 V at $10^{20} cm^{-3}$. The J_{sc} however decreases from 11.05 mA/cm^2 at $10^{15} cm^{-3}$ to 5.98 mA/cm^2 at $10^{20} cm^{-3}$.

The lowering of J_{sc} can be attributed to a decreasing ratio between charge carrier generation and recombination rates in the main portions of the photoactive layer (Trukhanov *et al*., 2011). The *FF* decreases with increasing doping concentration due to increase in series resistance in the cell which can be attributed to the increased presence of majority carriers (holes) in the p-type region with increased acceptor doping of the perovskite material (Bag *et al*., 2020) hence reduced series resistance in the cell. The *FF* varies monotonically with the *PCE* hence the similar pattern of behavior. The V_{oc} decreases due to decreasing share of radiative recombination at open-circuit condition. The optimal efficiency is deduced, showing that charge carriers are collected and transported more efficiently at $N_A = 10^{15} cm^{-3}$. Figure 14 shows different *J-V* Spectra with increasing doping concentrations of $Cs_{0.8}Rb_{0.2}SnI_3$ absorber layer.

Figure 14

J-V Spectra with increasing doping concentrations of $Cs_{0.8}Rb_{0.2}SnI_3$ *absorber layer.*

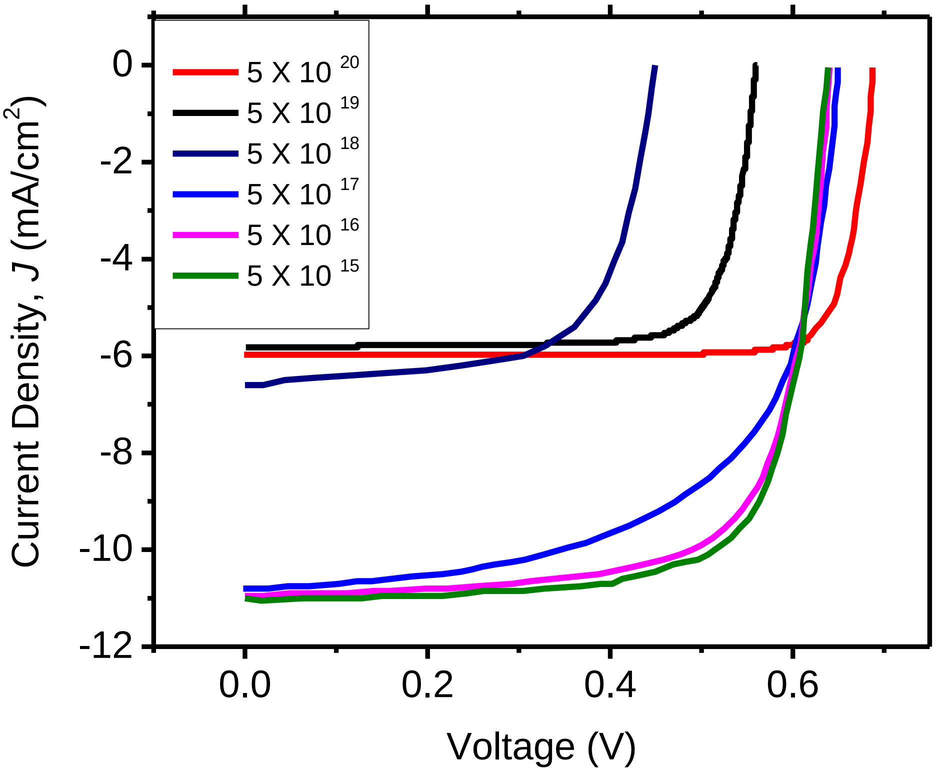

The large gap is a visual representation of the variation of current density with increasing voltage as shown in Figure 14. The large gap is an indicator of the improvement in the properties of the solar cell as a result of doping of the perovskite absorber layer in the solar cell. This is as a result of the increase in charge concentration in the cell hence increasing the photo-generated current per unit area delivered by the solar cell when the terminals of the solar cell are in contact with each other (Araoz, 2009).

Effect of Electron Transport Layer (PCBM) Thickness, Doping Concentration and Conduction Band Offset on lead – free $Cs_{1-X}Rb_XSnI_3$ perovskite solar cell parameters.

(a) Electron Transport Layer, ETL (PCBM) Thickness

The optimum thickness of the ETL layer plays a crucial role in terms of stability, efficiency, and other photovoltaic parameters of perovskite-based solar cells. Figure 15 shows the effect of ETL (PCBM) thickness on the device performance. The V_{oc}, J_{sc}, *FF* and *PCE* are shown to increase significantly with increasing PCBM thickness. The ETL (PCBM) thickness is varied from 20 nm to 100 nm. The V_{oc} increases from 0.47 V at 20 nm to 0.48 V at 100 nm. The J_{sc} increases from 5.98 mA/cm^2 at 20 nm to 7.29 mA/cm^2 at 100 nm. The *PCE* increases from 1.48 % at 20 nm to 2.32 % at 100 nm. The *FF* increases from 65.48 % at 20 nm to 66.36 % at 100 nm. The increase in V_{oc} can be attributed to low recombination due to efficient charge carrier separation at the PCBM/$Cs_{0.8}Rb_{0.2}SnI_3$ interface. The increase in J_{sc} could be due to an increase in light transmittance through the thicker ETL layer. The increase in *FF* with the increasing PCBM thickness is attributed to a decrease in series resistance in the device. The strong built-in potential ascribed to decreased trap states and interfacial charge carrier provides an enhanced driving force to inhibit the back transfer of electrons from the ETL to perovskite more effectively with increasing PCBM thickness. The 100 nm PCBM layer in the perovskite exhibits the best performance and hence optimum ETL thickness in this study.

Figure 15

Effect of Electron Transport Layer, ETL (PCBM) Thickness on $Cs_{1-X}Rb_XSnI_3$ *perovskite solar cell parameters.*

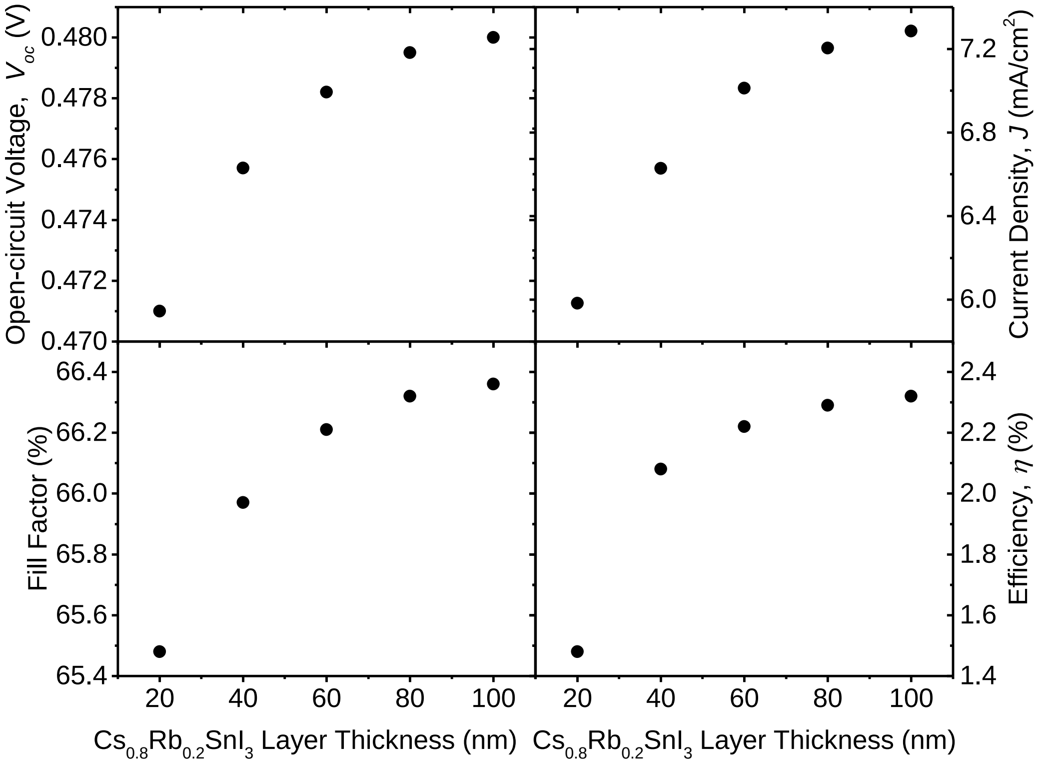

(b) Electron Transport Layer, ETL Doping Concentration

Electron transport layer, ETL plays a central role in the collection of generated charge carriers in PSCs. Doping concentration is a measure of the interaction of charges in the band. Figure 16 shows the effect of ETL doping concentrations on the photovoltaic performance of the PSCs. The V_{oc}, J_{sc}, *FF* and *PCE* are shown to eventually increase significantly with increasing doping concentration of the ETL layer despite initial variations. The doping concertation of the ETL (PCBM) layer is varied from$1 \times 10^{16} - 1 \times 10^{21} cm^{-3}$. The J_{sc} increases from 3.91 mA/cm^2 at $1 \times 10^{16} cm^{-3}$ to 7.33 mA/cm^2 at $1 \times 10^{21} cm^{-3}$. The *PCE* increases from 1.72 % at $1 \times 10^{16} cm^{-3}$ to a maximum value of 3.72 % at $1 \times 10^{21} cm^{-3}$. The *FF* first increases from 69.80 % at $1 \times 10^{16} cm^{-3}$, peaks at 77.51 % at $1 \times 10^{18} cm^{-3}$, decreases to 65.97 % at $1 \times 10^{20} cm^{-3}$and finally increases to 70.19 % at $1 \times 10^{21} cm^{-3}$. The V_{oc} first decreases from 0.63 V at $1 \times 10^{16} cm^{-3}$ to a minimum value of 0.46 V at $1 \times 10^{20} cm^{-3}$ and leaps to 0.72 V at $1 \times 10^{21} cm^{-3}$. High ETL doping concentrations cause high electron conductivity and provide low resistance to the flow of electrons that are swept away from the perovskite absorber layer due to the presence of a strong built-in electric field. This corroborates with the increase *FF* due to decreasing series resistance with increased doping. A steep increase in the V_{oc} is due to the increased separation of the Quasi Fermi levels in non-equilibrium conditions. For low doping value of ETL Quasi Fermi levels are closer, whereas, for a high amount of doping, they are more separated from each other. High ETL doping concentration leads to an increase in the width of the depletion region and hence decreases the recombination rate at the bulk of the absorber (Agha & Algwari, 2021). The built-in electric field across the device with increased doping facilitates separation of carriers. This results in increase in the J_{sc} and eventually the *PCE*. The optimal *PCE* (3.72 %) corresponds to a high doping concentration at $1 \times 10^{21} cm^{-3}$ which is therefore determined to be the optimal doping concentration.

Figure 16

Effect of Electron Transport Layer, ETL (PCBM) Doping Concentration on $Cs_{1-X}Rb_XSnI_3$ perovskite solar cell parameters.

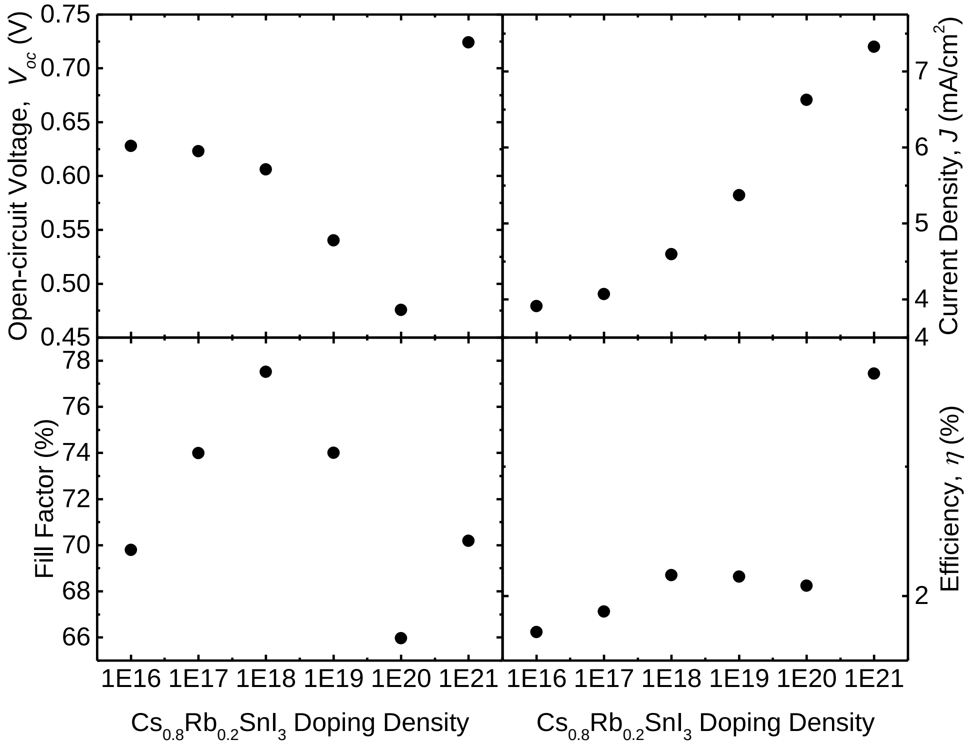

(a) Electron Transport Layer, ETL CBO

The [6, 6]-Phenyl-C61-butyric acid methyl ester (PCBM) was used as ETL and its electron affinity varied to get the intended CBO. Fig. 10 shows the energy band diagram for the perovskite solar cell with (a) – 0.28 eV and (b) + 0.22 eV CBO of the ETL/Absorber interface. The photo generated electron flow towards the metal back contact and are not interrupted when the CBO is increasingly positive. On the other hand, with increasing negative CBO, there is inhibition the flow of photo generated electrons towards the metal back contact hence the reducing *PCE* (Sharbati & Sites, 2014).The activation energy E_a for carrier recombination becomes lower than E_g of the absorber for a negative CBO hence interface recombination becomes the main recombination mechanism (Tanaka *et al.*, 2009). For a positive CBO, there is an optimal performance due to low interface recombination and likely selective charge collection.

Negative CBO increases interface recombination due to increased accumulation of electrons and holes for high defect density at interface which enhances recombination and low charge output as shown in Figure 17. (*PCE* against CBO for interface densities 10^{12} cm^{-3} and 10^{15} cm^{-3}). Both *PCE* and current density are heavily affected by interface defect densities. However, current density seemed not to be significantly affected by the CBO due to excess carrier density predominantly influencing carrier recombination at the ETL/Absorber. For improved cell performance, positive CBO with minimal interface defects is favorite (Akoto *et al*., 2023). From the above discussion, the optimal position for the conduction band of the ETL below the corresponding photoactive absorber bands respectively is derived at + 0.22 eV.

Figure 17

Effect of Electron Transport Layer Conduction Band Offset (CBO) on $Cs_{1-X}Rb_XSnI_3$ perovskite solar cell parameters

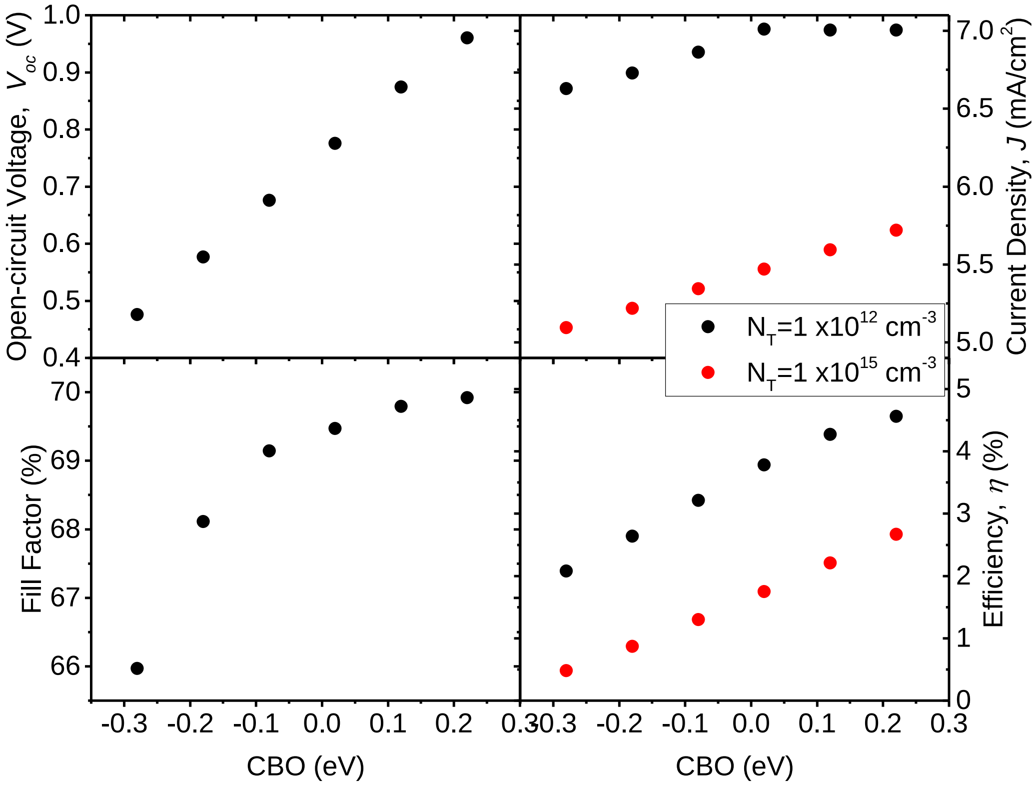

Effect of Different work functions of ITO front contact of lead – free $Cs_{1-X}Rb_XSnI_3$ perovskite solar cell Parameters.

The interface between the carrier transport layer (HTL/ETL) and the front transparent contact layer plays an important role for carrier transfer, and the deficit in V_{oc} if there occurs energy level (Fermi level) mismatch. The mostly used front transparent contact in perovskite solar cells is ITO which has work-function range 4.5 eV – 4.7 eV at undoped condition (Park *et al*., 1996). This low work function level poses significant energy mismatch for inverted planar (p-i-n) perovskite solar cells, where light enters from the HTL layer, because HTL materials usually have a higher Fermi level.

The situation aggravates for inverted planar $Cs_{0.8}Rb_{0.2}SnI_3$ without a HTL layer. It can be improved by utilizing different doped – ITO materials like Chlorinated ITO (Cl: ITO) (P.-R. Huang *et al*., 2013) which are reported to have better WF in the range of 4.9 eV – 5.6 eV. The V_{oc} increased steadily from 0.4757 V at 4.7 eV to 0.5018 at 5.3 eV. The J_{sc} increased from 6.63 mA/cm^2 at 4.7 eV to 11.24 mA/cm^2 at 5.3 eV. The FF increases from 65.97 % at 4.5 eV to 72.54 % at 5.3 eV. The PCE increases from 2.08 eV to 4.09 % at 5.3 eV as shown in figure 18. All the parameters levels off with increasing work function until 5.6 eV after attaining a maximum at 5.3 eV since maximum carrier extraction and transport has been attained. The high work function of ITO creates a high conductive path for carrier extraction hence reducing series resistance in the cell hence the enhanced FF in the device. The built-in potential, V_{bi} across the device, which is responsible for exciton dissociation and the upper limit for the attainable V_{oc}, is increased with increasing work function hence the increasing V_{oc} values (C. Zhang *et al*., 2014). Increase in work function subsequently leads to the better energy alignment hence better carrier extraction necessitating the increase in J_{sc} values. The optimum ITO work function is selected at 5.3 eV since a high work function enables a much simpler device structure hence the improved *PCE* in the device.

Figure 18

Effect of Different work functions of front contact on the parameters of Lead –free $Cs_{1-X}Rb_XSnI_3$ *perovskite solar cell parameters*

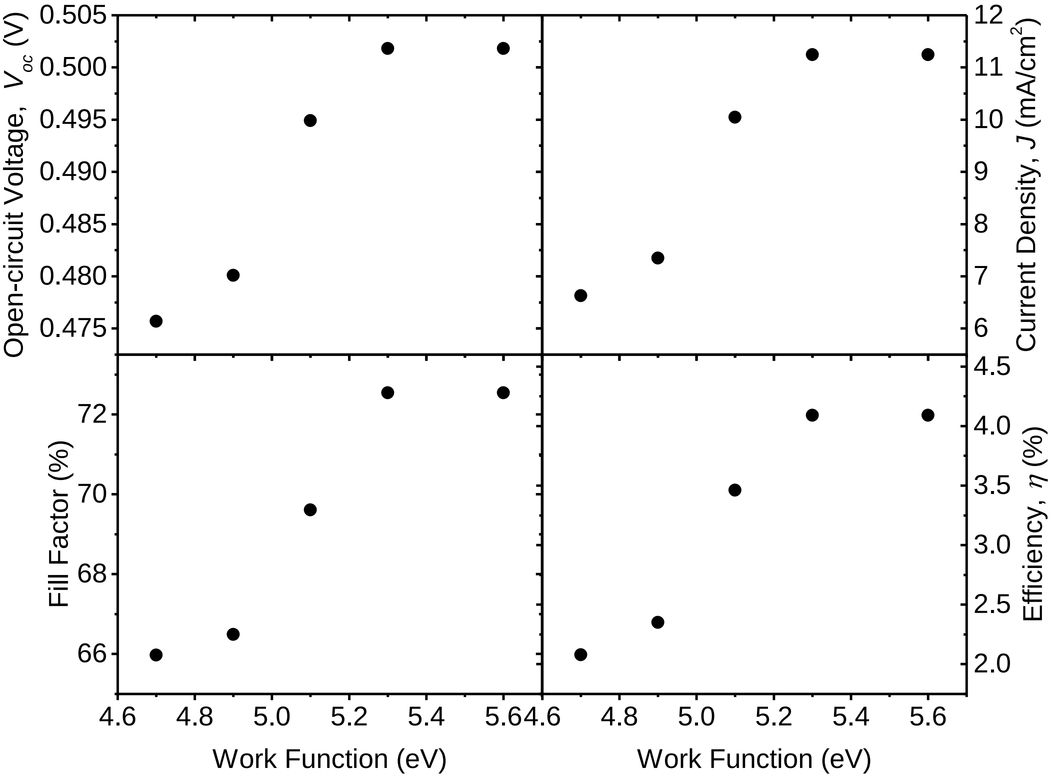

4.4 Numerical Simulation of Monolithic Lead – free Cs1-xRbXSnI3 Perovskite – silicon 2T tandem solar cell

Tandem solar cells exploit sunlight better because of the ability to split the solar spectrum into multiple bands that can be more efficiently converted by the different cells in the device. To trap long solar radiation wavelengths, a perovskite cell is introduced on top of a single-junction silicon solar cell to create a tandem structure. By using a top cell material, with a band gap higher than 1.124 eV of silicon, high energy photons generate a voltage approximately twice that which silicon generates (Baloch *et al.*, 2018). In perovskite – silicon tandem device, the high energy photons are absorbed by the perovskite cell, while the low energy photons are absorbed by the Si bottom cell. The $Cs_{1-x}Rb_XSnI_3$ perovskite with ~1.4 eV bandgap is a compatible contender as a material for the top cell in tandem configuration (Marshall *et al*., 2018). Thicker Silicon layers are required to absorb the same amount of light as any thin layer of direct bandgap material. In this study the effect of absorber thickness, doping concentration and defect density were studied in detail.

4.4.1 Effect of Perovskite thickness variation in lead – free Cs1-XRbXSnI3 perovskite – Silicon 2T Tandem Solar Cell

The thickness of the absorber layer is one of the critical parameters that has a considerable effect on the photovoltaic characteristics of a tandem solar cell. The thickness of $Cs_{1-X}Rb_XSnI_3$ perovskite absorber layer was varied from 100 nm to 1 μm to determine its influence on the lead - free $Cs_{1-X}Rb_XSnI_3$ perovskite – Si tandem solar cell. The range was arrived at as practical experimental limits within which the diffusion length lies. This change on the properties of the tandem solar cell is shown in figure 19. The *FF* decreases with increasing perovskite thickness from 85.86 % at 100 nm to 85.46 % at 1 μm. The V_{oc} slightly decreases from 0.79 V at 100 nm to 0.76 V at 1 μm with increasing thickness of the perovskite layer. The J_{sc} decreases drastically from 42. 74 mA/cm^2 at 100 nm to 14.23 mA/cm^2 at 1 μm.

The *PCE* decreases from 28.86 % at 100 nm to 9.22 % at 1 μm. The increase in *FF* suggests a decrease in series resistance in the cell with increasing perovskite absorber thickness. The decrease in V_{oc} is a measure of reduced exciton dissociation with increasing perovskite thickness (Scharber *et al*., 2006). The decrease in J_{sc} is due to increased carrier combination rate versus the carrier generation rate with increasing absorber thickness. The reduced exciton dissociation therefore reduce the carriers, increases recombination and hence decreases the efficiency (Duan *et al*., 2020).

Optimum perovskite thickness is realized at 100 nm which gives the highest efficiency (28.86 %).

Figure 19

Effect of Perovskite thickness variation on the properties of lead – free $Cs_{1-X}Rb_XSnI_3$ *perovskite – Silicon 2T Tandem Solar Cell*

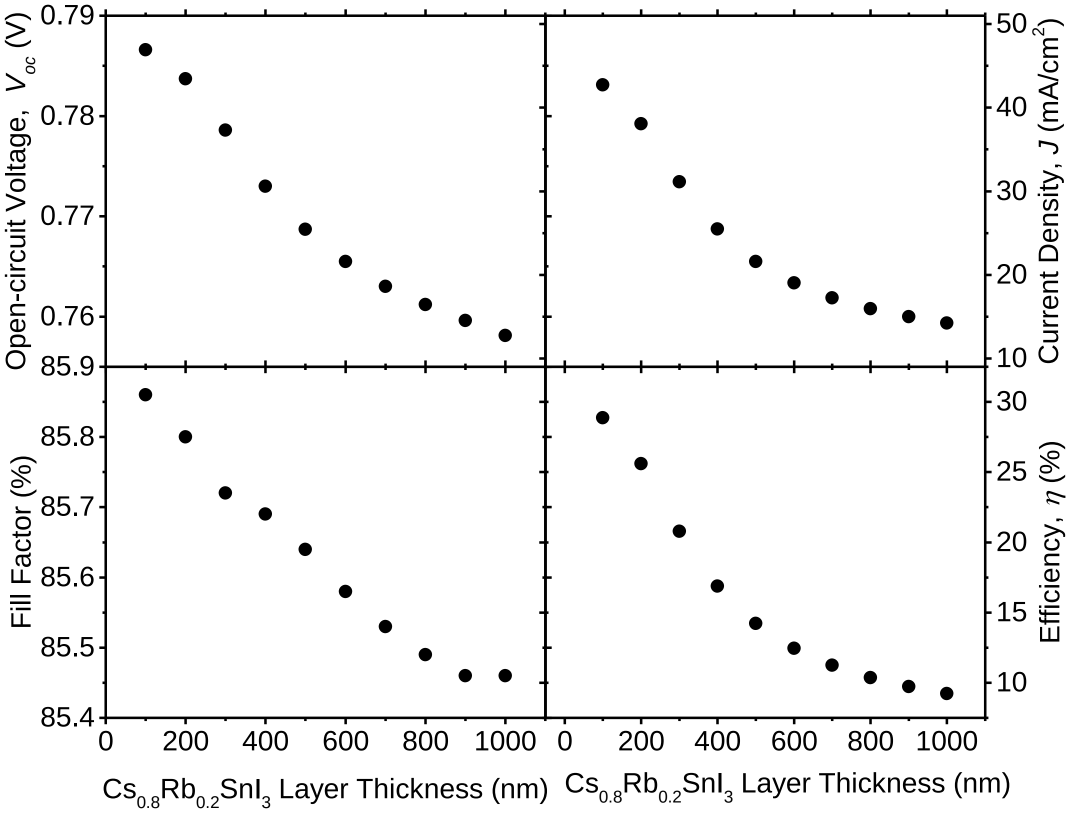

4.4.2 Effect of Silicon c-Si (p) thickness variation in lead – free Cs1-XRbXSnI3 perovskite – Silicon 2T Tandem Solar Cell

The c-Si (p) absorber layer thickness was varied from 50 μm to 400 μm to investigate the effect of the silicon absorber in the tandem solar cell. This range was arrived at considering experimental limitations (Terheiden *et al.*, 2015) . In figure 20, increase in the active layer thickness leads to a decrease in the V_{oc}, J_{sc}, *FF* and *PCE* in the solar cell. The J_{sc} of the device decreases from 41.04 mA/cm^2 at 50 μm to 40.42 mA/cm^2 at 400 μm. The V_{oc} values decrease from 0.79 V at 50 μm to 0.78 V at 400 μm with increasing thickness. The *FF* values decrease slightly from 85.87 % at 50 μm to 85.67 % at 400 μm.

The *PCE* values decrease slightly from 27.70 % at 50 μm to 27.12 at 400 μm with increasing c-Si (p) thickness. The V_{oc} decreases due to increased recombination in the thicker absorber layers. There is increased series resistance in the active layer with increasing thickness hence the dwindling values of *FF*. The decreasing J_{sc} points to a decrease in spectral response at the longer wavelength solar irradiance. Despite a large number of electron–hole pairs being generated suggested by the high efficiency, larger thicknesses reduce the charge collection while the photo absorption is constant thus reducing the efficiency of the cell (Melas-Kyriazi *et al*., 2011). Optimum silicon cell thickness is therefore determined at 200 μm, within the current experimental limits i.e. minimum thickness that is experimentally feasible (Terheiden *et al*., 2015).

Figure 20

Effect of Silicon c-Si (p) thickness variation on the properties of lead – free $Cs_{1-X}Rb_XSnI_3$ *perovskite – Silicon 2T Tandem Solar Cell*

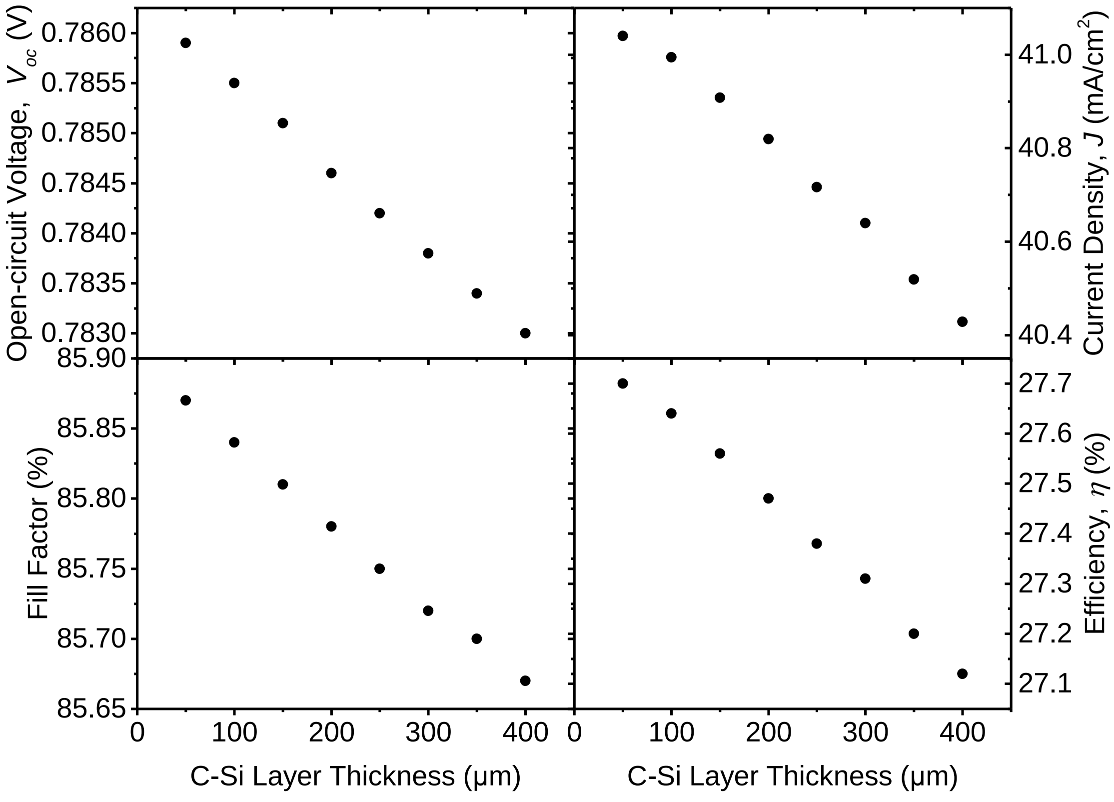

4.4.3 Doping concentration (ND) of perovskite Absorber layer in lead – free Cs1-XRbXSnI3 perovskite – Silicon 2T Tandem Solar Cell

Doping concentration refers to the quantity of electrical charge in the material. The doping concentration (N_D) of perovskite absorber layer was varied from $5 \times 10^{15} cm^{-3} - 5 \times 10^{20} cm^{-3}$ to determine the effect of doping the perovskite layer on the photovoltaic characteristics of the tandem solar cell. In figure 21 all the photovoltaic characteristics J_{sc}, V_{oc}, *FF* and *PCE* increase with increasing doping concentration of the perovskite absorber layer. The J_{sc} values increased from 40.99 mA/cm^2 at $5 \times 10^{15} cm^{-3}$, peaks at 42.96 mA/cm^2 at $5 \times 10^{18} cm^{-3}$, and thereafter decreases to 40.85 mA/cm^2 at $5 \times 10^{20} cm^{-3}$. The V_{oc} values increased from 0.78 V at $5 \times 10^{15} cm^{-3}$ to 0.80 V at $5 \times 10^{20} cm^{-3}$with increasing doping concentration. The *FF* increases from 85.84 % at $5 \times 10^{15} cm^{-3}$to 85.97 at $5 \times 10^{20} cm^{-3}$. The PCE increases from 27.64 % at $5 \times 10^{15} cm^{-3}$, peaks at $5 \times 10^{19} cm^{-3}$ (29.37 %) and sharply drops to 28.18 % at $5 \times 10^{20} cm^{-3}$.

There is increase in the in built voltage, V_{bi} with increasing doping concentration which causes increase in J_{sc} following introduction of the majority carriers in the perovskite layer. The saturation current of the device increases with the increase in the concentration of the acceptor and as a result increases the V_{oc} (Zhong *et al.*, 2014). The decrease in series resistance in the cell is attributed to the increased presence of majority carriers with increased doping of the perovskite material hence the rise in *FF*. An increase in doping density in the perovskite layer enhances device performance due to built-in electric field across the device. The optimum perovskite doping concentration is determined at $5 \times 10^{19} cm^{-3}$ since it yields the maximum *PCE* (29.37 %) in the solar cell.

Figure 21

Effect of doping concentration (N_D) of perovskite Absorber layer on the photovoltaic properties of lead – free $Cs_{1-X}Rb_XSnI_3$ perovskite- Silicon 2T Tandem Solar Cell

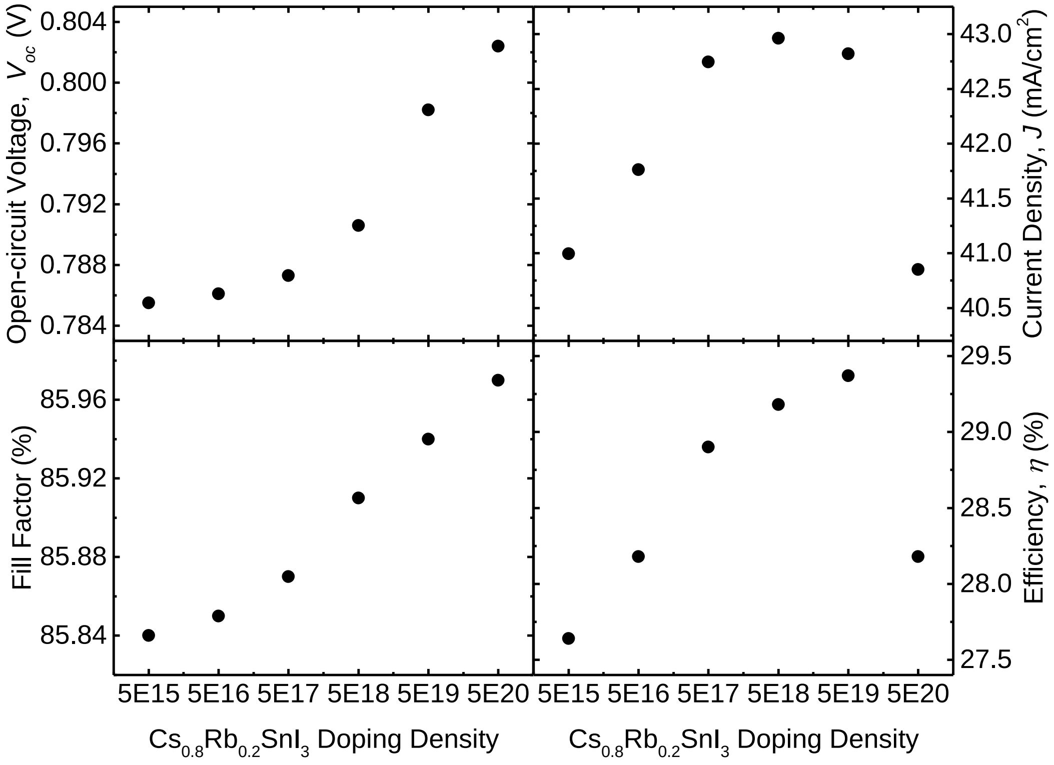

4.4.4 Doping concentration (ND) of Silicon Absorber layer in lead – free Cs1-XRbXSnI3 perovskite – Silicon 2T Tandem Solar Cell

Doping concentration (N_D) of silicon absorber layer was varied from $5 \times 10^{15} cm^{-3} - 5 \times 10^{20} cm^{-3}$ to establish the effect of doping the crystalline silicon absorber layer on the photovoltaic properties of tandem solar cell. In figure 22 the J_{sc} decreases while the *FF* and *PCE* first increase, peak and thereafter decrease with increasing doping concentration of the perovskite absorber layer. The J_{sc} values decreased from 41.13 mA/cm^2 at $5 \times 10^{15} cm^{-3}$ to 1.66 mA/cm^2 at $5 \times 10^{20} cm^{-3}$. The *FF* increases from 85.32 % at $5 \times 10^{15} cm^{-3}$, peaks at $5 \times 10^{17} cm^{-3}$ (85.89 %) and thereafter decrease to 84.87 % at $5 \times 10^{20} cm^{-3}$. The *PCE* slightly increases from 27.56 % at $5 \times 10^{15} cm^{-3}$, peaks at $5 \times 10^{16} cm^{-3}$ (27.64 %) and sharply drops to 1.02 %

at $5 \times 10^{20} cm^{-3}$. Higher carrier density increases the recombination process, reduce the probability of collecting electrons generated from photons and increase in the in built voltage, V_{bi} due to increase of the photocurrent hence necessitating decrease in J_{sc}. Increases in *FF* are due to the decrease in series resistance following the introduction of majority carriers. The slight increase in the *PCE* of device with active layer can be attributed photo-generated electrons and holes being separated effectively (Guo *et al*., 2021). Doping levels in the absorber layer influences the defect density and hence device performance. Further, the quality of the film in a solar cell deteriorates with increased doping. Optimum doping concentration of the silicon absorber layer is determined at $5 \times 10^{16} cm^{-3}$, which corresponds to the highest PCE at 27.64%.

Figure 22

Effect of Doping concentration (N_D) of Silicon Absorber layer on the photovoltaic characteristics of lead – free $Cs_{1-X}Rb_XSnI_3$ perovskite – Silicon 2T Tandem Solar Cell

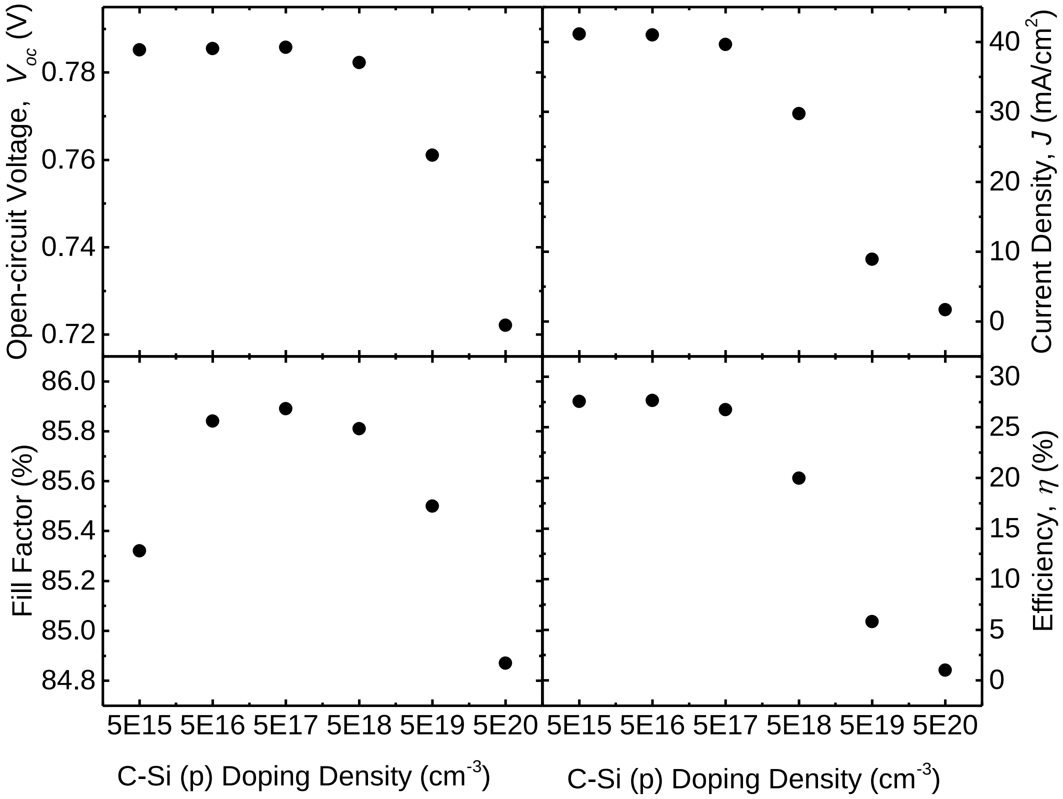

4.4.5 Effect of defect density of perovskite layer in lead – free $Cs_{1-X}Rb_XSnI_3$ perovskite – Silicon 2T Tandem Solar Cell

Absorber layer defect density is a significant factor that contributes to performance optimization of a tandem solar cell. The defect density of the material influences the structure and quality of the active perovskite absorber layer and hence the rate of recombination of charge carriers' in a material. The perovskite absorber layer defect density was varied from 10^{12} cm^{-3} to 10^{16} cm^{-3} to study its influence on the tandem device performance. It is expected that for an increase in defect density, both minority carrier lifetime and mobility should decrease causing a decrease in the open-circuit voltage. In figure 23, the electrical performance of all the parameters are strongly affected. The J_{sc},V_{oc}, FF and PCE all decrease with increasing perovskite defect density in the solar cell. The J_{sc} values decreases from 43.32 mA/cm^2 at 10^{12} cm^{-3} to 31.93 mA/cm^2 at $10^{16} cm^{-3}$. The J_{sc} values decrease from 0.7869 V to 0.7793 V with increasing defect density. The FF values decrease from 85.86 % to 85.72 % with increasing defect density. The PCE values decrease from 29.27 % to 21.33 % with increasing defect density. Optimum perovskite defect density is $1 \times 10^{13} cm^{-3}$ to achieve a more realistic cell. With the increase in defect density, both minority carrier lifetime and mobility decrease causing a decrease in the V_{OC}. The rate of recombination to carrier generation of charge carriers increases hence the reduction in J_{sc} which eventually degrade the performance and outcome of the device (Hussain *et al*., 2021).

Figure 23

Effect of defect density of perovskite layer in lead – free $Cs_{1-X}Rb_XSnI_3$ perovskite – Silicon 2T Tandem Solar Cell

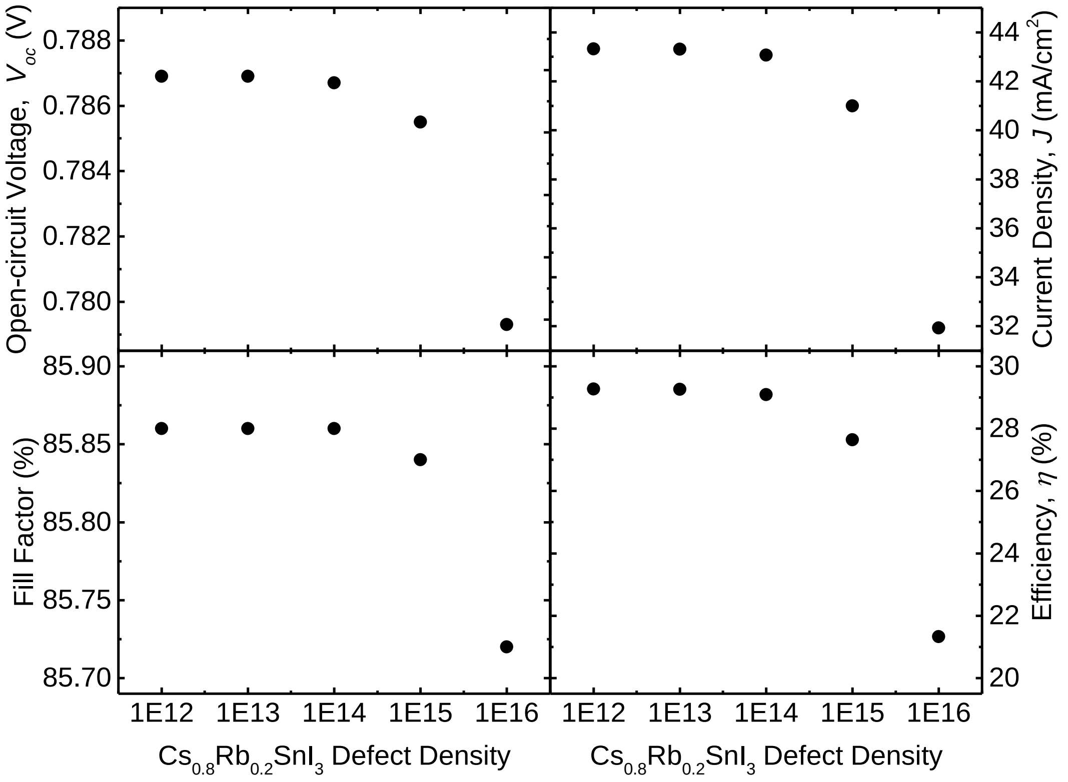

4.4.6 Effect of defect density of Silicon in lead – free $Cs_{1-X}Rb_XSnI_3$ perovskite – Silicon 2T Tandem Solar Cell

Defects in a material originate from added impurities or crystallographic defects such as vacancies or dislocations. The more defects a material has, the less the photocurrent of the solar cell due to increased recombination centers reducing its minority carrier lifetime. The effect of varying the C- Si (p) absorber layer defect density in the lead – free $Cs_{1-X}Rb_XSnI_3$ perovskite – Silicon 2T Tandem Solar Cell is investigated as shown in figure 24. The silicon absorber layer defect density is varied from $10^{12}cm^{-3}$ – $10^{16}cm^{-3}$. The J_{sc} values decreases from 40.99 mA/cm^2 at 1 x $10^{12}cm^{-3}$ to 11.49 mA/cm^2 at 1 x $10^{16}cm^{-3}$. The V_{oc} values decrease from 0.79 V at 1 x $10^{12}cm^{-3}$ to 0.61 V at 1 x $10^{16}cm^{-3}$ with increasing defect density. The *FF* values decrease from 85.84 % at $1x10^{12}cm^{-3}$to 82.77% at $1x10^{16}cm^{-3}$ with increasing defect density. The *PCE* values decrease from

27.64 % at 1 x 10^{12}cm^{-3} to 5.80 % at 1 x 10^{16}cm^{-3} with increasing defect density. Optimum silicon absorber defect density is determined at 1 x 10^{12}cm^{-3}. With the increase in defect density, the drop in efficiency can be attributed to increased rate of recombination, which leads to higher scattering and reduced diffusion length , so the device performance decreases (Nalianya *et al.*, 2021).

Figure 24

Effect of defect density of Silicon in lead – free $Cs_{1-X}Rb_XSnI_3$ perovskite – Silicon 2T Tandem Solar Cell

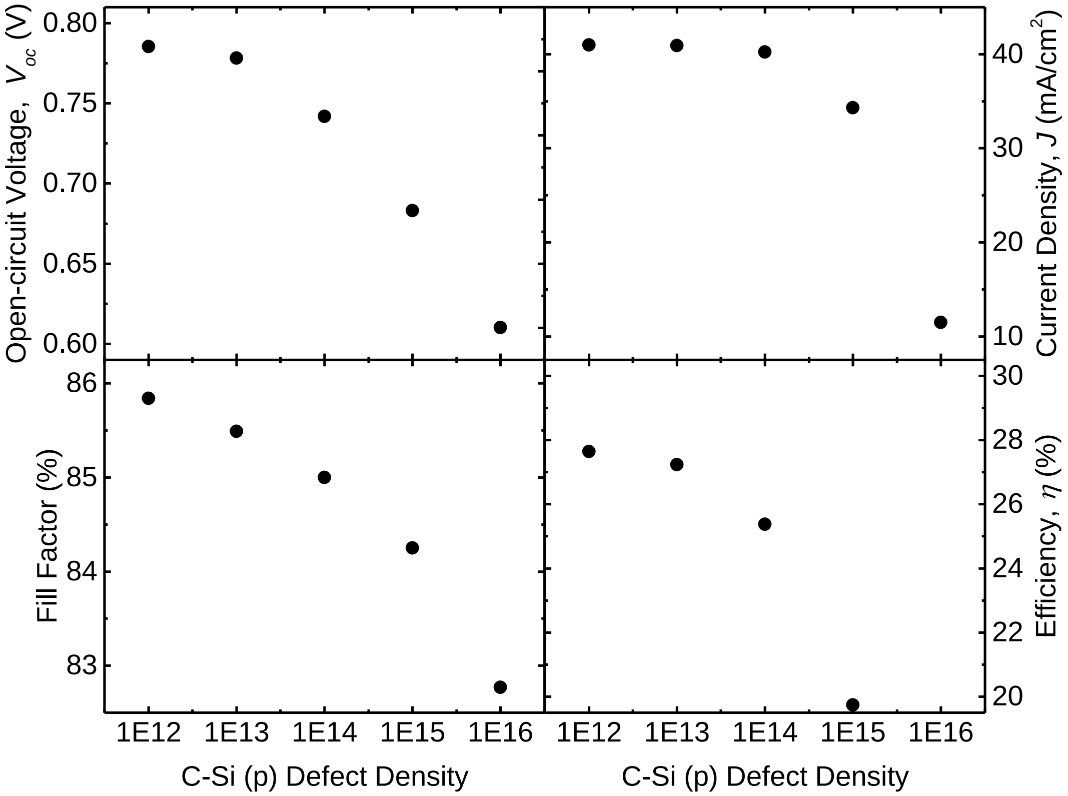

Optimum values obtained in this study (Table 9) of both the top and bottom cells in the lead – free $Cs_{1-X}Rb_XSnI_3$ perovskite – Silicon 2T tandem solar cell were used to obtain the encouraging results (Table 10). Simulation results show that optimized absorber thickness, defect and doping densities, ETL thickness, doping densities and CBO and front contact of $Cs_{1-X}Rb_XSnI_3$ perovskite lead to high efficiencies.

Table 9

Optimized parameters of $Cs_{1-X}Rb_XSnI_3$ Perovskite and tandem solar cells

Cell		$Cs_{1-X}Rb_XSnI_3$ Perovskite	Tandem Solar Cell	
			Top Cell	Bottom Cell
Absorber	Thickness	500 nm	100 nm	200 µm
	Doping Density	5×10^{15}	5×10^{19}	5×10^{16}
	Defect Density	1×10^{15}	1×10^{14}	1×10^{12}
ETL	Thickness	100 nm		
	Doping Density	1×10^{21}		
	CBO	+ 0.22 eV		
Work Function of ITO Front contact			5.3 eV	

Table 10

Initial and optimized parameters of $Cs_{1-X}Rb_XSnI_3$ Perovskite and lead – free $Cs_{1-X}Rb_XSnI_3$ perovskite – Silicon 2T tandem solar cell (s).

Solar Cell		Open Circuit Voltage, V_{oc} (V)	Short Circuit Current Density, J_{sc} (mA/cm^2)	Fill Factor, FF (%)	Power Conversion Efficiency, PCE (%)
$Cs_{1-X}Rb_XSnI_3$ Perovskite	Initial	0.4757	6.63	65.97	2.08
	Final	1.0356	23.76	83.18	20.46
Crystalline Silicon		0.7400	43.29	83.30	26.68
$Cs_{1-X}Rb_XSnI_3$ perovskite – Silicon tandem	Initial	0.7855	40.99	85.84	27.64
	Final	0.7992	43.39	85.98	29.82

Figure 25

Optimized and initial J –V curves for the perovskite, silicon, initial and final tandem solar cell (s)

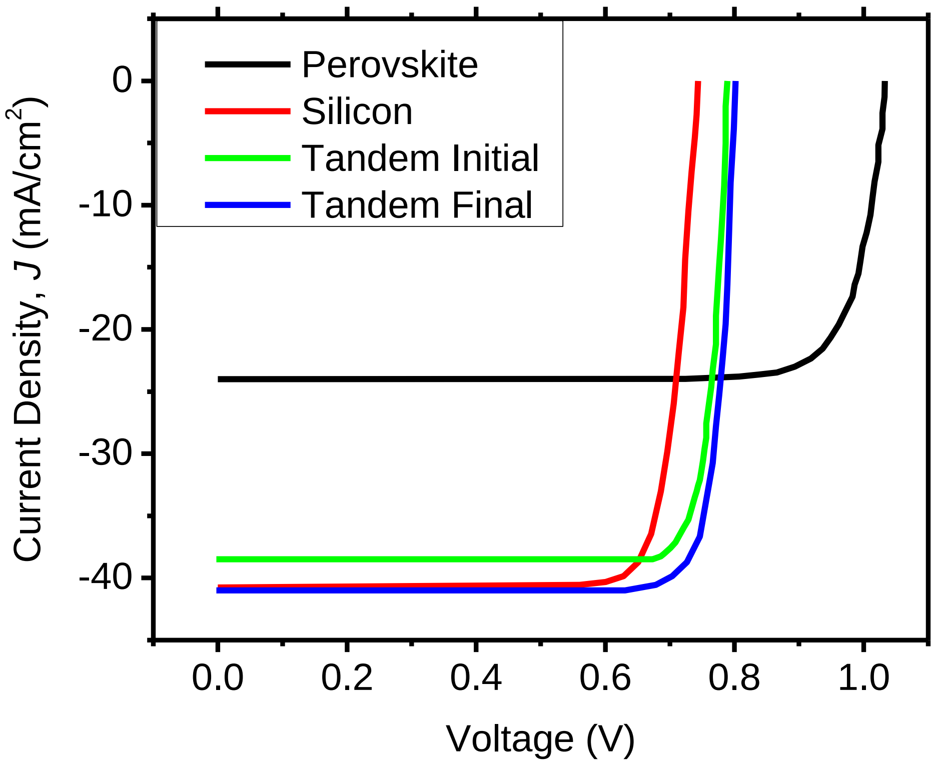

Figure 25 displays the *J* – *V* curves of different cells as indicated. The gaps are therefore a clear indication and visual representation of the different J – V characteristic properties of the simulated cells: silicon cell and perovskite cells, an improvement realized by aggregation of the two cells by forming a tandem solar cell and an improvement of the initial tandem solar cell by optimization techniques used in this study.

CHAPTER FIVE

SUMMARY, CONCLUSIONS AND RECOMMENDATIONS

5.1 Introduction

In the former chapters a report of the photovoltaic performance of lead free $Cs_{0.8}Rb_{0.2}SnI_3$, silicon solar cell and lead – free $Cs_{0.8}Rb_{0.2}SnI_3$ – Silicon 2T tandem solar cell has been presented. In this chapter a summary of the study, conclusions made from the study and the recommendations are discussed.

5.2 Summary

In this study $Cs_{0.8}Rb_{0.2}SnI_3$ perovskite solar cell, crystalline silicon solar cell and lead – free $Cs_{0.8}Rb_{0.2}SnI_3$ – silicon 2T tandem solar cell were successfully modelled and simulated by SCAPS 1D. Numerical modeling provides a better and easier way to understand a device’s behavior. The modeling of solar cells uses physical parameters of material which are taken as input for the simulation software. This modelling involved solving semiconductor basic equations like the electrons and holes continuity equation, the Poisson equation relating the charge to electrostatic potential, and the carrier transport equations by the simulation software SCAPS 1D.

5.2.1 Numerical Simulation of Lead – Free $Cs_{1-X}Rb_xSnI_3$ and Silicon Solar Cells

This study involved modelling of the $Cs_{0.8}Rb_{0.2}SnI_3$ perovskite solar cell by using SACPS 1D. The initial values of parameters for each layer of the cell were obtained from literature. These parameters were varied in the simulation to determine their impact on the performance of the solar cell. The different parameters such as absorber thickness, doping concentration and defect density, electron transport layer (ETL) thickness, doping concentration and conduction band offset (CBO) and work function of the ITO front contact in the $Cs_{0.8}Rb_{0.2}SnI_3$ perovskite were then optimized.

5.2.2 Numerical Simulation of Monolith Lead – Free Cs1-XRbXSnI3 – Silicon 2T Tandem Structure.

This part of the study involved simulating the properties of lead – free $Cs_{0.8}Rb_{0.2}SnI_3$ – silicon 2T tandem solar cell solar cell by using Solar cell capacitance simulator (SCAPS ver.3.3.03). Different parameters such as thickness, doping concentration, and defect density of the two absorber layers in lead – free $Cs_{0.8}Rb_{0.2}SnI_3$ – silicon 2T tandem solar cell are investigated in detail. Optimized parameters were used to simulate the photovoltaic characteristics of the final tandem solar cell.

5.3 Conclusion

5.3.1 Numerical Simulation of Lead – Free Cs1-XRbxSnI3 and Silicon Solar Cells

The Lead free $Cs_{0.8}Rb_{0.2}SnI_3$ perovskite cell appropriate absorber thickness and low defect density improved solar power conversion efficiency due to the enhancement of electron – hole generation and low recombination rate. The electron transport layer (PCBM) thickness ensures high carrier concentration and mobility and doping density ensured effective carrier collection. Appropriate carrier doping concentration ensured heightened built-in electric field. The optimized solar cell constitutes improved properties of the solar cell with a PCE of 20.46 %.

5.3.2 Numerical Simulation of Monolith Lead – Free Cs1-XRbXSnI3 – Silicon 2T Tandem Structure

This part of the study further investigated the properties of lead – free $Cs_{0.8}Rb_{0.2}SnI_3$ – Silicon 2T tandem solar cell. The optimum perovskite thickness in the tandem cell ensured maximum exciton dissociation. Doping ensured increase in presence of majority carriers hence built in electric field across the cell. The optimum silicon thickness in the tandem cell ensured efficient charge collection. Doping ensured decreased resistance and increased optical absorption. The low defect densities realized in the silicon and perovskite layers of the tandem cell reduced the number of trap states where recombination takes place. Optimized ITO work function of the front contact ensured efficient electron transportation. The reassuring power conversion efficiency of 29.82 % is obtained after optimization of all the parameters. Increased efficiency is expected with further research on fabrication process compatibility with the absorber materials. The films are used in generating renewable energy from solar using novel low cost and earth-abundant materials.

5.4 Recommendations

5.4.1 Policy Recommendations

Solar power generation is one of the few low-carbon energy sources that can be scaled up to extremely large scales as one of the steps toward attaining Sustainable Development Goal 7: affordable, reliable, sustainable, and modern energy for all. To realize this, further development is needed to achieve a considerable rise in technology, price, and performance, which includes:

i. A long term approach towards the technological development in installed solar producing capacity by improving the efficiency of solar cells especially by embracing cost effective new advancements such as numerical modelling.

ii. Supportive environment for creation of innovative business models, to fuel investment in residential solar systems and efficient subsidies for solar deployment to ensure a much broader photovoltaic penetration and hence generation.

5.4.2 Recommendations for further research

The study of charge transport and recombination in lead – free $Cs_{1-X}Rb_XSnI_3$ perovskite and lead – free $Cs_{1-X}Rb_XSnI_3$ perovskite – Silicon 2T tandem solar cells still remains explorable at fundamental levels. Considering the work carried out in this thesis, the following areas require further investigation:

i. Simulation of this cell structure (s) using DFT approach to study electronic structure calculations and quantum-mechanical molecular dynamics, from first principles

ii. Optical, structural and morphological characterization of the structures of the solar cell (s) in order to improve the solar cell (s)

iii. Study transport and recombination mechanism of the solar cell (s) architectures with a hole transport layer.

REFERENCES

Agha, D. N. Q., & Algwari, Q. T. (2021). The influence of the interface layer between the electron transport layer and absorber on the performance of perovskite solar cells. *IOP Conference Series: Materials Science and Engineering*, *1152*(1), 12033.

Akoto, E., Isahi, V., Odari, V., Maghanga, C., & Nyongesa, F. (2023). MONOLITH Cs1-XRbXSnI3 PEROVSKITE-SILICON 2T TANDEM SOLAR CELL USING SCAPS-1D. *Results in Optics*, 100470.

Almansouri, I., Ho-Baillie, A., Bremner, S. P., & Green, M. A. (2015). Supercharging silicon solar cell performance by means of multijunction concept. *IEEE Journal of Photovoltaics*, *5*(3), 968–976.

Aman, G., Jahangir, K., Usman, Y., Ghazi, E., Nowsherwan, A., Khizer Jahangir, E., Saleem, M. W., & Khalid, M. (2021). Numerical Modeling and Optimization of Perovskite Silicon Tandem Solar Cell Using SCAPS-1D. *Sch Bull*, *7*(7), 171–184. https://doi.org/10.36348/sb.2021.v07i07.004

Araoz, R. S. (2009). Chemical bath deposition of Zn (S,O) buffer layers and application in Cd-free chalcopyrite-based thin-film solar cells and modules. In *Helmholtz Zentrum Berlin*. Free University of Berlin.

Bag, A., Radhakrishnan, R., Nekovei, R., & Jeyakumar, R. (2020). Effect of absorber layer, hole transport layer thicknesses, and its doping density on the performance of perovskite solar cells by device simulation. *Solar Energy*, *196*, 177–182.

Baloch, A. A. B., Hossain, M. I., Tabet, N., & Alharbi, F. H. (2018). Practical efficiency limit of methylammonium lead iodide perovskite (CH3NH3PbI3) solar cells. In *The journal of physical chemistry letters* (Vol. 9, Issue 2, pp. 426–434). ACS Publications.

Benduhn, J., Tvingstedt, K., Piersimoni, F., Ullbrich, S., Fan, Y., Tropiano, M., McGarry, K. A., Zeika, O., Riede, M. K., & Douglas, C. J. (2017). Intrinsic non-radiative voltage losses in fullerene-based organic solar cells. *Nature Energy*, *2*(6), 1–6.

Bhatia, S. C. (2014). *Advanced renewable energy systems,(Part 1 and 2)*. CRC Press.

Bremner, S. P., Yi, C., Almansouri, I., Ho-Baillie, A., & Green, M. A. (2016). Optimum band gap combinations to make best use of new photovoltaic materials. *Solar Energy*, *135*, 750–757.

Burgelman, M., Decock, K., Niemegeers, A., Verschraegen, J., & Degrave, S. (2016). SCAPS manual. *February*.

Burgelman, M., Nollet, P., & Degrave, S. (2000). Modelling polycrystalline semiconductor solar cells. *Thin Solid Films*, *361*, 527–532. https://doi.org/10.1016/S0040-6090(99)00825-1

Bush, K. A., Manzoor, S., Frohna, K., Yu, Z. J., Raiford, J. A., Palmstrom, A. F., Wang, H.-P., Prasanna, R., Bent, S. F., & Holman, Z. C. (2018). Minimizing current and voltage losses to reach 25% efficient monolithic two-terminal perovskite–silicon tandem solar cells. *ACS Energy Letters*, *3*(9), 2173–2180.

Chapin, D. M., Fuller, C. S., & Pearson, G. L. (1954). A new silicon p-n junction photocell for converting solar radiation into electrical power. *Journal of Applied Physics*, *25*(5), 676–677.

Chen, Z., Yu, C., Shum, K., Wang, J. J., Pfenninger, W., Vockic, N., Midgley, J., & Kenney, J. T. (2012). Photoluminescence study of polycrystalline CsSnI3 thin films: Determination of exciton binding energy. *Journal of Luminescence*, *132*(2), 345–349.

Cheng, Y., & Ding, L. (2021). Perovskite/Si tandem solar cells: Fundamentals, advances, challenges, and novel applications. *SusMat*, *1*(3), 324–344.

Coulibaly, A. B., Oyedele, S. O., & Aka, B. (2019). Comparative study of lead-free perovskite solar cells using different hole transporter materials. *Modeling and Numerical Simulation of Material Science*, *9*(4), 97–107.

Devi, N., Parrey, K. A., Aziz, A., & Datta, S. (2018). Numerical simulations of perovskite thin-film solar cells using a CdS hole blocking layer. *Journal of Vacuum Science & Technology B, Nanotechnology and Microelectronics: Materials, Processing, Measurement, and Phenomena*, *36*(4), 04G105.

Du, H.-J., Wang, W.-C., & Zhu, J.-Z. (2016). Device simulation of lead-free CH3NH3SnI3 perovskite solar cells with high efficiency. *Chinese Physics B*, *25*(10), 108802.

Duan, L., Zhang, Y., Yi, H., Haque, F., Deng, R., Guan, H., Zou, Y., & Uddin, A. (2020). Trade-off between exciton dissociation and carrier recombination and dielectric properties in Y6-sensitized nonfullerene ternary organic solar cells. *Energy Technology*, *8*(1), 1900924.

Green, M. A., Hishikawa, Y., Dunlop, E. D., Levi, D. H., Hohl-Ebinger, J., Yoshita, M., & Ho-Baillie, A. W. Y. (2019). *Prog. Photovolt: Res. Appl*.

Green, M. A., Ho-Baillie, A., & Snaith, H. J. (2014). The emergence of perovskite solar cells. *Nature Photonics*, *8*(7), 506–514.

Guo, R., Zhao, Y., Zhang, Y., Deng, Q., Shen, Y., Zhang, W., & Shao, G. (2021). Significant performance enhancement of all-inorganic CsPbBr3 perovskite solar cells enabled by Nb-doped SnO2 as effective electron transport layer. *Energy & Environmental Materials*, *4*(4), 671–680.

Hao, F., Stoumpos, C. C., Chang, R. P. H., & Kanatzidis, M. G. (2014). Anomalous band gap behavior in mixed Sn and Pb perovskites enables broadening of absorption spectrum in solar cells. *Journal of the American Chemical Society*, *136*(22), 8094–8099.

Hao, L., Li, T., Ma, X., Wu, J., Qiao, L., Wu, X., Hou, G., Pei, H., Wang, X., & Zhang, X. (2021). A tin-based perovskite solar cell with an inverted hole-free transport layer to achieve high energy conversion efficiency by SCAPS device simulation. *Optical and Quantum Electronics*, *53*(9), 1–17.

Huang, L., & Lambrecht, W. R. L. (2016). Electronic band structure trends of perovskite halides: Beyond Pb and Sn to Ge and Si. *Physical Review B*, *93*(19), 195211.

Huang, P.-R., He, Y., Cao, C., & Lu, Z.-H. (2013). The origin of the high work function of chlorinated indium tin oxide. *NPG Asia Materials*, *5*(8), e57–e57.

Hussain, S. S., Riaz, S., Nowsherwan, G. A., Jahangir, K., Raza, A., Iqbal, M. J., Sadiq, I., Hussain, S. M., & Naseem, S. (2021). Numerical modeling and optimization of lead-free hybrid double perovskite solar cell by using SCAPS-1D. *Journal of Renewable Energy, 2021*.

Jäger, K., Jošt, M., Sutter, J., Tockhorn, P., Köhnen, E., Eisenhauer, D., Manley, P., Albrecht, S., & Becker, C. (2019). Improving Monolithic Perovskite/Silicon Tandem Solar Cells From an Optical Viewpoint. *Optical Devices and Materials for Solar Energy and Solid-State Lighting*, PM4C-2.

Jahangir, K., Usman, Y., Ghazi, E., Nowsherwan, A., Khizer Jahangir, E., Saleem, M. W., & Khalid, M. (2021). Numerical Modeling and Optimization of Perovskite Silicon Tandem Solar Cell Using SCAPS-1D. *Sch Bull*, *7*(7), 171–184. https://doi.org/10.36348/sb.2021.v07i07.004

Jehad, A. K., & Hamammu, I. (2013). Computer simulation on solving Poisson's equation for the silicon solar cell. *International Conference on Engineering and Computer Education - ICECE '2013, March*, 26–28.

Jiang, X., Zang, Z., Zhou, Y., Li, H., Wei, Q., & Ning, Z. (2021). Tin halide perovskite solar cells: an emerging thin-film photovoltaic technology. *Accounts of Materials Research*, *2*(4), 210–219.

Jošt, M., Kegelmann, L., Korte, L., & Albrecht, S. (2020). Monolithic perovskite tandem solar cells: a review of the present status and advanced characterization methods toward 30% efficiency. *Advanced Energy Materials*, *10*(26), 1904102.

Jošt, M., Köhnen, E., Morales-Vilches, A. B., Lipovšek, B., Jäger, K., Macco, B., Al-Ashouri, A., Krč, J., Korte, L., & Rech, B. (2018). Textured interfaces in monolithic perovskite/silicon tandem solar cells: advanced light management for improved efficiency and energy yield. *Energy & Environmental Science*, *11*(12), 3511–3523.

Jung, Y.-K., Lee, J.-H., Walsh, A., & Soon, A. (2017). Influence of Rb/Cs cation-exchange on inorganic Sn halide perovskites: from chemical structure to physical properties. *Chemistry of Materials, 29*(7), 3181–3188.

Ke, W., Stoumpos, C. C., & Kanatzidis, M. G. (2019). "Unleaded" perovskites: status quo and future prospects of tin-based perovskite solar cells. *Advanced Materials*, *31*(47), 1803230.

Khadka, D. B., Shirai, Y., Yanagida, M., & Miyano, K. (2020). Passivation of the Recombination Activities with Rubidium incorporation for Efficient and Stable Sn-HaP Solar Cells. *2020 47th IEEE Photovoltaic Specialists Conference (PVSC)*, 113–116.

Khallaf, H., Chai, G., Lupan, O., Chow, L., Heinrich, H., Park, S., & Schulte, A. (2009). In-situ boron doping of chemical-bath deposited CdS thin films. *Physica Status Solidi (A), 206*(2), 256–262.

Khatibi, A., Razi Astaraei, F., & Ahmadi, M. H. (2019). Generation and combination of the solar cells: A current model review. *Energy Science & Engineering*, *7*(2), 305–322.

Köhnen, E., Jošt, M., Morales-Vilches, A. B., Tockhorn, P., Al-Ashouri, A., Macco, B., Kegelmann, L., Korte, L., Rech, B., & Schlatmann, R. (2019). Highly efficient monolithic perovskite silicon tandem solar cells: analyzing the influence of current mismatch on device performance. *Sustainable Energy & Fuels*, *3*(8), 1995–2005.

Kojima, A., Teshima, K., Shirai, Y., & Miyasaka, T. (2009). Organometal halide perovskites as visible-light sensitizers for photovoltaic cells. *Journal of the American Chemical Society*, *131*(17), 6050–6051.

Kour, R., Arya, S., Verma, S., Gupta, J., Bandhoria, P., Bharti, V., Datt, R., & Gupta, V. (2019). Potential substitutes for replacement of lead in perovskite solar cells: A review. *Global Challenges*, *3*(11), 1900050.

Kurumi, S., Shimizu, Y., Kobayashi, S., Takase, K., & Suzuki, K. (2008). Synthesis of non-stoichiometric (LaO) CuS thin films by pulse laser deposition. *Applied Physics A*, *93*(3), 741–743.

Leijtens, T., Bush, K. A., Prasanna, R., & McGehee, M. D. (2018). Opportunities and challenges for tandem solar cells using metal halide perovskite semiconductors. *Nature Energy*, *3*(10), 828–838.

Li, Z.-Q., Ni, M., & Feng, X.-D. (2020). Simulation of the Sb2Se3 solar cell with a hole transport layer. *Materials Research Express*, *7*(1), 16416.

Lin, S., Zhang, B., Lü, T.-Y., Zheng, J.-C., Pan, H., Chen, H., Lin, C., Li, X., & Zhou, J. (2021). Inorganic Lead-Free B-γ-CsSnI3 Perovskite Solar Cells Using Diverse Electron-Transporting Materials: A Simulation Study. *ACS Omega*, *6*(40), 26689–26698.

Liu, P., Singh, V. P., Jarro, C. A., & Rajaputra, S. (2011). Cadmium sulfide nanowires for the window semiconductor layer in thin film CdS–CdTe solar cells. *Nanotechnology*, *22*(14), 145304.

Liu, Z. (2015). Supply and demand of global energy and electricity. *Global Energy Interconnection*, 101–182.

Löper, P., Moon, S.-J., De Nicolas, S. M., Niesen, B., Ledinsky, M., Nicolay, S., Bailat, J., Yum, J.-H., De Wolf, S., & Ballif, C. (2015). Organic–inorganic halide perovskite/crystalline silicon four-terminal tandem solar cells. *Physical Chemistry Chemical Physics*, *17*(3), 1619–1629.

Mailoa, J. P., Bailie, C. D., Johlin, E. C., Hoke, E. T., Akey, A. J., Nguyen, W. H., McGehee, M. D., & Buonassisi, T. (2015). A 2-terminal perovskite/silicon multijunction solar cell enabled by a silicon tunnel junction. *Applied Physics Letters*, *106*(12), 121105.

Makori, N. E., Amatalo, I. A., Karimi, P. M., & Njoroge, W. K. (2015). Characterization of SnSe-CdO: Sn PN junction for solar cell applications. *Int. J. Energy Eng*, *5*(1).

Mandadapu, U., Vedanayakam, S. V., & Thyagarajan, K. (2017). Simulation and analysis of lead based perovskite solar cell using SCAPS-1D. *Indian J. Sci. Technol.*, *10*(11), 65–72.

Marshall, K. P., Tao, S., Walker, M., Cook, D. S., Lloyd-Hughes, J., Varagnolo, S., Wijesekara, A., Walker, D., Walton, R. I., & Hatton, R. A. (2018). Cs 1− x Rb x SnI 3 light harvesting semiconductors for perovskite photovoltaics. *Materials Chemistry Frontiers*, *2*(8), 1515–1522.

Marshall, K. P., Walker, M., Walton, R. I., & Hatton, R. A. (2016). Enhanced stability and efficiency in hole-transport-layer-free CsSnI3 perovskite photovoltaics. *Nature Energy*, *1*(12), 1–9.

Marshall, K. P., Walton, R. I., & Hatton, R. A. (2015). Tin perovskite/fullerene planar layer photovoltaics: improving the efficiency and stability of lead-free devices. *Journal of Materials Chemistry A*, *3*(21), 11631–11640.

Mazzarella, L., Lin, Y., Kirner, S., Morales-Vilches, A. B., Korte, L., Albrecht, S., Crossland, E., Stannowski, B., Case, C., & Snaith, H. J. (2019). Infrared light management using a nanocrystalline silicon oxide interlayer in monolithic perovskite/silicon heterojunction tandem solar cells with efficiency above 25%. *Advanced Energy Materials*, *9*(14), 1803241.

Melas-Kyriazi, J., Ding, I., Marchioro, A., Punzi, A., Hardin, B. E., Burkhard, G. F., Tétreault, N., Grätzel, M., Moser, J., & McGehee, M. D. (2011). The Effect of Hole Transport Material Pore Filling on Photovoltaic Performance in Solid-State Dye-Sensitized Solar Cells. *Advanced Energy Materials*, *1*(3), 407–414.

Moiz, S. A., & Alahmadi, A. N. M. (2021). Design of dopant and lead-free novel perovskite solar cell for 16.85% efficiency. *Polymers*, *13*(13), 2110.

Momblona, C., Malinkiewicz, O., Roldán-Carmona, C., Soriano, A., Gil-Escrig, L., Bandiello, E., Scheepers, M., Edri, E., & Bolink, H. J. (2014). Efficient methylammonium lead iodide perovskite solar cells with active layers from 300 to 900 nm. *Apl Materials*, *2*(8), 81504.

Monti, M., Tao, S. X., Staniforth, M., Crocker, A., Griffin, E., Wijesekara, A., Hatton, R. A., & Lloyd-Hughes, J. (2018). Efficient Intraband Hot Carrier Relaxation in the Perovskite Semiconductor Cs1–x Rb x SnI3 Mediated by Strong Electron–Phonon Coupling. *The Journal of Physical Chemistry C*, *122*(36), 20669–20675.

Nalianya, M. A., Awino, C., Barasa, H., Odari, V., Gaitho, F., Omogo, B., & Mageto, M. (2021). Numerical study of lead free CsSn0. 5Ge0. 5I3 perovskite solar cell by SCAPS-1D. *Optik*, *248*, 168060.

Namvar, M. J., Abbaspour-Fard, M. H., Rezaei Roknabadi, M., Behjat, A., & Mirzaei, M. (2019). The effect of inserting combined Rubidium-Cesium cation on performance of perovkite solar cell FAMAPb (IBr) 3. *Journal of Research on Many-Body Systems*, *8*(19), 125–138.

Neamen, D. A. (2003). *Semiconductor Physics and Devices: Basic Principles* (Third Edit). McGraw-Hill.

Nelson, J. (2003). *The Physics of Solar cells*. Imperial College Press.

Nogay, G., Sahli, F., Werner, J., Monnard, R., Boccard, M., Despeisse, M., Haug, F. J., Jeangros, Q., Ingenito, A., & Ballif, C. (2019). 25.1%-efficient monolithic perovskite/silicon tandem solar cell based on ap-type monocrystalline textured silicon wafer and high-temperature passivating contacts. *ACS Energy Letters*, *4*(4), 844–845.

Nuys, M. R. (2015). *Characterization & Modification of Copper and Iron Oxide Nanoparticles for Application as Absorber Material in Silicon based Thin Film Solar Cells* (Vol. 291).

Parisi, A., Pernice, R., Rocca, V., Curcio, L., Stivala, S., Cino, A. C., Cipriani, G., Di Dio, V., Ricco Galluzzo, G., & Miceli, R. (2015). Graded carrier concentration absorber profile for high efficiency CIGS solar cells. *International Journal of Photoenergy*, *2015*.

Park, Y., Choong, V., Gao, Y., Hsieh, B. R., & Tang, C. W. (1996). Work function of indium tin oxide transparent conductor measured by photoelectron spectroscopy. *Applied Physics Letters*, *68*(19), 2699–2701.

Partain, L. D., Kuryla, M. S., Weiss, R. E., Ransom, R. A., McLeod, P. S., Fraas, L. M., & Cape, J. A. (1987). 26.1% solar cell efficiency for Ge mechanically stacked under GaAs. *Journal of Applied Physics*, *62*(7), 3010–3015.

Physics, T. (2014). *Performance Optimization Of Tin Halide Perovskite Solar Cells Via Numerical Simulation Performance Optimization Of Tin Halide Perovskite*.

Prasanna, R., Gold-Parker, A., Leijtens, T., Conings, B., Babayigit, A., Boyen, H.-G., Toney, M. F., & McGehee, M. D. (2017). Band gap tuning via lattice contraction and octahedral tilting in perovskite materials for photovoltaics. *Journal of the American Chemical Society*, *139*(32), 11117–11124.

Rahman, M. A. (2021). Design and simulation of a high-performance Cd-free Cu2SnSe3 solar cells with SnS electron-blocking hole transport layer and TiO2 electron transport layer by SCAPS-1D. *SN Applied Sciences*, *3*(2), 1–15.

Rai, S., Pandey, B. K., & Dwivedi, D. K. (2020). Device simulation of low cost HTM free perovskite solar cell based on TiO2 electron transport layer. *AIP Conference Proceedings*, *2220*(1), 140022.

Richter, A., Benick, J., Feldmann, F., Fell, A., Hermle, M., & Glunz, S. W. (2017). n-Type Si solar cells with passivating electron contact: Identifying sources for efficiency limitations by wafer thickness and resistivity variation. *Solar Energy Materials and Solar Cells*, *173*, 96–105.

Ruiz-Preciado, M. A., Gota, F., Fassl, P., Hossain, I. M., Singh, R., Laufer, F., Schackmar, F., Feeney, T., Farag, A., & Allegro, I. (2022). Monolithic Two-Terminal Perovskite/CIS Tandem Solar Cells with Efficiency Approaching 25%. *ACS Energy Letters*, *7*, 2273–2281.

Sahare, S., Pham, H. D., Angmo, D., Ghoderao, P., MacLeod, J., Khan, S. B., Lee, S., Singh, S. P., & Sonar, P. (2021). Emerging perovskite solar cell technology: Remedial actions for the foremost challenges. *Advanced Energy Materials*, *11*(42), 2101085.

Sahli, F., Werner, J., Kamino, B. A., Bräuninger, M., Monnard, R., Paviet-Salomon, B., Barraud, L., Ding, L., Diaz Leon, J. J., & Sacchetto, D. (2018). Fully textured monolithic perovskite/silicon tandem solar cells with 25.2% power conversion efficiency. *Nature Materials*, *17*(9), 820–826.

Salado, M., Kokal, R. K., Calio, L., Kazim, S., Deepa, M., & Ahmad, S. (2017). Identifying the charge generation dynamics in Cs+-based triple cation mixed perovskite solar cells. *Physical Chemistry Chemical Physics*, *19*(34), 22905–22914.

Sampaio, P. G. V., & González, M. O. A. (2017). Photovoltaic solar energy: Conceptual framework. *Renewable and Sustainable Energy Reviews*, *74*, 590–601.

Scharber, M. C., Mühlbacher, D., Koppe, M., Denk, P., Waldauf, C., Heeger, A. J., & Brabec, C. J. (2006). Design rules for donors in bulk-heterojunction solar cells—Towards 10% energy-conversion efficiency. *Advanced Materials*, *18*(6), 789–794.

Seshan, K. (2012). *Handbook of thin film deposition*. William Andrew.

Sharbati, S., & Sites, J. R. (2014). Impact of the Band Offset for n-Zn (O, S)/p-Cu (In, Ga) Se $ _ {2} $ Solar Cells. *IEEE Journal of Photovoltaics*, *4*(2), 697–702.

Sherkar, T. S., Momblona, C., Gil-Escrig, L., Avila, J., Sessolo, M., Bolink, H. J., & Koster, L. J. A. (2017). Recombination in perovskite solar cells: significance of grain boundaries, interface traps, and defect ions. *ACS Energy Letters*, *2*(5), 1214–1222.

Shi, Z., & Jayatissa, A. H. (2018). Perovskites-based solar cells: A review of recent progress, materials and processing methods. *Materials*, *11*(5), 729.

Song, T.-B., Yokoyama, T., Aramaki, S., & Kanatzidis, M. G. (2017). Performance enhancement of lead-free tin-based perovskite solar cells with reducing atmosphere-assisted dispersible additive. *ACS Energy Letters*, *2*(4), 897–903.

Stevenson, K. J., & Luchkin, S. (2021). Photochemically-Induced Phase Segregation of Mixed Halide Perovskite Solar Cells. *ECS Meeting Abstracts*, *45*, 1809.

Sun, Y., Peng, J., Chen, Y., Yao, Y., & Liang, Z. (2017). Triple-cation mixed-halide perovskites: towards efficient, annealing-free and air-stable solar cells enabled by Pb (SCN) 2 additive. *Scientific Reports*, *7*(1), 1–7.

Sveinbjörnsson, K., Li, B., Mariotti, S., Jarzembowski, E., Kegelmann, L., Wirtz, A., Frühauf, F., Weihrauch, A., Niemann, R., & Korte, L. (2022). Monolithic Perovskite/Silicon Tandem Solar Cell with 28.7% Efficiency Using Industrial Silicon Bottom Cells. *ACS Energy Letters*, *7*, 2654–2656.

Tanaka, K., Minemoto, T., & Takakura, H. (2009). Analysis of heterointerface recombination by Zn1− xMgxO for window layer of Cu (In, Ga) Se2 solar cells. *Solar Energy*, *83*(4), 477–479.

Terheiden, B., Ballmann, T., Horbelt, R., Schiele, Y., Seren, S., Ebser, J., Hahn, G., Mertens, V., Koentopp, M. B., & Scherff, M. (2015). Manufacturing 100-µm-thick silicon solar cells with efficiencies greater than 20% in a pilot production line. *Physica Status Solidi (A)*, *212*(1), 13–24.

Trieb, F., & Elnokraschy, H. (2007). Concentrating solar power for seawater desalination. *IWCT*, *12*, 2–13.

Trukhanov, V. A., Bruevich, V. V, & Paraschuk, D. Y. (2011). Effect of doping on performance of organic solar cells. *Physical Review B*, *84*(20), 205318.

Ushasree, P. M., Singh, A., Tian, H., Unger, E., Persson, C., Gibson, E. A., Bruce, D. W., O'Hare, D., & Walton, R. I. (2019). *Solar Energy Capture Materials*. Royal Society of Chemistry.

Wang, X., Zhang, T., Lou, Y., & Zhao, Y. (2019). All-inorganic lead-free perovskites for optoelectronic applications. *Materials Chemistry Frontiers*, *3*(3), 365–375.

Xing, G., Mathews, N., Sun, S., Lim, S. S., Lam, Y. M., Grätzel, M., Mhaisalkar, S., & Sum, T. C. (2013). Long-range balanced electron-and hole-transport lengths in organic-inorganic CH3NH3PbI3. *Science*, *342*(6156), 344–347.

Xu, L., Du, H., & Zhang, X. (2021). Driving forces of carbon dioxide emissions in China's cities: An empirical analysis based on the geodetector method. *Journal of Cleaner Production*, *287*, 125169.

Yin, W., Shi, T., & Yan, Y. (2014). Unique properties of halide perovskites as possible origins of the superior solar cell performance. *Advanced Materials*, *26*(27), 4653–4658.

Yoshikawa, K., Kawasaki, H., Yoshida, W., Irie, T., Konishi, K., Nakano, K., Uto, T., Adachi, D., Kanematsu, M., & Uzu, H. (2017). Silicon heterojunction solar cell with interdigitated back contacts for a photoconversion efficiency over 26%. *Nature Energy*, *2*(5), 1–8.

Zeghbroeck, B. Van. (2011). *Principles of Semiconductor Devices*.

Zhang, C., Qi, L., Chen, Q., Lv, L., Ning, Y., Hu, Y., Hou, Y., & Teng, F. (2014). Plasma treatment of ITO cathode to fabricate free electron selective layer in inverted polymer solar cells. *Journal of Materials Chemistry C*, *2*(41), 8715–8722.

Zhang, X., Liu, H., Wang, W., Zhang, J., Xu, B., Karen, K. L., Zheng, Y., Liu, S., Chen, S., & Wang, K. (2017). Hybrid perovskite light-emitting diodes based on perovskite nanocrystals with organic–inorganic mixed cations. *Advanced Materials*, *29*(18), 1606405.

Zheng, J., Wang, G., Duan, W., Mahmud, M. A., Yi, H., Xu, C., Lambertz, A., Bremner, S., Ding, K., & Huang, S. (2022). Monolithic Perovskite–Perovskite–Silicon Triple-Junction Tandem Solar Cell with an Efficiency of over 20%. *ACS Energy Letters*, *7*, 3003–3005.

Zhong, Y., Tada, A., Izawa, S., Hashimoto, K., & Tajima, K. (2014). Enhancement of VOC without loss of JSC in organic solar cells by modification of donor/acceptor interfaces. *Advanced Energy Materials*, *4*(5), 1301332.

APPENDICES

Appendix I: Introduction letter from the institution

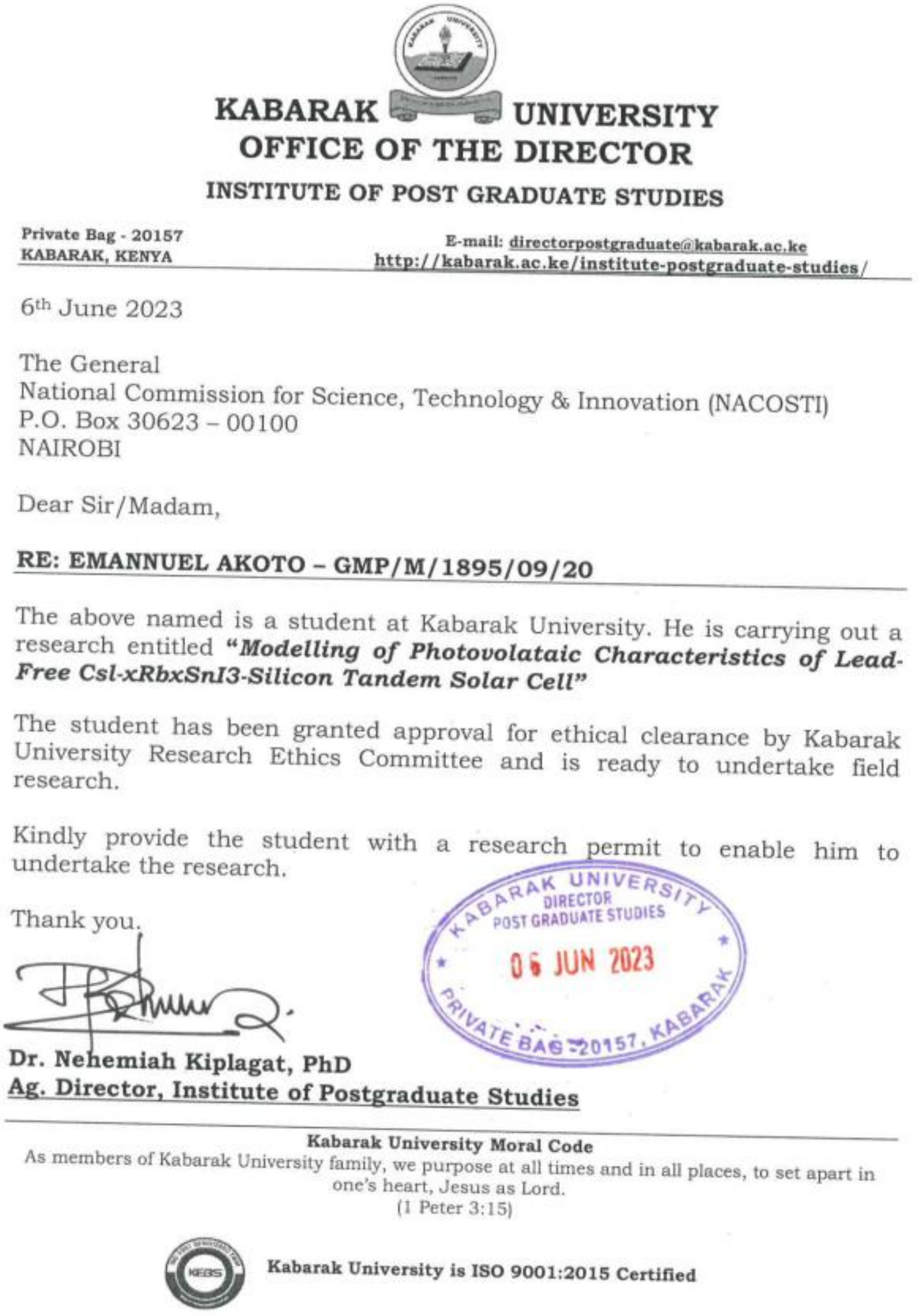

KABARAK UNIVERSITY
OFFICE OF THE DIRECTOR
INSTITUTE OF POST GRADUATE STUDIES

Private Bag - 20157
KABARAK, KENYA

E-mail: directorpostgraduate@kabarak.ac.ke
http://kabarak.ac.ke/institute-postgraduate-studies/

6th June 2023

The General
National Commission for Science, Technology & Innovation (NACOSTI)
P.O. Box 30623 – 00100
NAIROBI

Dear Sir/Madam,

RE: EMANNUEL AKOTO – GMP/M/1895/09/20

The above named is a student at Kabarak University. He is carrying out a research entitled ***"Modelling of Photovolataic Characteristics of Lead-Free Csl-xRbxSnI3-Silicon Tandem Solar Cell"***

The student has been granted approval for ethical clearance by Kabarak University Research Ethics Committee and is ready to undertake field research.

Kindly provide the student with a research permit to enable him to undertake the research.

Thank you.

KABARAK UNIVERSITY
DIRECTOR
POST GRADUATE STUDIES
06 JUN 2023
PRIVATE BAG 20157, KABARAK

Dr. Nehemiah Kiplagat, PhD
Ag. Director, Institute of Postgraduate Studies

Kabarak University Moral Code
As members of Kabarak University family, we purpose at all times and in all places, to set apart in one's heart, Jesus as Lord.
(1 Peter 3:15)

Kabarak University is ISO 9001:2015 Certified

Appendix II: KUREC Clearance Letter

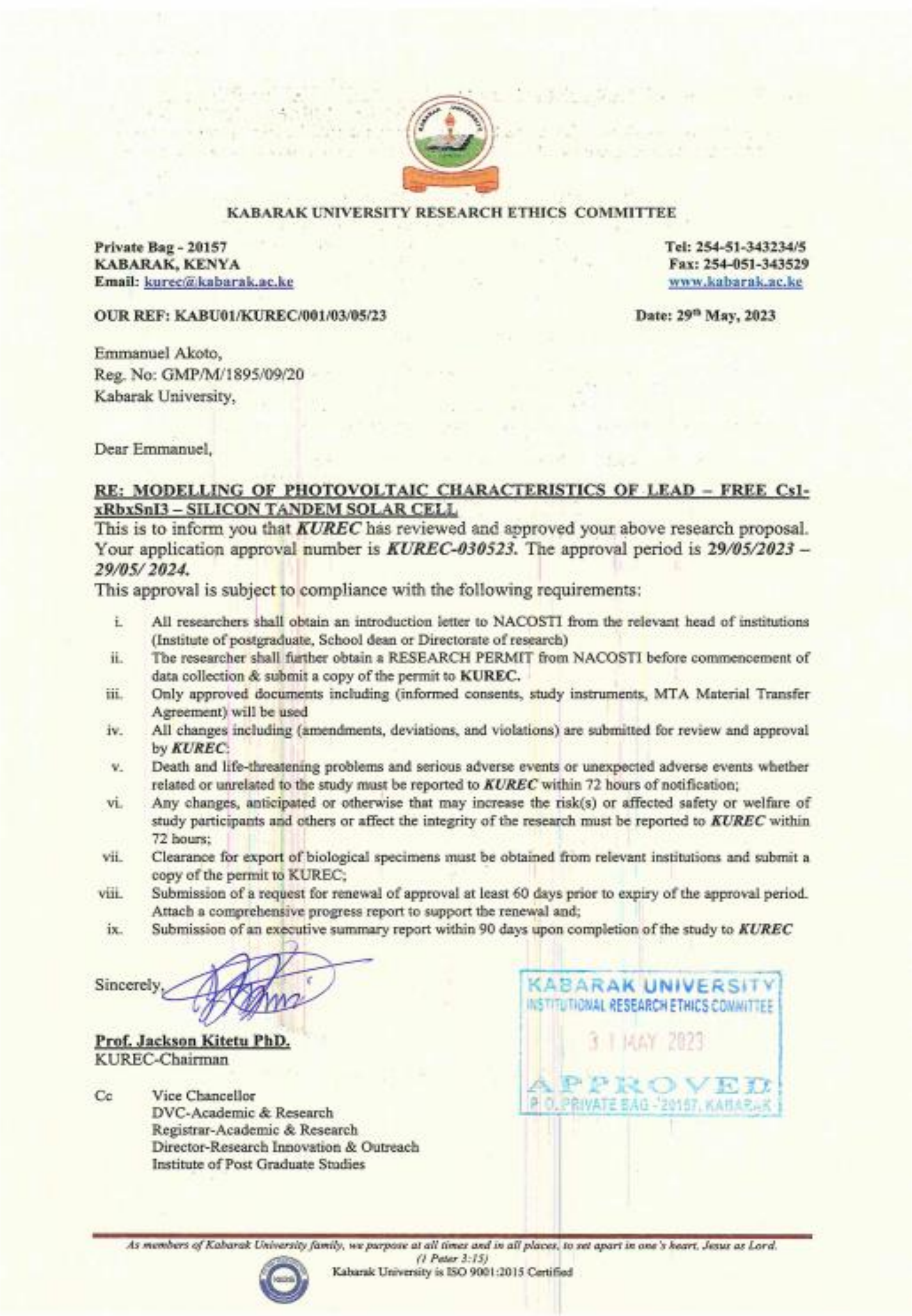

KABARAK UNIVERSITY RESEARCH ETHICS COMMITTEE

Private Bag - 20157
KABARAK, KENYA
Email: kurec@kabarak.ac.ke

Tel: 254-51-343234/5
Fax: 254-051-343529
www.kabarak.ac.ke

OUR REF: KABU01/KUREC/001/03/05/23

Date: 29th May, 2023

Emmanuel Akoto,
Reg. No: GMP/M/1895/09/20
Kabarak University,

Dear Emmanuel,

RE: MODELLING OF PHOTOVOLTAIC CHARACTERISTICS OF LEAD – FREE Cs1-xRbxSnI3 – SILICON TANDEM SOLAR CELL

This is to inform you that ***KUREC*** has reviewed and approved your above research proposal. Your application approval number is ***KUREC-030523.*** The approval period is ***29/05/2023 – 29/05/ 2024.***

This approval is subject to compliance with the following requirements:

i. All researchers shall obtain an introduction letter to NACOSTI from the relevant head of institutions (Institute of postgraduate, School dean or Directorate of research)
ii. The researcher shall further obtain a RESEARCH PERMIT from NACOSTI before commencement of data collection & submit a copy of the permit to **KUREC.**
iii. Only approved documents including (informed consents, study instruments, MTA Material Transfer Agreement) will be used
iv. All changes including (amendments, deviations, and violations) are submitted for review and approval by ***KUREC***:
v. Death and life-threatening problems and serious adverse events or unexpected adverse events whether related or unrelated to the study must be reported to ***KUREC*** within 72 hours of notification;
vi. Any changes, anticipated or otherwise that may increase the risk(s) or affected safety or welfare of study participants and others or affect the integrity of the research must be reported to ***KUREC*** within 72 hours;
vii. Clearance for export of biological specimens must be obtained from relevant institutions and submit a copy of the permit to KUREC;
viii. Submission of a request for renewal of approval at least 60 days prior to expiry of the approval period. Attach a comprehensive progress report to support the renewal and;
ix. Submission of an executive summary report within 90 days upon completion of the study to ***KUREC***

Sincerely,

Prof. Jackson Kitetu PhD.
KUREC-Chairman

KABARAK UNIVERSITY
INSTITUTIONAL RESEARCH ETHICS COMMITTEE
31 MAY 2023
APPROVED
P.O. PRIVATE BAG - 20157, KABARAK

Cc Vice Chancellor
DVC-Academic & Research
Registrar-Academic & Research
Director-Research Innovation & Outreach
Institute of Post Graduate Studies

As members of Kabarak University family, we purpose at all times and in all places, to set apart in one's heart, Jesus as Lord.
(1 Peter 3:15)
Kabarak University is ISO 9001:2015 Certified

Appendix III: NACOSTI Permit Research

REPUBLIC OF KENYA

NATIONAL COMMISSION FOR
SCIENCE,TECHNOLOGY & INNOVATION

Ref No: **487198**

Date of Issue: **30/June/2023**

RESEARCH LICENSE

This is to Certify that Mr.. EMMANUEL AKOTO of Kabarak University, has been licensed to conduct research as per the provision of the Science, Technology and Innovation Act, 2013 (Rev.2014) in Transnzoia on the topic: MODELLING OF PHOTOVOLTAIC CHARACTERISTICS OF LEAD ? FREE Cs1-xRbxSnI3 ? SILICON TANDEM SOLAR CELL for the period ending : 30/June/2024.

License No: **NACOSTI/P/23/27488**

487198

Applicant Identification Number

Director General
NATIONAL COMMISSION FOR
SCIENCE,TECHNOLOGY &
INNOVATION

Verification QR Code

NOTE: This is a computer generated License. To verify the authenticity of this document,
Scan the QR Code using QR scanner application.

See overleaf for conditions

Appendix IV: List of Publication

Results in Optics 12 (2023) 100470

Contents lists available at ScienceDirect

Results in Optics

journal homepage: www.sciencedirect.com/journal/results-in-optics

Monolith $Cs_{1-x}Rb_xSnI_3$ perovskite – silicon 2T tandem solar cell using SCAPS-1D

Emmanuel Akoto[a,*], Victor Isahi[a], Victor Odari[b,c], Christopher Maghanga[a,c],
Francis Nyongesa[d]

[a] Department of Physical and Biological Sciences, Kabarak University, P.O. Box Private Bag-20157, Kabarak, Kenya
[b] Department of Physics, Masinde Muliro University of Science and Technology, P.O. Box 190-50100, Kakamega, Kenya
[c] Materials Research Society of Kenya, P.O. Box 15653-00503, Nairobi, Kenya
[d] Department of Physics, University of Nairobi, P.O. Box 30197-00100, Nairobi, Kenya

ARTICLE INFO

Keywords:
Tandem solar cells
Silicon
$Cs_{1-x}Rb_xSnI_3$ perovskite
SCAPS-1D

ABSTRACT

Tandem solar cells (TSCs) have gained notoriety by the use of various absorber layers with different bandgaps. The photovoltaic characteristics of $Cs_{1-x}Rb_xSnI_3$ perovskite – silicon TSCs were determined through simulation using the SCAPS-1D software in this work by first validating the experimentally obtained efficiency of 2.08% for ITO/$Cs_{0.8}Rb_{0.2}SnI_3$/PCBM/BCP/Al structure. The influence of chlorinated and undoped ITO front contact, variation of Electron Transport Layer (ETL) thickness, doping concentration, CBO and variation of absorber layer thickness, defect density, and doping concentration was studied. Optimum V_{OC} (0.9893 V), J_{SC} (30.04 mA/cm2), fill factor (81.78 %) and efficiency (24.31 %) were determined. The bottom cell was simulated independently with reference to experimental data using the structure Al/c-Si (n)/c-Si (p)/c-Si (p +)/Au resulting in an efficiency of 26.68 %. The monolithic $Cs_{0.8}Rb_{0.2}SnI_3$ perovskite – silicon tandem solar cell of the architecture ITO/$Cs_{0.8}Rb_{0.2}SnI_3$/c-Si (n)/c-Si (p)/c-Si (p +)/Au performance was analyzed by varying the thickness, doping concentration, and defect density of the active layers. Optimized parameters obtained were as follows: top perovskite layer thickness (100 nm), doping concentrations (5×10^{19} cm^{-3}) and defect density (1×10^{13} cm^{-3}), and bottom silicon absorber layer thickness (50 μm), doping concentrations (5×10^{16} cm^{-3}), defect density (1×10^{12} cm^{-3}), and a work function of 5.3 eV with chlorinated ITO as the front contact of the tandem cell. Optimized outcomes of efficiency (29.82 %), V_{OC} (0.7992 V), J_{SC} density (43.39 mA/cm^2), and fill factor (85.98 %) were realized for the 2T $Cs_{0.8}Rb_{0.2}SnI_3$ perovskite – silicon tandem solar cell.

1. Introduction

Solar power has drawn a lot of attention as a source of sustainable, clean, and green energy in this age of rapidly advancing technology (Saga, 2010). To create effective and affordable solar cells, a tremendous amount of effort has been made. Si-based solar cells have undergone decades of development, including wafer surface treatment, device structure design, Si defects passivation, optical design, and optical design, which gradually increases the device efficiency to a world-record value of 26.1% for single crystal Si cells (Partain et al., 19871987), 23.3% for multi-crystalline Si cells (Richter et al., 2017), and 26.7% for Si-based heterostructure solar cells (Stevenson and Luchkin, 2021). Since the invention of PV, c-Si wafer-based photovoltaic (PV) devices have been successfully developed and commercialized, and dominated the global solar power market (by about 90%) (Fazal and Rubaiee, 2023). The benefits of C-Si solar cells include their ease of production, environmental friendliness, vitality, excellent performance and its ability to withstand adversity. Further advancement in efficiency of the solar cells, becomes a bottleneck, with its efficiency approaching the Shockley-Quisser (S-Q) limit of 29% for a single-junction cell (Stevenson and Luchkin, 2021). This is primarily due to the indirect optical bandgap of the c-Si is c-Si (1.12 eV), as a result of the relatively low optical absorption coefficient of C-Si cells (Saga, 2010), necessitating the relatively thick layer of absorber material. This coupled with the high-purity crystals required (Saga, 2010), and the high processing cost of a c-Si wafer (50% of the manufacturing cost of a c-Si PV module), research on a new module for solar cells becomes necessary.

Perovskite solar cells (PSCs) attracted attention as one of the most

---

[*] Corresponding author.
E-mail address: akoto@kabarak.ac.ke (E. Akoto).

https://doi.org/10.1016/j.rio.2023.100470
Received 17 March 2023; Received in revised form 21 May 2023; Accepted 26 June 2023

Appendix V: Evidence of Conference Participation

CERTIFICATE OF PARTICIPATION

BALEWARE

Issued to

Emmanuel Akoto

for participating at ANSOLE´s 12th Anniversary International Online Conference (A^2IOC 2023) on the 4th of February 2023, and lecturing on "Monolith $Cs_{1-x}Rb_xSnI_3$ Perovskite/Silicon Tandem Solar Cell Using SCAPS-1D Software". A^2IOC 2023 was co-hosted by Masinde Muliro University of Science and Technology (MMUST), Kenya, and Faculty of Sciences, University of Tunis-Elmanar, Tunis, Tunisia.

Prof. Dr. Daniel A. M. EGBE
International Coordinator of ANSOLE & BALEWARE

African Network for Solar Energy e.V. (ANSOLE e.V.)
Schillerstrasse 5
07745 Jena, Germany
Tel.: +49 (0) 3641-2349352
Info@ansole.org
www.ansole.org

Riga Photonics Centre

UPPSALA UNIVERSITET

ipmt Institute of Polymeric Materials and Testing

KIT Karlsruhe Institute of Technology

Université Internationale de Rabat
THE INNOVATIVE UNIVERSITY